DESIGN AND COMMISSIONING OF A COMPACT CONDUCTION-COOLED SRF CRYOMODULE

A Dissertation

Presented to the Faculty of the Graduate School

of Cornell University

in Partial Fulfillment of the Requirements for the Degree of

Doctor of Philosophy

by

Neil Anthony Stilin

December 2024

DESIGN AND COMMISSIONING OF A COMPACT CONDUCTION-COOLED SRF CRYOMODULE

Neil Anthony Stilin, Ph.D.

Cornell University 2024

The last 10 - 20 years have seen major improvements in both the RF performance of Nb_3Sn cavities and the cooling capacities of 4 K cryocoolers. In the last few years in particular, these developments have reached a critical crossroads where a single cryocooler can provide enough cooling to operate a single- or even multi-cell 1.3 GHz Nb_3Sn cavity at an accelerating gradient of 10 - 15 MV/m. For a single-cell cavity of this size, this field level corresponds to a roughly 1 MeV gain in beam energy for relativistic particles. This is well within relevant levels for a variety of small-scale accelerator applications in fields such as energy, environmental sustainability, medicine, security and industry. This dissertation describes work that has been done to demonstrate the feasibility of making superconducting radio-frequency (SRF) technology accessible to such small-scale applications, which relies on removing the need for liquid helium as a cooling source. An initial proof-of-principle study was performed, which used a single cryocooler and a single-cell 2.6 GHz Nb_3Sn cavity. This experiment achieved the world's first successful demonstration of an SRF cavity reaching accelerating gradients relevant for small-scale applications while relying solely on a cryocooler as a cooling source. Following the success of this study, a new project was started to extend this concept to a full SRF accelerating cryomodule. The successful design of such a system is described in detail, along with the complete commissioning of the newly designed and fabricated single-cell Nb_3Sn cavity which will be used in the cryomodule.

BIOGRAPHICAL SKETCH

Neil Anthony Stilin was born and raised in the small town of Williams Bay, Wisconsin. He attended school in the Williams Bay public school system from kindergarten through 12th grade. For such a small public school, this setting provided a robust learning environment. Williams Bay is also home to Yerkes Observatory, a place of rich history in the study of astronomy and astrophysics; spending countless hours at the observatory played a key role in inspiring Neil's interest in physics. After graduating from high school in 2014, he began his undergraduate studies at Cornell University in Ithaca, NY. In 2018 he obtained his B.A. in physics, after which he returned for another few years of graduate school. Neil joined the Cornell SRF group in the summer of 2019, and after several years of research completed his Ph.D. in the summer of 2024.

To my family – parents Scott and Patti and sister Allison – and dearest friends who have supported my journey throughout the years.

ACKNOWLEDGEMENTS

Before all else, I extend my deepest thanks to my advisor, Matthias Liepe. Everybody hears "those" stories before starting a Ph.D. program; conducting research under Matthias' guidance has been a prime example of the complete other end of the spectrum. I have never felt anything other than full support and encouragement of my research during my time in the SRF group. Even when mistakes happen, Matthias is the first to assure you that things will be alright and redirect focus onto how the issue might be resolved. Matthias also has the propensity to believe in his students' capabilities so strongly that they have no choice but to believe in themselves too, even when they inevitably find themselves in a slump. If all of this weren't enough, Matthias never fails to encourage a healthy work-life balance for all the members of the SRF group – encouraging students to join the paddling club with him, organizing group lunches and rooftop barbecues in the summer, and generally making sure students prioritize their health. In summary, the fact that every Cornell SRF group graduate sings a similar level of praise is quite telling and beyond well-earned.

Next, I would like to acknowledge all the members of the SRF team who have supported my work and provided invaluable insight throughout every stage of my research. Starting with Adam Holic, Jessica Turco, Peter Quigley and James Sears, who were all part of the "core" cryomodule project support team and made critical contributions in advising all aspects of the design, creating and managing the 3D models of the system, offering input on cryomodule design topics that I wouldn't have known even existed if not for them, and many more. I'd also like to thank Greg Kulina and Paul Bishop for their help with just about anything that goes on in the Newman Lab basement, Holly Conklin and Terri Gruber-Hine for their dedicated work performing chemical treatments and cleaning literally hundreds of

parts sent their way for this project, and Terry Neiss and all the Newman Lab machinists for creating those hundreds of parts to begin with. Tim O'Connell and Eric Smith also deserve recognition for providing valuable insights throughout the duration of this project. My fellow graduate students and scientists have helped me grow as a researcher from my very first summer with the SRF group through to my very last: James Maniscalco, Ryan Porter, Pete Koufalis, Thomas Oseroff[1], Gabriel Gaitan, Liana Shpani, Nicole Verboncoeur, Sadie Seddon-Stettler, Jake Parsons (who deserves bonus acknowledgement for being thrown into the pilot assembly of the cryomodule right after joining the group), Zeming Sun, Thomas Oseroff[2] and Nathan Sitaraman.

Finally, I would like to thank all of my loved ones who have supported and encouraged me throughout my years at Cornell. My remarkable friends from both the taekwondo team and swing dance club, who provided the best company I could ask for and helped me learn new skills which I plan to continue developing throughout my life. My close friends from my hometown who still keep in touch, even as we've all ended up in different time zones. My wonderful partner Valeria, who has given me more joy since we've met than I could have imagined. And of course, my family: Scott (father), Patti (mother) and Allison (sister), who have always been there for me more than anyone else. Without their love and support, I certainly would not have made it to where I am today. My extended family has also been a reliable source of encouragement, and my cat Tungsten never fails to ease my stress with his affection.

[1]Graduate Student
[2]Research Associate

The work shown here was supported by:

U.S. DOE award DE-SC0008431.

U.S. DOE award DE-SC0021038.

TABLE OF CONTENTS

LIST OF TABLES

LIST OF FIGURES

CHAPTER 1

INTRODUCTION

Particle accelerators have been a key driver in scientific discovery for decades across a variety of research fields. Particle accelerators excel at producing high intensity beams and x-rays which are capable of probing the structure of sub-atomic particles in remarkable detail [A$^+$12]. They are also effective for studying new materials as well as pushing the cutting edge of research in chemistry, biology and medicine [BEW05]. Beyond fundamental science, particle accelerators are also a staple of valuable applications in fields such as energy, environment, medicine, security and industry [HS09, HW15]. Particle beams could be used as the main drivers of a new type of nuclear reactor while also treating the waste products of current reactors. Treatment of wastewater, sewer sludge and flue gas can all be made more efficient by the use of accelerated beams or the X-rays they produce. Accelerators are already used for both medical diagnostics and treatments, and could also provide the means to greatly increase production of critical medical isotopes. High-intensity X-rays can play a pivotal role in increasing the available throughput of cargo scanning and can also be used in a variety of industrial processes such as polymer cross-linking to improve material durability [HS09, HW15].

While large-scale accelerators have already widely adopted the use of superconducting cavities, enabling more efficient operation and improved beam dynamics and power handling, smaller operations still face major barriers preventing such adaptation. Namely, the liquid helium used to cool superconducting cavities requires significant additional infrastructure which is costly, complex and requires expert maintenance. For a kilometer(s)-long machine, this trade off is well worth the benefit; for a small, "table-top" size machine, the comparative cost is much greater.

Yet many of the applications mentioned previously operate at relatively small scale and could be further enhanced by switching to superconducting technology. Addressing this dilemma has been a focal point in superconducting radio-frequency (SRF) research in recent years, and is the primary focus of this dissertation.

1.1 Organization of the Dissertation

The journey of this work begins with an abridged SRF science primer in Chapter 2, covering the basics of superconductivity, Nb_3Sn as an alternative material for accelerating cavities, and how cavities are tested and characterized. While most projects in Cornell's SRF group delve deeply into the inner workings of superconducting materials in order to find ways to improve their performance, this work represents more of an "apply what's available" approach, in which the nature of the application is the main novelty. Thus for the sake of following the discussions of this dissertation, it is not quite necessary to cover all the fascinating minutia behind superconductivity. Rather, Chapter 2 will cover only what's necessary to get any interested reader up and running so they may absorb the remainder of the work effectively.

Chapter 3 covers the main motivation behind this research and the new technologies that make it possible. In particular, small-scale applications for accelerators will be introduced in more detail before discussing one of the critical developments that makes SRF science accessible to small operations: modern cryocoolers. The chapter wraps up with brief discussions of the materials required for bringing together cryocoolers and SRF, followed by acknowledgment of other ongoing projects on this topic.

An initial proof-of-principle demonstration is described in detail in Chapter 4.

This experiment resulted in the world's first successful operation of a conduction-cooled (cryocooler-based) SRF cavity at 10 MV/m, an accelerating gradient relevant for the applications of interest. This chapter will cover the system design, assembly process, RF testing and various discussion of the results, and finally comparison of experimental results to numerical simulations. The lessons learned from this experiment will play a key role in guiding many design choices in the main project.

After demonstrating the feasibility of using cryocoolers to cool SRF cavities during RF operation, the next step was to design a full, compact SRF accelerating cryomodule that replaces all liquid cryogenics with cryocoolers. This endeavor is the focus of Chapter 5. To motivate the initial steps of the design, key operational goals will be discussed. The majority of the chapter will be dedicated to discussing the design of two of the most important and challenging components: the accelerating cavity and the high-power input couplers. The design of the vacuum vessel, thermal shield and other auxiliary components will also be described, before collecting all of the calculated heat loads of the system to show they are within the limits set by the cryocoolers being used.

Chapter 6 describes the commissioning process of the new accelerating cavity, named LCC1-1. The entire process, from machining and electron-beam welding to baseline testing both before and after coating with Nb_3Sn, will be discussed. Various difficulties throughout this process will be introduced, along with some future modifications to the cavity that may be required to reach the intended performance for long-term use.

Finally, a high-level summary and outlook for the future of this project are presented in Chapter 7.

CHAPTER 2

COMPACT SRF FOUNDATION

This chapter will introduce the background knowledge required to follow the remainder of this work. The studies described in this dissertation are focused more on developing a new application environment for already established SRF cavity technology, rather than trying to improve cavity performance. Therefore, the required theory is rather light in comparison to other works which involve in-depth analysis of the cavity material and how it is affected by different treatments. The first section will introduce the basics of SRF science, namely the phenomenon of superconductivity and how (and why) it is applied to the context of accelerators. This discussion will only mention the "simple" forms of superconducting parameters without delving into their more complex or expanded forms, which would already be more than what is required for this work. The following section will cover the material known as Nb_3Sn – why it has garnered interest in accelerator physics, key properties, growth methods and state-of-the-art performance. The final section will discuss how superconducting cavities are tested to measure their performance and introduce key metrics which are used to describe such performance. Any reader who is familiar with the topics mentioned here can readily skip this chapter and move on to the next.[1]

2.1 Journey to SRF

The phenomenon of superconductivity is on its own an incredibly rich topic, capable of fueling countless research careers and dozens (or hundreds) of textbooks.

[1]Except for Matthias, my advisor, who may wish to review the text of this chapter to ensure that no classified secrets are revealed.

While initially not the most intuitive subject, well-established theories of superconductivity are able to motivate both quantitative and qualitative understanding. As more complex superconducting materials continue to be discovered, new categories of superconductivity demand updated theories to be properly described. Fortunately, SRF science primarily relies on "conventional" superconductors, allowing the field to generally operate within the more established and well-tested theories. For this work in particular, only an introductory overview of the foundational Bardeen-Cooper-Schrieffer (BCS) theory [BCS57] will be needed.

2.1.1 Basics of BCS Superconductivity

Superconductivity was first discovered by H.K. Onnes in 1911 while studying the resistance of mercury. When a mercury sample was cooled to about 4.2 K, he observed the resistance suddenly drop to "almost zero". A copy of the historic plot showing the sample's resistance as a function of temperature can be seen in Figure 2.1 [vDK10]. This discovery was made possible by Onnes' successful liquefaction of helium in 1908, which has a boiling point of 4.2 K at atmospheric pressure. Though mercury was certainly a fortuitous choice of material to study given the temperature at which it becomes superconducting, Onnes' experimental setup was actually able to reach a temperature of about 1.8 K thanks to a pumping system which could lower the vapor pressure of the liquid helium below atmospheric (thus decreasing its temperature below 4.2 K) [vDK10]. Still, many elements either have no observed superconductivity or only transition at even lower temperatures, showing that sometimes a touch of luck can contribute to major scientific progress (or at least can provide a fortunate shortcut).

Modern, highly sensitive experiments have more recently determined the upper

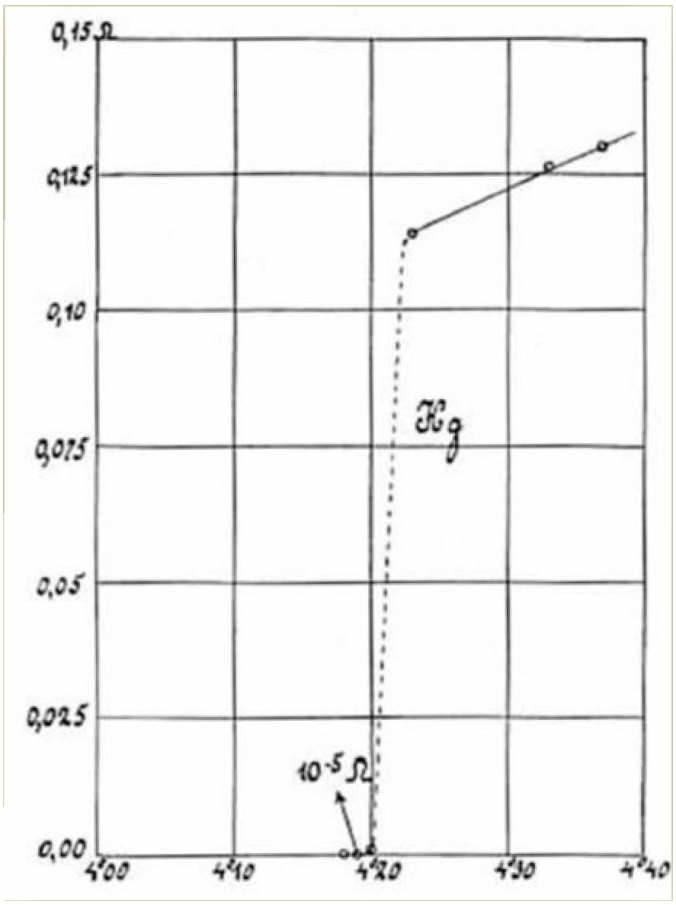

Figure 2.1: Plot of resistance (Ohms) versus temperature (K) for the mercury sample studied in Onnes' famous experiment in 1911. The superconducting transition can be seen as measured just above 4.2 K [vDK10].

limit of the ratio between the resistivity of a superconductor ρ_s to its normal conducting resistivity ρ_n to be [PKH08]

$$\frac{\rho_s}{\rho_n} < 10^{-12}.$$

In practice, a superconductor is considered to have zero resistance to a constant current. It took about 40 years after the initial discovery of superconductivity for physicists to develop new theories that could sufficiently explain the remarkable phenomenon. Ginzburg-Landau theory was published in 1950, providing a phenomenological description of superconductivity [GL50], while the microscopic theory of Bardeen-Cooper-Schrieffer (BCS) was completed in 1957 [BCS57]. As men-

tioned previously, this work will focus primarily on BCS theory, following a similar (though abbreviated) approach to its introduction as that found in [PKH08].

At the heart of BCS theory is the concept of normal conducting electrons condensing into a new state made up of "Cooper pairs". This transition occurs due to an attractive potential between electrons generated from their interactions with vibrations in the material's lattice structure – this is referred to as the electron-phonon interaction. At a critical temperature, T_c, this attractive potential overcomes the usual repulsive Coulomb potential, resulting in the formation of the Cooper pairs. This interaction creates a state with lower total energy; thus the superconducting state is energetically favorable and an energy gap, denoted by $\Delta(T)$, is formed. This energy gap corresponds to the amount of energy required to break a Cooper pair ($2\Delta(T)$ breaks a pair). The energy gap of an ideal superconductor at $T = 0$ was derived in BCS theory to be

$$2\Delta(T = 0) = 3.528 k_{\mathrm{B}} T_c, \tag{2.1}$$

where k_{B} is the Boltzmann constant [BCS57]. In real superconductors, the value of the energy gap varies by material and depends on the strength of the electron-phonon interaction.

The paired electrons can move through the lattice structure unimpeded, such that they create a "supercurrent" which screens any fields from the remaining normal conducting electrons[2]. This collision-free movement is possible due to the long-range nature of the pairing mechanism. The coherence length ξ_0 of a super-

[2]For any finite $T > 0$, only a fraction of the total electrons are paired. In particular, the number of *normal* electrons remaining is given by [PKH08]:

$$n_{normal} = \exp\left(-\frac{\Delta}{k_{\mathrm{B}} T}\right).$$

conductor describes the spatial extent of each Cooper pair and is given by

$$\xi_0 \sim \frac{\hbar v_F}{k_B T_c}, \tag{2.2}$$

where $\hbar$ is Planck's constant and v_F is the Fermi velocity of the electrons [Tin96]. Conventional superconductors described by BCS theory have coherence lengths much larger than the atomic spacing of their lattice structures, allowing the Cooper pairs to effectively "ignore" the lattice ions that normal electrons would scatter off of – this enables the characteristic zero DC resistance.

The advantage of infinite conductivity does not, however, carry over when the fields applied to a superconductor begin to oscillate. Conceptually, this is because Cooper pairs still have finite inertia even if they can move without friction. As such, they cannot instantly accelerate as would be needed to perfectly screen the normal conducting electrons from the oscillating external fields. In particular, an external magnetic field will penetrate a short distance into the superconductor with an exponentially decaying amplitude given by

$$H(x) = H_0 e^{-x/\lambda}, \tag{2.3}$$

where H_0 is the amplitude at the surface, x is the depth into the superconductor, and λ is a material parameter known as the penetration depth. For a superconductor without impurities, the penetration depth can be derived in London theory as

$$\lambda_L = \sqrt{\frac{mc^2}{4\pi n e^2}} \tag{2.4}$$

where m is the electron mass, c is the speed of light, n is the density of normal conducting electrons and e is the electron charge. The penetration depths for the superconducting materials relevant to this study are on the order of several tens of nanometers – thus the fields are confined to a very small region at the surface

of the superconductor. Comparisons of specific values can be found in the next section of this chapter.

The normal (unpaired) electrons near the surface are thus also acted on by the oscillating fields, resulting in a small yet measurable resistance – typically on the order of nΩ for RF fields. A basic formulation of this surface resistance can be broken up into two primary components [PKH08]:

$$R_s = R_{\mathrm{BCS}}(T, H) + R_0(H) \tag{2.5}$$

where $R_{\mathrm{BCS}}(T, H)$ is the temperature-dependent resistance as predicted by BCS theory and $R_0(H)$ is the field-dependent residual resistance. A simplified expression for R_{BCS}, accurate for $T < T_c/2$, is given by [PKH08]

$$R_{\mathrm{BCS}} = A\frac{f^2}{T}\exp\left(-\frac{\Delta(T)}{k_{\mathrm{B}}T}\right), \tag{2.6}$$

where A is a material-dependent constant and f is the frequency of the applied field. While the original formulation of BCS theory does not account for any field-dependence of this component, recent experiments have shown that such a dependence exists for certain material conditions [G$^+$17, Man20], and theoretical work has sought to address this fact [XRK13, Gur14]. The residual resistance $R_0(H)$ is what remains at low temperature as $R_{\mathrm{BCS}} \to 0$. There are various sources that can contribute to the residual resistance, but one of the most important is trapped magnetic flux. Although ideal superconductors expel all magnetic fields[3], defects in the material can cause localized suppression of superconductivity. These locations act as potential "pinning" sites for magnetic flux, which then generate more losses when exposed to oscillating external fields [PKH08].

[3]This is the well-known Meissner effect, which is also a result of the formation of supercurrents at the transition to the superconducting state. These supercurrents not only screen any external fields that are applied to the superconductor, but also expel any fields that were already present inside the material when it was normal conducting.

In addition to contributing to RF resistance, an applied magnetic field (constant or oscillating) can also suppress superconductivity and the Meissner effect (flux expulsion) if the field is strong enough. The nature of this breakdown depends on the type of superconductor; conventional superconductors can be categorized as type-I or type-II. For type-I, there is a single critical field H_c, above which superconductivity is lost [Tin96]. For type-II, to which the materials used in this work belong, there are two primary critical fields, H_{c1} and H_{c2}. Above H_{c1}, it is energetically favorable for magnetic flux to exist in the superconductor in quantized bunches known as magnetic vortices. These vortices have a normal conducting core surrounded by a supercurrent, such that superconductivity still exists between the vortices. This is referred to as the vortex state. The density of vortices increases with the applied field, until the vortex cores begin to overlap and superconductivity is lost at H_{c2} [Tin96, PKH08].

Fortunately for SRF applications, which will be discussed further throughout the rest of this work, there is another field limit known as the superheating field H_{SH} which relies on a form of metastability. Focusing on type-II superconductors, while it is energetically favorable for the magnetic vortices to *exist* above H_{c1}, there is an additional energy cost for the vortices to actually form and enter the material. This provides an additional energy barrier which prevents the vortices from entering until $H_{\mathrm{SH}} > H_{c1}$ is reached [PKH08]. The superheating field sets the effective limit for SRF applications, as the entrance of magnetic vortices throughout the whole superconductor would generate prohibitive losses when exposed to the oscillating fields[4]. The different superconducting phases and corresponding field limits for a type-II superconductor are shown in Figure 2.2.

[4]Note that the previously mentioned trapped flux during cooldown is a more local effect, resulting in much fewer vortices compared to the global effect of vortex entry above H_{SH}. Thus an SRF cavity can still operate with some residual losses from trapped flux, but cannot realistically operate above H_{SH}.

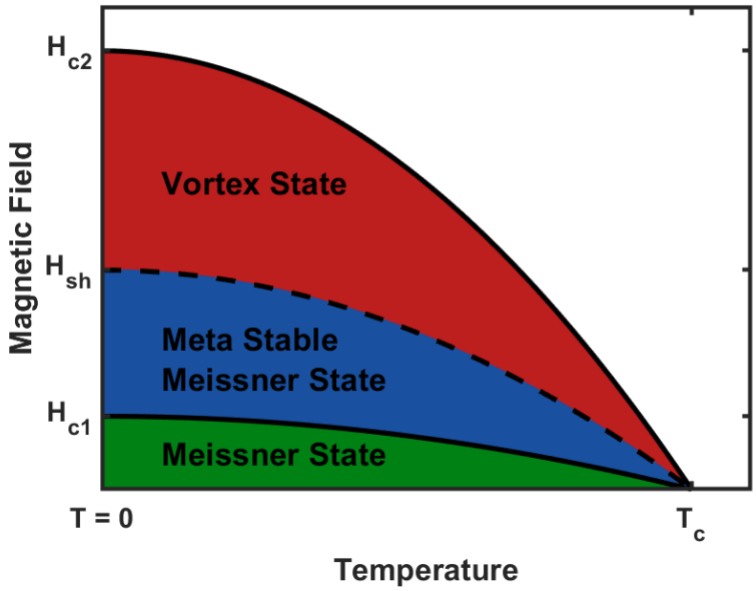

Figure 2.2: Phase space diagram for a type-II superconductor showing the temperature-dependent magnetic field limits of the three main phases: Meissner state (standard superconductivity), metastable Meissner state and vortex state. This diagram first appeared in [Por21].

2.1.2 Superconducting Radio-Frequency

The field of superconducting radio-frequency (SRF) pertains to the application of superconducting technology to RF (microwave) resonant structures. Of particular interest to this work is the study of accelerating cavities which can be used to accelerate and energize charged particles. This is achieved by exciting electromagnetic fields inside a resonant cavity such that the electric fields point along the beam axis, accelerating the particles as they pass through the cavity. Meanwhile, the magnetic fields lead to resistive losses in the cavity, as previously discussed. These fields are excited by sending RF power to a forward power coupler (FPC) on one end of the cavity. For speed-of-light particles, the cavity typically has an approximately elliptical cross-section which is optimized to improve the field geometry and reduce losses. A simple schematic can be seen in Figure 2.3. Further

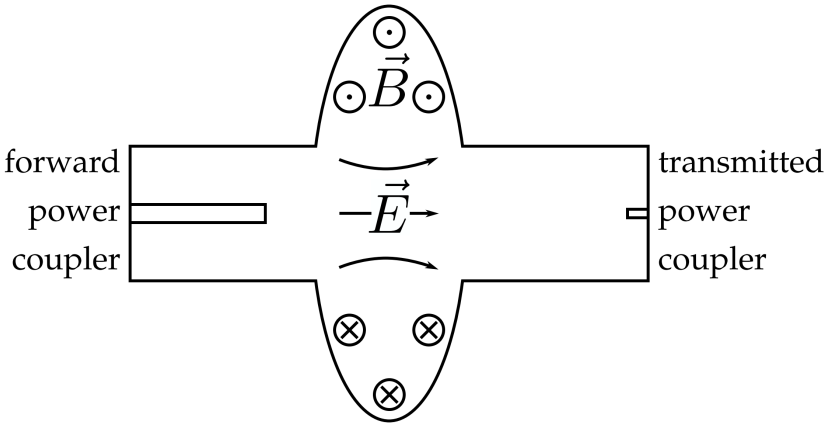

Figure 2.3: Schematic of an accelerating cavity with excited electric fields ($\vec{E}$) parallel to the beam axis and magnetic fields ($\vec{B}$) circling around the cavity. These fields are excited by the forward power coupler shown on the left side. The transmitted power coupler on the right can be used during cavity testing to monitor the fields. This diagram first appeared in [Man20].

details about measuring the excited fields and the cavity's response can be found in the last section of this chapter.

In addition to fundamental R&D conducted using individual cavities, the field of SRF also encompasses the design, construction and operation of complete superconducting accelerator systems. As described in the introduction, accelerators in general have a wide range of crucial applications, from fundamental science to medicine, security and industry. Many of these accelerators benefit from or entirely rely on superconducting cavities to meet their performance requirements. For example, many cutting-edge applications require high average beam currents which can only be obtained with an accelerator operating in continuous-wave (cw) mode. In this case, normal conducting copper cavities are typically restricted to accelerating fields of just 1 MV/m to avoid excessive heating which can degrade the vacuum or damage (even melt) the cavities, while superconducting cavities can maintain high fields of tens of MV/m without any (fundamental) issues [PKH08].

Operating at much higher fields allows the length of the accelerator to be reduced significantly for a targeted beam energy, greatly reducing costs[5]. With such low surface resistance, the losses in a superconducting cavity are negligible compared to the energy transferred to the beam. This helps reduce the operational cost of powering the accelerator. In addition, the low resistive losses allow the cavity aperture to be increased while still maintaining high accelerating fields. This provides a variety of benefits for beam quality, such as reducing the effect of detrimental higher-order modes and wake-fields [PKH08].

The main drawback of using superconducting cavities is the cooling requirement, as the cavities must operate at 2 - 4 K to achieve high quality factors. Even with this added cost, using superconducting cavities results in a lower net energy consumption for large-scale machines. For example, consider a generic linear accelerator that has a targeted beam energy of 10 GeV with a requirement to operate in cw mode. The approximate power dissipated in the accelerating cavities is given by

$$P \propto \frac{E_{\text{acc}}^2 * L_{\text{eff}}}{Q_0}, \tag{2.7}$$

where E_{acc} is the accelerating gradient, L_{eff} is the effective accelerating length, and Q_0 is the cavity quality factor[6]. Copper cavities have $Q_0 \approx 10^4$, and a limit of 1 MV/m in cw requires an accelerating length of about 10 km. This results in a total cavity wall loss of about 1 GW. By comparison, superconducting cavities can reach fields of about 20 MV/m with $Q_0 \approx 2 \times 10^{10}$, thus only needing an accelerating length of 500 m. This results in a dissipated power of about 10 kW; it takes about 800 W to extract 1 W at 2 K (see Figure 2.4), giving a total cooling power requirement of 8 MW. Thus a superconducting accelerator will have a lower

[5]Or conversely, makes higher beam energies achievable given practical restraints on the size of the accelerator and project budget.

[6]Other factors such as the shunt impedance are left out to simplify the comparison.

net energy consumption even with the large cooling cost.

Niobium is currently the main material used for SRF cavities, in large part due to it having the highest critical temperature of any pure element at 9.2 K. With this T_c, niobium cavities can operate efficiently at about 2 K, which can be achieved by pumping liquid helium below atmospheric pressure. This temperature is determined as an optimal balance between decreasing the BCS component of the surface resistance (see Equation 2.5) and decreasing the cryogenic cooling efficiency. Another key benefit of niobium is its malleability; especially at higher purities used in accelerating cavities, niobium is soft enough to be pressed or drawn into shape using dies. This is beneficial given the complicated shapes that RF cavities can require. In addition, niobium is a type-II superconductor, meaning it can operate stably up to its superheating field $H_{\mathrm{SH}} \approx 200\,\mathrm{mT}$ [VL11].

2.2 Alternative material: Nb_3Sn

As niobium cavities approach the theoretical limits of their achievable RF performance thanks to highly optimized surface treatments, there is great interest in studying new materials for SRF cavities which can surpass the limits of niobium. This includes not only demonstrating such performance in an R&D setting, but also proving that the performance can be reproduced reliably such that it is ready for implementation in a full-scale accelerator. One of the most promising materials to reach these goals is Nb_3Sn, a niobium alloy containing (ideally) 25 atomic percent tin [PH17]. Due to the brittleness of this material, it is impractical to make an entire cavity out of Nb_3Sn; instead, a thin film is typically formed on a bulk niobium or copper cavity. For brevity, the remainder of this work will refer

to a bulk niobium cavity coated with Nb_3Sn as a Nb_3Sn cavity (unless otherwise specified).

This section relies heavily on the dissertations of previous Cornell SRF graduates who led the primary Nb_3Sn research program [Pos14, Hal17, Por21]. The discussion to follow will be a significantly abridged version of what can be found in those publications, only covering what is directly needed for the remainder of this work.

2.2.1 Material Properties

The two most appealing properties of Nb_3Sn are a superconducting critical temperature of 18 K [God06] and a theoretically predicted superheating field of 425 mT [CS08]. These are both approximately double the corresponding values for pure niobium, as shown in Table 2.1. A T_c of 18 K allows Nb_3Sn cavities to operate efficiently at a temperature of 4.2 K, compared to an operating temperature of $\sim$2 K for niobium. Though this difference may not sound like much, being able to cool the cavity with atmospheric liquid helium, rather than sub-atmospheric, simplifies the required infrastructure and also increases the cooling efficiency. This is shown in Figure 2.4 [Hal17]. The left plot shows the cooling efficiency of a large cryoplant (such as those installed for LCLS-II), in which there is a factor of 3-4 difference from 2 K to 4.2 K. The right plot also takes into account the dissipated power per $(MV/m)^2$ in niobium and Nb_3Sn cavities, showing that an energy savings of 60-80% for a given working accelerating gradient is possible with Nb_3Sn cavities. Meanwhile, a higher superheating field corresponds to a higher theoretically attainable accelerating gradient. Thus, for a given targeted beam energy, the total length of a linear accelerator could be reduced by up to a factor of two by using

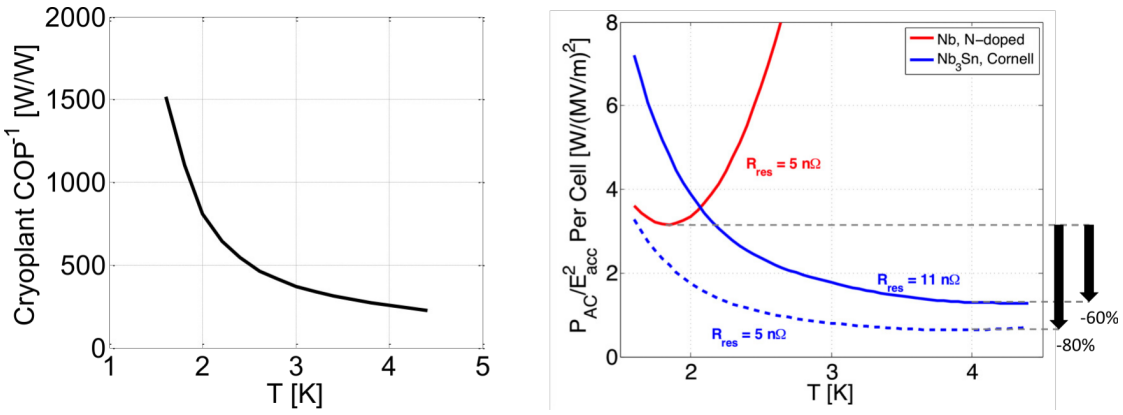

Figure 2.4: Left: inverse coefficient of performance (COP) for a large-scale cryoplant, indicating the amount of wall power required to extract 1 W from the cold region. Right: Cryoplant wall power per cell per $(\mathrm{MV/m})^2$ to operate a 1.3 GHz cavity (TESLA-shape). This figure was originally published in [Hal17].

Nb_3Sn cavities[7].

Also included in Table 2.1 are the penetration depth λ and coherence length ξ for the two materials. A larger penetration depth indicates that the applied magnetic fields will penetrate further into the RF surface for Nb_3Sn compared to niobium, while a shorter coherence length makes Nb_3Sn more sensitive to defects. Figure 2.5 shows a comparison of the thermal conductivites for niobium and Nb_3Sn. Across the temperature range shown, Nb_3Sn thermal conductivity is $> 10^3$ times worse than that of niobium. This means that Nb_3Sn is more susceptible to thermal instability, and is another reason that growing thin films of Nb_3Sn on a niobium or copper substrate is required. Overall, Nb_3Sn as an SRF material offers significant advantages in terms of higher operating temperature and higher theoretical limits on the accelerating gradient, while trading in greater susceptibility to defects and worse thermal stability.

[7]Assuming the cavities were to operate at their theoretical limits.

Parameter	Nb	Nb_3Sn	Units
T_c	9.2	18	K
H_{SH}	219	425	mT
λ	50	111	nm
ξ	22	4.2	nm

Table 2.1: Key superconducting parameters for niobium and Nb_3Sn. The values listed are meant as illustrative examples, and will vary depending on the mean free path of the material.

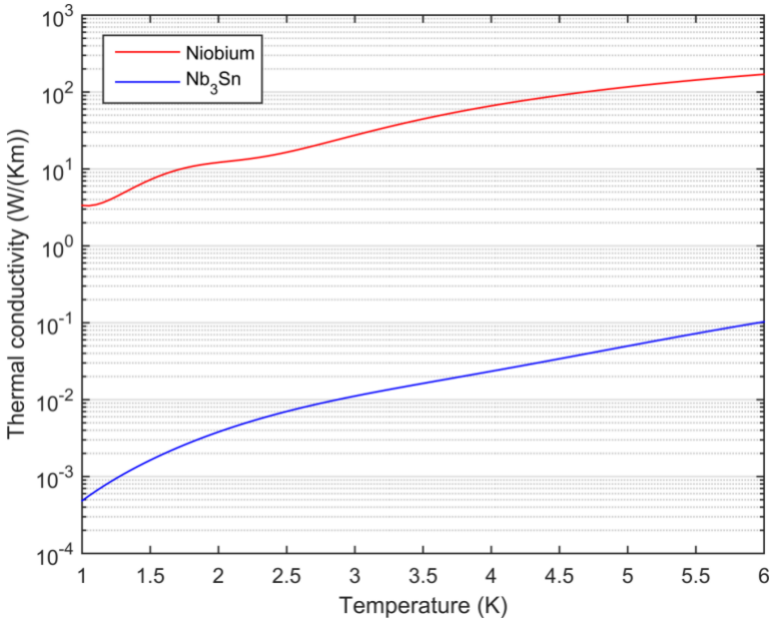

Figure 2.5: Plot of the temperature-dependent thermal conductivity k for Nb_3Sn and 300 RRR niobium. This figure first appeared in [Hal17] with Nb_3Sn data from [CC64] and niobium data from [KB96].

2.2.2 Film Growth

To date, the most reliable method for growing Nb_3Sn films for SRF cavities is thermal vapor diffusion. Generally speaking, this is done by coating a niobium cavity with tin vapor in a high vacuum furnace, then allowing the tin to diffuse into the bulk niobium to form Nb_3Sn. This method was pioneered at Siemens AG in Germany, in which 10 GHz cavities were coated and tested [HMP+75]. Studies on

larger cavities (e.g. 1.5 GHz) were later performed at the University of Wuppertal [HGM+84]. While these studies produced important early results, the cavity performance typically fell short of expectations. This led to a general loss of interest in Nb_3Sn research for many years, until a new program was started at Cornell in 2009 [PL11, PLX11]. This new research produced Nb_3Sn cavities which surpassed the limitations seen in the earlier works, kicking off new interest in the development of high-performing Nb_3Sn cavities [PL14]. For example, similar R&D programs later began at Thomas Jefferson National Laboratory (Jefferson Lab) [EKR+15] and Fermi National Accelerator Laboratory (Fermilab) [PMRT15], with added interest in applying Nb_3Sn coatings to multi-cell cavities. An especially thorough recounting and discussion of the historical and current Nb_3Sn research programs can be found in [Hal17].

A diagram of the Nb_3Sn coating furnace used at Cornell is shown in Figure 2.6 [Pos14, Hal17]; this furnace design was adapted from the one used at Wuppertal [HGM+84]. The coating furnace consists of a niobium coating chamber placed inside a larger ultra high-vacuum furnace. The lower section of the vacuum furnace (labeled "Hot Zone" in the figure) heats up the bottom portion of the coating chamber where the cavity sits. In a small enclave below the main coating chamber is a secondary hot zone with an independent heater. A tin source is set inside this secondary hot zone so that its temperature can be raised higher than that of the cavity. This allows the tin evaporation rate and niobium-tin reaction rate (determined by cavity temperature) to be controlled independently. Just inside where the cavity sits is a $SnCl_2$ source which acts as a nucleating agent prior to the main coating. Heat shields are lowered into the coating chamber and sit just above the cavity to reduce heating of the upper portion of the coating chamber, which acts as a thermal transition. The top portion of the coating chamber is

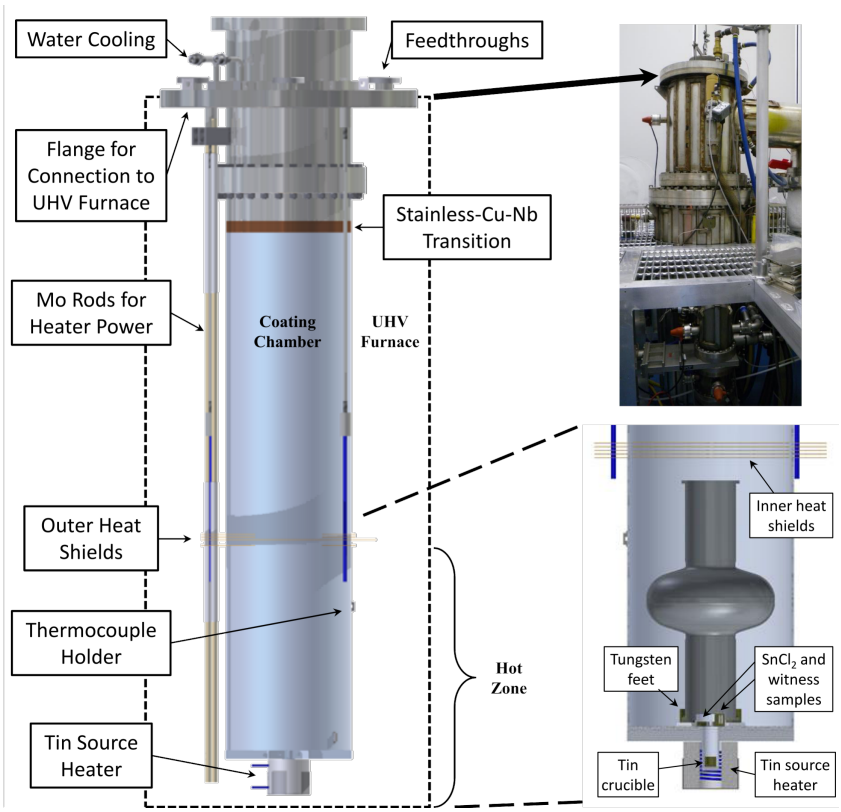

Figure 2.6: Diagram of the Nb_3Sn coating chamber used at Cornell. The coating chamber is installed in a vacuum furnace which heats up the bottom portion of the chamber where the cavity is located. A secondary heater can increase the tin source temperature above that of the chamber and cavity. This figure first appeared in [Hal17], which was adapted from [Pos14].

made of stainless steel and seals the coating chamber to the vacuum furnace.

While there are many parameters to adjust to try to improve the results of a coating run, this work will simply summarize the standard coating process used at Cornell (at time of writing). After pumping down the vacuum furnace and coating chamber, the following steps are taken [Por21]:

1. Degas: Chamber is warmed to 180 °C for 24-48 hrs to remove residual moisture and any other contaminants that would otherwise outgas from the chamber or cavity during coating.

2. Nucleation: Chamber is warmed to 550 °C for 5 hrs to vaporize the $SnCl_2$ in order to coat the cavity with small droplets of tin which act as nucleation sites.
3. Temperature ramp: Secondary heater is activated to form a temperature gradient between the tin source and cavity. Once this gradient reaches 270 °C, the chamber temperature is increased to 1150 °C while maintaining the temperature gradient (thus the tin source reaches a temperature just above 1400 °C).
4. Coating: The high temperatures at the end of the ramp are held for 1.5 hrs in which the main coating process occurs.
5. Annealing: The secondary heater is turned off while the chamber temperature is held for another hour. This allows any excess tin to be absorbed after decreasing the tin vapor pressure.
6. Cool down: Both heaters are turned off and the coating chamber and cavity are allowed to naturally cool down.

The plot on the left of Figure 2.7 shows a temperature profile of the standard coating described above (excluding the degas). The orange curve corresponds to the cavity temperature while the blue curve represents the temperature of the tin source. The image to the right is an SEM scan of a typical Nb_3Sn coating produced by this process, showing individual grains of size $\sim$1 µm.

2.2.3 State-of-the-Art Performance

Since 2013, Nb_3Sn cavities have been improved to the point of operating at 4.2 K at 15 MV/m or higher while still maintaining a high Q_0 of $1 - 2 \times 10^{10}$ (see e.g.

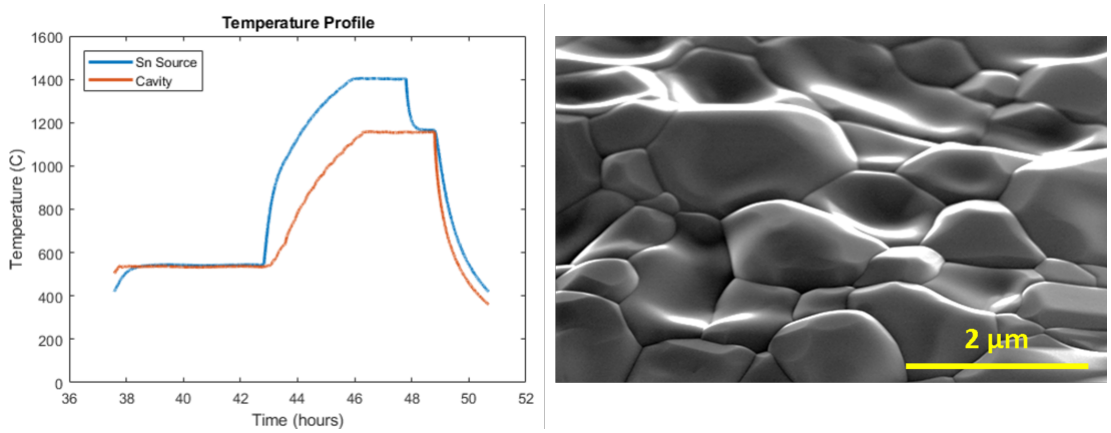

Figure 2.7: Left: temperature profile for the standard Nb_3Sn coating process used at Cornell; this image first appeared in [Por21]. Right: SEM image of a typical Nb_3Sn film surface produced by the standard coating process; this image first appeared in [Pos14].

[Pos14, Hal17, Por21, PH17, PCE+19, PLS+21]). These high Q_0 values correspond to a very small cavity heat load of less than one Watt for a single-cell 1.3 GHz cavity. Research on improving Nb_3Sn films is an ongoing effort, but the performance cited here is quite reliably achievable. Figure 2.8 shows recent state-of-the-art results from Cornell [Por21], Fermilab [PLS+21] and Jefferson Lab [PCE+19] as examples of such performance.

It is worth noting that optimal Nb_3Sn cavity performance relies on minimizing the thermal gradients across the cavity during cooldown, particularly during the superconducting transition. Due to the thermoelectric effect, the bi-metal structure of Nb/Nb_3Sn will generate thermoelectric currents in the presence of a thermal gradient [Hal17]. These currents then generate magnetic fields which get partially trapped in the cavity walls as the cavity cools through T_c. This trapped magnetic flux contributes to an increase in the residual resistance, leading to worse cavity performance [Hal17, MD19]. For this reason, Nb_3Sn cavities are typically cooled very slowly near T_c with a thermal gradient of no more than 200 mK/m across the cavity [Hal17].

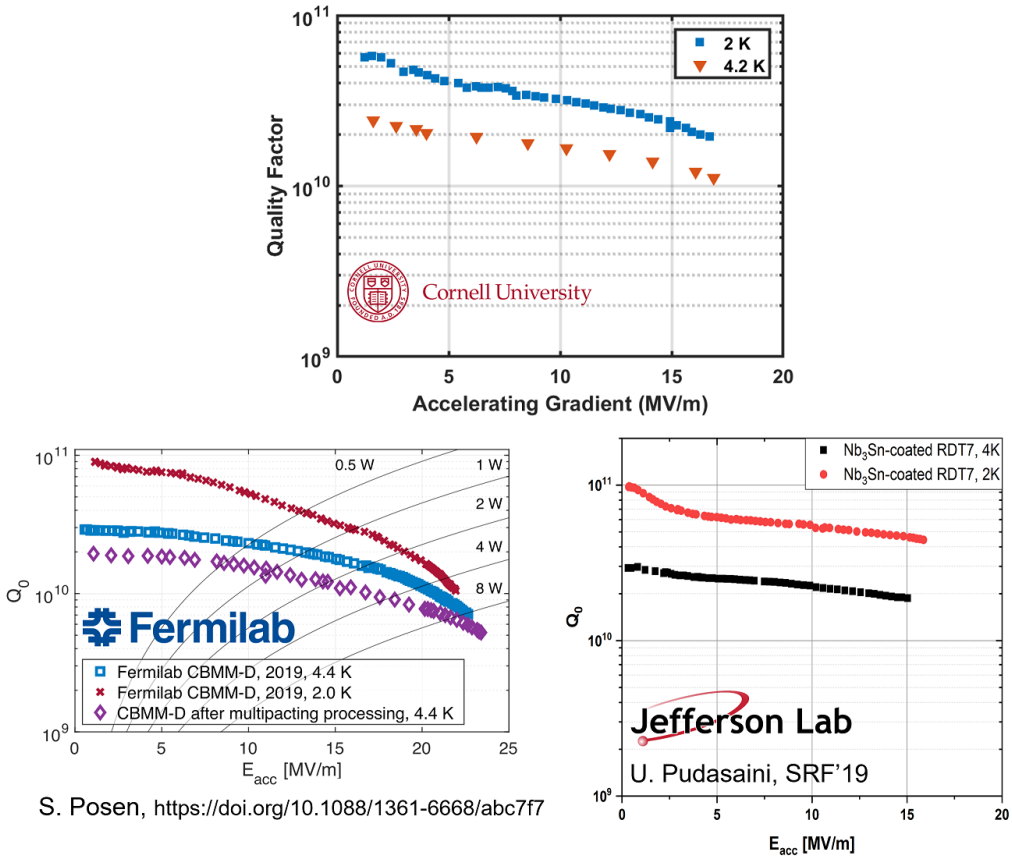

Figure 2.8: Recent state-of-the-art Nb_3Sn cavity performance from Cornell University [Por21], Fermilab [PLS+21] and Jefferson Lab [PCE+19]. Results are for single-cell 1.3 - 1.5 GHz cavities. A key takeaway is that Nb_3Sn cavities can reliably reach accelerating gradients >15 MV/m with Q_0 >1×10^{10}.

2.3 Cavity Measurement and Metrics

Whether a cavity is being used for R&D or is part of production for an accelerator, the cavity must be tested by exposing it to RF fields and measuring the response. So-called vertical testing is the foundation of this process. This testing provides various measurements of the cavity performance, which can be used to determine the effectiveness of a new treatment method in R&D or whether the cavity meets the qualification requirements for accelerator production. In general, the cavity testing process (including clean room preparation but excluding treat-

ment processes) takes ∼1 week for a shorter test with just one cooldown; tests with multiple cooldowns may take a couple extra days.

2.3.1 Cavity Vertical Testing

Prior to testing, cavities will receive a combination of various treatments to improve RF performance. These almost always include some amount of chemical etching and vacuum bake, and may also include a special material coating or a doping / infusion procedure. These processes have been well-discussed in previous works, e.g. [Man20, Por21], and will not be treated extensively here; the Nb_3Sn coating process discussed in the previous section is sufficient for this work.

Once cavity treatments are completed, the final test preparation is performed in a cleanroom located in the Newman Lab basement. This cleanroom has Class 10 areas in which the cavities are prepared in order to minimize the risk of dust contamination. With the high fields that get excited in the cavities during testing, even a single dust particle can significantly affect the cavity performance. The standard cleanroom preparation consists of: two high-pressure DI-water rinse cycles to provide a final cleaning of the RF surface (one with the cavity completely open, one with only the bottom flange left open), assembly onto a test pit insert, pumping down the cavity to vacuum, and leak checking the cavity and insert. Particularly after the HPR cycles are completed, extreme care must be taken when working with the cavity to avoid any contamination. Once the cavity is sealed and under vacuum with no leaks, the test insert can be removed from the cleanroom for the final test preparation steps.

Once outside the cleanroom, temperature and magnetic field sensors are at-

tached to the cavity. For elliptical cavities, three Lakeshore Cernox sensors [Cry23] are used with one at the cavity equator and each iris. These sensors are used to measure the cavity temperatures both during cooldown and RF testing. Two or more flux gates (Mag-01H Type F Magnetometers from Bartington) are used to measure the magnetic fields at the cavity during cooldown; these are oriented vertically at the equator and top iris of the cavity. An example of a prepared cavity and test insert can be seen in Figure 6.8. Once the sensors and auxiliary instrumentation has been added, the insert is lowered into one of the test pit dewars, pumped down to vacuum, and cooled down to 4.2 K by adding liquid helium to the dewar. The superconducting transition is tracked using both the temperature sensors and by watching for a sudden jump in the flux gate readings, which is the result of (sometimes partial) flux expulsion.

Once the cavity is cooled down, RF testing can begin. RF cables connect the cavity to a phase-locked loop consisting of a signal generator, frequency counter, mixer, phase shifter, power meters and various directional couplers and amplifiers – see Figure 2.9. The cable attenuations are measured in order to correct the raw power meter measurements. The phase-locked loop ensures that the signal sent to the cavity remains locked on to the cavity's resonant frequency. This is necessary due to modulation of the resonant frequency caused by vibrations in the cryostat which slightly alter the cavity shape – this phenomenon is referred to as microphonics. Though this frequency modulation is small (often on the order of tens of Hz), the cavity bandwidth is even smaller: < 1 Hz for a 1.3 GHz cavity with a loaded quality factor $\sim 1 \times 10^{10}$. The mixer and phase shifter are two of the key components for locking onto the cavity frequency. The mixer compares the phases of the forward and transmitted power signals and sends a DC signal to the generator based on the difference. The phase shifter is used to remove any phase

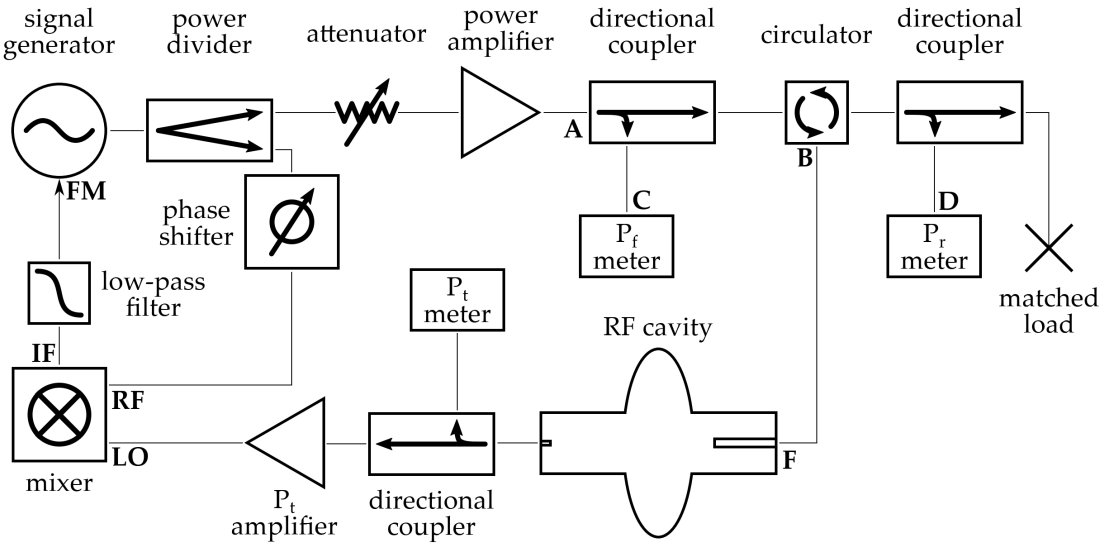

Figure 2.9: Diagram of the phase-lock loop circuit used for vertical testing of cavities at Cornell. This diagram first appeared in [Man20].

difference in the signals that comes from the different cable lengths, such that the mixer can effectively compare the phases at the cavity. A detailed analysis of the mathematics of the phase-locked loop is presented in [Man20].

2.3.2 Key Metrics and Parameters

As described in the phase-locked loop setup, the only quantities measured directly during RF testing are the signal frequency and the forward, reflected and transmitted powers. The rest of this section will cover how these four measurements[8] are used to calculate two primary cavity metrics: the cavity quality factor Q_0 and the accelerating gradient E_{acc}. While there are other metrics of interest for detailed R&D, these two will provide adequate characterization for this work. Some of these calculations also require the use of special cavity parameters which are sep-

[8] Actually three, as the transmitted power signal does not have a correcting attenuation measurement and thus is not used in the main calculations.

arately extracted from RF simulations of the cavity being tested. The derivations described will primarily follow and summarize the method used in [PKH08].

First consider a cavity being driven in steady state such that it contains some total electromagnetic energy U_0. When the RF drive is turned off, the energy in the cavity will decrease due to a combined power loss given by

$$P_{\text{tot}} = P_{\text{diss}} + P_e + P_t, \tag{2.8}$$

where P_{diss} is the power dissipated in the cavity walls, P_e is the "emitted" power that leaks back out the forward power coupler, and P_t is the power that leaks out the transmitted power coupler. In vertical tests, the transmitted power coupler is designed such that its contribution to the power loss is negligible compared to the others; thus this component will be ignored moving forward.

The energy decay is described by

$$U(t) = U_0 e^{-\omega t/Q_L} \tag{2.9}$$

where ω is the (angular) frequency of the oscillating fields inside the cavity and Q_L is known as the loaded quality factor defined as

$$Q_L \equiv \frac{\omega U}{P_{\text{tot}}}. \tag{2.10}$$

Thus, by measuring (a) the time constant of the energy decay[9] and (b) the frequency of the RF signal, the loaded quality factor of the cavity and coupler system can be calculated using Equation 2.9.

However, the intrinsic quality factor Q_0 of the cavity is typically of greater interest during testing, as it corresponds to how much power is dissipated in the

[9]This is done using the P_e power meter, since the time constant is the same for the whole system.

cavity itself:

$$Q_0 \equiv \frac{\omega U}{P_{\text{diss}}}. \tag{2.11}$$

To extract Q_0 from Q_L, an additional quality factor Q_e associated with the emitted power is defined by

$$Q_e \equiv \frac{\omega U}{P_e}. \tag{2.12}$$

Combining the quality factor definitions (Eqs. 2.10 - 2.12) with Equation 2.8 gives a new relation,

$$\frac{1}{Q_L} = \frac{1}{Q_0} + \frac{1}{Q_e} \tag{2.13}$$

(recall that P_t is negligibly small). Defining a new quantity known as the coupling factor

$$\beta \equiv \frac{Q_0}{Q_e}, \tag{2.14}$$

Equation 2.13 can be rearranged to give

$$Q_0 = Q_L(1 + \beta). \tag{2.15}$$

Thus the intrinsic quality factor can be calculated from the loaded quality factor and coupling factor. The coupling factor can be determined either in steady state or when the RF drive is turned off using different relations between the forward and reflected (or emitted for RF off) powers [PKH08]. Cornell's vertical testing software calculates both values and uses the average for calculating Q_0.

To determine the accelerating gradient E_{acc}, the power dissipated in the cavity walls, P_{diss}, must be calculated during steady state. This is given by the formula

$$P_{\text{diss}} = \frac{4\beta}{(1+\beta)^2} P_f. \tag{2.16}$$

This can then be used along with the calculated Q_0 and measured RF signal frequency ω to calculate the total energy U in the cavity during steady state using

Parameter	LTE	STE	ERL 2-cell	LCC1-1	Units
Freq.	1300	2600	1300	1300	MHz
G	278	278	–	263	Ω
R/Q	105	105	218	106	Ω
$E_{pk}/\sqrt{U}$	15.1	42.3	–	16.7	$(MV/m)/\sqrt{J}$
E_{pk}/E_{acc}	1.86	1.86	1.94	2.06	–
B_{pk}/E_{acc}	4.23	4.25	4.28	4.44	mT/(MV/m)

Table 2.2: Key parameters for various cavity types relevant to this work: 1.3 GHz TESLA-shape (LTE) [A+00], 2.6 GHz TESLA-shape (STE), Cornell ERL 2-cell injector cavities [SBG+03], LCC1-1.

Equation 2.11. Special cavity parameters $E_{pk}/\sqrt{U}$ and E_{pk}/E_{acc} can then be used to calculate the accelerating gradient from the cavity energy, where E_{pk} is the peak surface electric field in the cavity. These parameters, which are typically calculated via RF simulation software, are listed in Table 2.2 for different cavity geometries relevant to this work. As a general rule of thumb, a 10% error is assumed for Q_0 and E_{acc} calculations. This comes from a combination of RF cable attenuation measurement error as well as systematic uncertainty from the variety of electric circuit components used [PKH08].

Other important parameters listed in the table (also calculated in RF simulations) are G, the geometry factor; R/Q, the shunt impedance; and B_{pk}/E_{acc}. The geometry factor is used to calculate the average surface resistance R_s of the cavity with the simple relation

$$Q_0 = \frac{G}{R_s}. \tag{2.17}$$

The shunt impedance measures how effectively the cavity can transfer energy to charged particles via an excited eigenmode, and scales with the number of cells in the cavity (unlike the other parameters) [PKH08]. Lastly, the parameter B_{pk}/E_{acc} converts between the accelerating gradient and the peak surface magnetic field. This can be used to plot certain quantities, particularly those related to resistance,

as a function of B_{pk} rather than E_{acc}. Of course, the only difference is a scalar factor so that is mostly a matter of preference.

CHAPTER 3

MOTIVATION FOR CONDUCTION-COOLED SRF

While the topics of fundamental SRF and some larger-scale applications have already been introduced, the work in this dissertation focuses on a slightly different branch of the field: small-scale applications or "compact SRF". As opposed to accelerators on the scale of kilometers, compact SRF seeks to develop superconducting accelerators on the scale of *meters*; these are sometimes also referred to as "table-top" accelerators. While the general notion of table-top accelerators is nothing new, the possibility of operating a meter-long superconducting accelerator at high power in a practical manner is. This chapter will briefly introduce some small-scale applications which offer particular interest for SRF technology, then present a key factor which makes compact SRF possible: recent improvements in the cooling capabilities of cryocoolers. The next sections will provide a summary of the materials which are required for conduction-cooled schemes to be feasible along with an overview of ongoing projects at other research facilities.

3.1 Small-scale Applications

Reports from the U.S. Department of Energy have identified a large number of applications which are ideal for small-scale accelerator operations [HS09, HW15]. These applications span a range of fields such as energy and environment, medicine, security/defense and industry; some examples of particular interest will be described in more detail below. Over 30,000 accelerators are already in use for such applications worldwide, with the number continuing to grow every year. As highlighted in the report "Accelerators for America's Future," pushing the forefront of these fields depends on extensive R&D to further the development of accelerating

systems which are "smaller, more compact but often high-power, more rugged, highly reliable, and less costly" [HS09].

In the fields of energy and environment, electron beams have been shown to be highly efficient in purifying drinking water, treating waste water and sewage sludge, and removing pollutants from flue gas e.g. from coal burning [HS09]. A few example projects discussed later in this chapter aim to develop new systems for various types of wastewater treatment. Electron accelerators provide high electrical efficiency, making them an attractive solution for these environmental applications. On a related front, high-power proton beams could be used to generate neutrons from a target which can then break down some of the most problematic radioactive isotopes in nuclear waste. This reaction could reduce the time required for nuclear waste to reach the same radioactivity as natural uranium to hundreds of years, from hundreds of thousands [HS09].

Compact accelerators are already widely applied in medicine, with uses ranging from diagnostics such as X-rays to treatments such as radiotherapy. However, a growing need in the field comes from radioisotope production. Radioisotopes are themselves used in a wide range of diagnostics and treatments in medicine, and their demand continues to increase. A delicate supply chain with little redundancy creates critical concern about the ability to continue meeting patients' needs in the future [HS09]. High power electron-beam based accelerators again provide a promising solution for establishing robust domestic production of these crucial radioisotopes.

Another application set to benefit from further development of compact, robust and high power accelerator systems is cargo inspection. Millions of cargo containers are unloaded every year at domestic seaports, yet only a small percentage are

scanned with X-ray or gamma-ray systems [Bli12]. New compact accelerators capable of producing high power X-rays could greatly increase the throughput of cargo inspection systems and lead to a much higher percentage of containers being scanned [HS09].

In industry, improved high-power electron beam accelerators can benefit a wide range of applications, such as using radiation for cross-linking plastics and rubber, performing metrology or wafer inspection in-line at production facilities, and improving sterilization of medical devices [HS09]. A couple projects introduced at the end of this chapter are developing systems meant for in-situ asphalt treatment and medical device sterilization. In general, compact accelerators producing high power electron beams would enable the construction of compact sources of hard X-rays in both academic and industrial facilities. Such a development has the ability to transform university and industrial research in biology, physics, materials science and environmental science, enabling the acceleration of new discoveries related to key technologies such as new batteries, photovoltaic systems, catalysts, high-performance alloys, oxide electronics, pharmaceuticals, carbon sequestration strategies, and drought-resistant crops [HS09].

A major benefit in developing new compact systems for these applications is that most of them require similar electron beam characteristics, namely high current and low to mid energy, operating in continuous-wave or long duty factor modes for high average power delivery – see Table 3.1. This makes it possible to investigate a "general-purpose" compact accelerator that could be implemented in a variety of the applications described, as is done in the primary research described in this dissertation.

Parameter	Value	Units
Energy	1 - 10	MeV
Current	100 - 1000	mA
Power	1 - 10	MW

Table 3.1: Typical Beam Parameter Range for Compact Accelerating Systems

3.2 Modern Cryocoolers

The previous section established that there is considerable interest in further developing small-scale accelerators for a wide variety of applications spanning the fields of energy and environment, medicine, security and more. Many of these applications could benefit from the more efficient, higher average power capabilities of SRF technology. Of course, such widespread implementation is not present today[1], even though SRF science in general is much further developed than what is required – so what is the main roadblock? The answer lies not in the accelerator itself, but in how it is cooled. Currently, superconducting cavities rely on liquid helium to extract RF heat loads during operation. While liquid helium is an extremely efficient coolant, it is also incredibly costly and complicated to use. Thus it is impractical for a small-scale operation to opt for superconducting technology, if that were to require liquid helium infrastructure which far surpasses the actual accelerating system in cost, complexity and maintenance needs.

A major part of the solution to this dilemma is provided by the recent advancements in the performance of commercial cryocoolers. A cryocooler is essentially a very powerful refrigerator capable of cooling desired system components down to cryogenic temperatures (usually defined as $< 120\,\mathrm{K}$). The cryocooler system typically includes a compressor unit responsible for driving the primary thermo-

[1] Arguably beneficial for the author, as this dissertation work would not be needed otherwise.

dynamic processes, a cold head unit with one or more cold plates (often referred to as "stages") which are cooled to cryogenic temperatures, and cryogenic lines which carry the working cryogenic fluid between the compressor and cold head. The cryocooler operates as a closed system, such that no additional cryogenics need to be added after it has been manufactured and delivered. There are several types of cryocoolers, such as Gifford-McMahon (GM) [Wal83a], pulse-tube (PT) [GL64] and Joule-Thomson (JT) [Wal83b]; the specific thermodynamic processes used in these cryocoolers vary, but that level of detail is beyond what is needed for this work.

While cryocoolers in general have existed for several decades, a new class of 4 K cryocoolers have only become available in the last 20 years or so. Even then, the first models were only able to extract about 0.5 W at 4.2 K – not nearly enough to use with an SRF cavity, especially at that time. Only after 10 more years of increasing cooling capacity, combined with huge improvements in the performance of Nb_3Sn cavities, have cryocoolers entered a new stage where they can be utilized as the primary cooling source for an SRF cavity. This convergence is illustrated in the left plot of Figure 3.1. The blue curve represents the 4.2 K cooling capabilities of pulse-tube cryocoolers from Cryomech (chosen as a representative example), while the red curve represents the amount of heat dissipated in a single-cell 1.3 GHz Nb_3Sn cavity at 4.2 K and 10 MV/m. As is evident in the plot, it was not until the early 2010's that this concept first became feasible. Since then, steady improvements have continued to push both fields such that the newest cryocoolers are capable of cooling multi-cell Nb_3Sn cavities.

With these developments, the possibility of replacing liquid helium altogether and instead cooling an SRF cavity with a cryocooler is well within reach. This

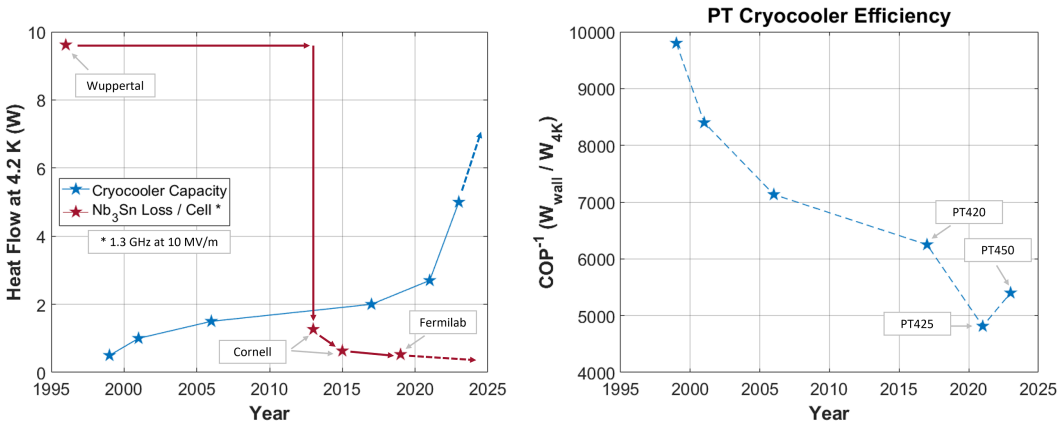

Figure 3.1: Left: plot showing the improvements in both cryocooler and Nb_3Sn cavity performance over the last ∼30 years. The cooling capacity values are for pulse-tube type cryocoolers from Cryomech [Blu24]. The Nb_3Sn losses are for single-cell 1.3 GHz cavities operating at 10 MV/m. Right: wall-power efficiency of 4.2 K pulse tube cryocooler models.

concept is illustrated in Figure 3.2, showing the current liquid helium infrastructure that would be required even for a small operation on the left, and a cryocooler compressor unit which can effectively replace it on the right. While this concept bridges the gap between SRF technology and small operations, cryocoolers are not meant to replace cryoplants for large-scale superconducting accelerators. This is due to the comparatively poor cooling efficiency of cryocoolers, as shown in the right plot of Figure 3.1. The most efficient 4 K cryocoolers still require about 5 kW wall power for every 1 W removed at 4.2 K, compared to large scale cryoplants which only require about 250 W wall power for the same cooling – see Figure 2.4.

In addition to being far less complex and costly than helium infrastructure, cryocoolers are also manufactured to be especially robust. For example, Cryomech's pulse tube cryocoolers only have scheduled maintenance every 20000 operational hours, which can be performed without professional servicing [Blu24]. In addition to being low-maintenance, the operation of the cryocooler does not require any expertise either. In fact, cryocoolers are designed for turn-key or "push-to-start"

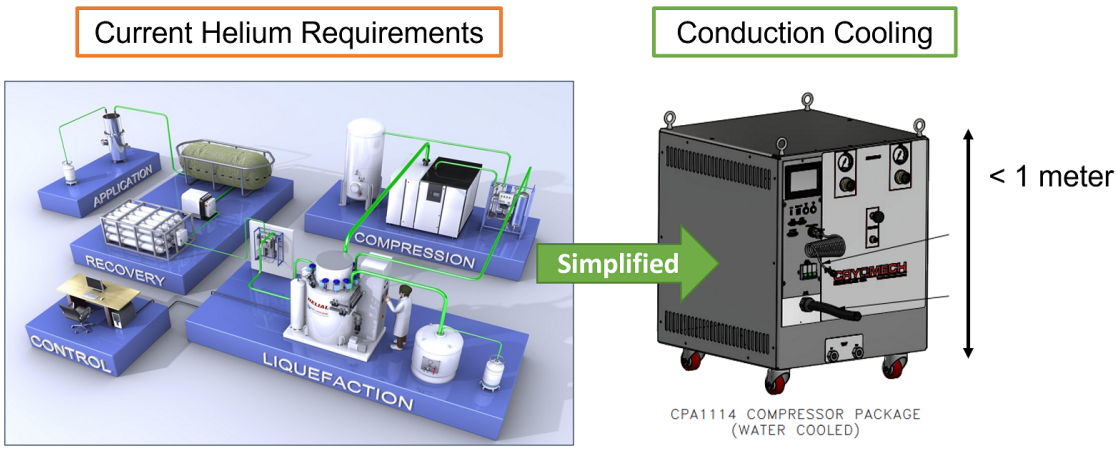

Figure 3.2: New 4 K cryocoolers (compressor unit shown on the right) have enough cooling capacity to extract the RF heat loads from Nb_3Sn cavities, such that small-scale operations would not need to install and maintain complicated liquid helium infrastructure (left).

operation; the compressor unit quite literally has a "Start" button which will begin cooling down the system without any further input. While 4 K cryocoolers often list cooldown times of about an hour [Blu24], having an assembly attached will increase this, potentially to a few hours or more. Figure 3.3 shows an example of a cooldown for a relatively small cavity assembly (discussed in depth in the following chapter). The cryocooler used in this assembly has two stages, referred to as the 1st (warmer, ~ 45 K) and 2nd (colder, ~ 4.2 K) stages. The 2nd stage took about 5 hours to reach its final temperature, while the 1st stage took closer to 10 hours.

The use of cryocoolers in place of liquid helium allows for new cooling schemes to be designed and utilized. The main two categories are direct conduction cooling of the cavity and cooling a closed tank of liquid and gaseous helium which contains the cavity. In general, the direct conduction cooling method involves physically connecting the cryocooler cold head to the cavity using some conductive pathway. This is often achieved with flexible thermal straps or a similar implementation. While the latter cooling scheme sounds oddly similar to the liquid helium cooling

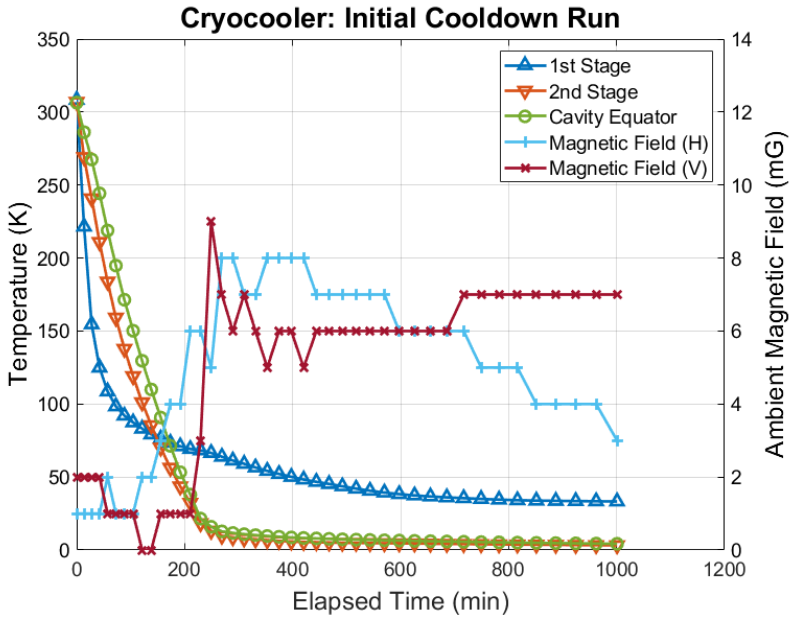

Figure 3.3: Assembly temperatures and ambient magnetic fields measured during a cavity cooldown using a cryocooler.

system that is supposed to be replaced, the main difference is that the helium tank would be fully closed. Rather than circulating the helium liquid and gas throughout a larger system, the cryocooler would re-condense the gas in-situ, creating an equilibrium state in which the liquid level remains constant. These two methods are depicted in Figure 3.4. Most of the cryocooler-based projects currently under development, including the primary work of this dissertation, utilize the direct conduction cooling method. This method simplifies the overall system, which is advantageous for small-scale industry applications that require non-expert operation and maintenance.

3.3 Materials for Conduction Cooling

Successful implementation of conduction cooling requires the use of materials which exhibit especially high thermal conductivity at cryogenic temperatures, particu-

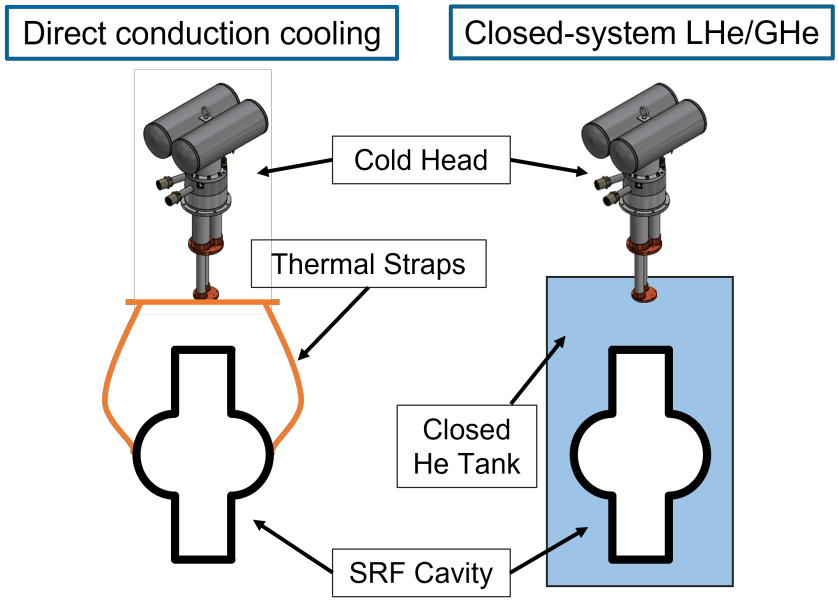

Figure 3.4: Conceptual designs of different cooling schemes made possible by the use of cryocoolers. The first option uses conduction cooling mediated by thermal straps connecting the cryocooler to the cavity, while the second uses the cryocooler to re-liquefy helium within a closed tank surrounding the cavity.

larly near 4 K. The two plots in Figure 3.5 show the temperature-dependent thermal conductivity for different materials. The plot on the left includes a wide range of materials with several orders of magnitude difference in thermal conductivity. Those near the top of the plot are of particular interest for use in conduction cooling designs, namely commercially pure coppers (ETP and OFHC) and ultra-high purity (5N) aluminum and copper. Conversely, the materials towards the bottom of the plot are typically treated as thermal insulators. In regards to niobium and Nb_3Sn, Figure 2.5 indicates that niobium would be near the middle of this plot, with thermal conductivity below 10 K similar to that of the medium-purity aluminums. Nb_3Sn, on the other hand, would be at the very bottom of the plot.

The right plot in the figure focuses on different purities of copper, providing a better illustration of the variance in thermal conductivity between different residual resistivity ratio (RRR) values. In practice, commercially produced copper is not

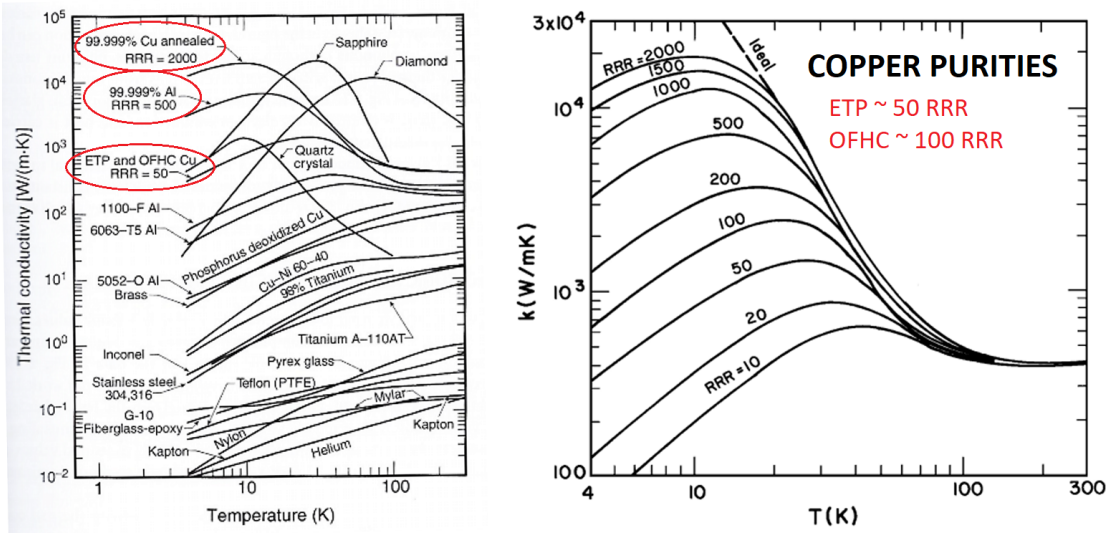

Figure 3.5: Plots of cryogenic thermal conductivity of various materials. Left: large set of materials with several orders of magnitude difference in thermal conductivity; materials of interest for conduction cooling are circled. Right: different purities of copper with more detail on the variance between a range of RRR values. The two plots first appeared in [VR08] and [PF79], respectively.

often specified by RRR value. Instead, common high-purity commercial coppers include electrolytic tough pitch (ETP) and oxygen-free high conductivity (OFHC), which typically have RRR values around 50 and 100, respectively. These coppers are also often specified by standardized UNS designations C11000 and C10100, respectively. Comparing the two plots indicates that a copper purity between 500 and 1000 RRR would be required to match the thermal conductivity of 5N aluminum; either of these options require custom ordering with a special supplier, as metals of this high purity are not typically readily available.

3.4 Ongoing Projects

Before moving on to discussing the main project that is the focus of this dissertation, it must be acknowledged that many labs around the world are conducting

similar investigations of conduction-cooled SRF cavities and cryomodules using cryocoolers. The projects discussed here are meant to be demonstrative examples of the progress in the field, and the list is not meant to be fully exhaustive. For simplicity, all cryocoolers mentioned in these projects extract ~ 2 W at 4.2 K unless stated otherwise.

Initial studies at Fermilab involved a single-cell 650 MHz Nb_3Sn cavity with Nb rings welded to both sides of the cavity equator. High-purity (5N) aluminum rings were then bolted on with a thin layer of indium in between, and bent 5N aluminum plates completed the conduction path to a single cryocooler. While the cavity was originally limited to ~ 7 MV/m, an improved Nb_3Sn coating and better-controlled cooldown resulted in stable operation at ~ 10 MV/m. More information on this study can be found in [DPG+20, DPGT22].

An ambitious extension of this initial study is a proposed design for a 10 MeV, 1 MW average power electron beam accelerator for use in wastewater treatment [D+22]. This design includes all components needed for implementing a compact accelerator system, including an electron gun for beam generation, the conduction-cooled accelerating cryomodule, and beam delivery. The proposed accelerating cryomodule would use eight cryocoolers to cool a 5-cell 650 MHz Nb_3Sn cavity. With the cavity operating around 10 MV/m, particle bunches from the electron gun could be accelerated to 10 MeV [D+22]. The 1 MW beam would then be focused and steered for use in radiating wastewater for sterilization and contaminant removal. While the design and analysis of the full system has been completed, this project has not yet advanced to full development.

Meanwhile, two conduction-cooling projects already under construction at Fermilab focus on medical device sterilization and mobile pavement treatment; both

of these systems target an average beam power of ~ 20 kW [T$^+$23]. The medical application project uses a 1.5-cell 650 MHz Nb_3Sn cavity with an integrated thermionic gun to accelerate electrons to 1.6 MeV for sterilization of medical devices. This system uses two cryocoolers as a cooling source [T$^+$23]. The pavement treatment project, in collaboration with the US Army Engineer Research and Development Center (ERDC), aims to use a 9-cell 1.3 GHz Nb_3Sn cavity to accelerate electrons to 10 MeV for radiating pavement in order to increase its durability. The accelerating cryomodule will use six cryocoolers, and while a standard cryostat has already been designed for initial testing, future implementation will require a more specialized structure suitable for mobile deployment [T$^+$23].

Jefferson Lab originally investigated a conduction-cooled assembly using a single-cell 1.5 GHz Nb_3Sn cavity which was plated with a 5 mm layer of copper on the cavity exterior. This thick copper layer was added to improve thermal conduction across the entire cavity. An additional copper ring was added to the equator region, which was then connected to a single cryocooler via copper thermal straps. This cavity reached about 6.5 MV/m; further discussion can be found in [CCPR20]. Further studies were then conducted in collaboration with General Atomics on a 950 MHz Nb_3Sn cavity which used a similar copper plating and thermal strap design. This cavity was tested in a specialized horizontal test cryostat with three cryocoolers, in which it reached about 12 MV/m [C$^+$23].

Jefferson Lab is currently developing a 3-cell 1.3 GHz Nb_3Sn cavity to demonstrate conduction cooling of a multi-cell cavity. This hydroformed cavity will receive the same copper plating treatment as in the previous projects, and will be installed and tested in the same horizontal test cryostat with three cryocoolers [Pud24]. On a larger scale, Jefferson Lab has also investigated designs for a

10 MeV, 1 MW accelerating system [V$^+$23]. This design features a 5-cell 915 MHz Nb_3Sn cavity cooled by seven cryocoolers, with an additional two cryocoolers for the high-power coupler(s). The cavity frequency was chosen to match that of commercially available magnetrons, which offer a more efficient RF power source compared to solid state amplifiers (SSAs) [V$^+$23].

Beyond the lab setting, there are other unique projects being led by industry partners. Euclid Labs is developing a conduction-cooled photoinjector for use in ultrafast electron diffraction and microscopy (UED/UEM). This system uses a 1.5-cell 1.3 GHz Nb_3Sn photogun to deliver a $\sim$ 1 MeV beam, while only requiring a single cryocooler [K$^+$24]. RadiaBeam is also developing a deployable conduction-cooled cryostat for applications such as cargo scanning. This system uses four cryocoolers to cool a 4.5-cell 650 MHz cavity delivering a 10 MeV beam with up to 1 MW average power (though the initial demonstration plans for 20 kW) [KAM$^+$23].

Researchers at KEK in Japan are investigating a 10 MeV, 500 kW conduction-cooled accelerator system for use in irradiation [S$^+$24], while researchers at IMP in China achieved an initial demonstration of accelerating an electron beam to $\approx$ 1.5 MeV with a conduction-cooled SRF cryomodule [Y$^+$24]. With still more conduction cooling-based projects being developed than what can realistically be covered here, it is clear that there is significant interest in this topic. The broad extent of industry partner involvement, even in the relatively early stages of research for this field, is a promising sign for a robust, collaborative environment as the projects continue to mature into future phases.

CHAPTER 4

PROOF-OF-PRINCIPLE DEMONSTRATION

This chapter presents an experimental cavity testing assembly which was developed in order to demonstrate the possibility of operating an SRF cavity cooled with a cryocooler in place of liquid helium. As discussed in Chapter 3, such an endeavor only became feasible quite recently thanks to improvements in both cryocooler and Nb_3Sn cavity performance, and at the time had never been directly tested. Thus it was crucial to begin by demonstrating the concept in a smaller test assembly before moving on to a full standalone cryomodule (to be discussed in Chapters 5 and 6). As such, this chapter starts with an introduction of the test assembly's operational goals, followed by the final 4.2 K thermal link design which they led to. Next, thermal simulations indicating the effectiveness of the design will be shown. This is followed by an overview of the full system assembly. After this, results from different cavity cooldowns and RF tests will be presented and discussed. In particular, the achievement of the world's first demonstration of a conduction-cooled SRF cavity operating stably at 10 MV/m thanks to the implementation of well-controlled cooldowns is highlighted. Finally, by comparing the experimental results to simulation, primary candidates for further improvements to optimize performance are determined. The discussion in this chapter will generally follow what has previously been published on this study [SHL+23b].

4.1 Operational Goals

This experiment used a 2.6 GHz elliptical (TESLA-shape [A+00]) Nb_3Sn cavity and a single Cryomech PT420-RM cryocooler as the cooling source. The cavity and cryocooler cold head were connected via thermal straps for conduction cooling,

while a high-Q_{ext} antenna was used to deliver power to the cavity. This cavity had previously been coated with Nb_3Sn using Cornell's standard coating procedure (see Chapter 2 and e.g. [Por21]), and RF testing in a 4.2 K helium bath had shown a quench field of about 17.5 MV/m with a low-field Q_0 of 8×10^9 [PLM19]. Thus, this cavity provided a convenient option for a compact cavity which was readily available and had already proven to have good performance. At the time of this experiment, the PT420 cryocooler offered the best cooling capacity at 4.2 K for a commercial cryocooler. To guide the design of the rest of the assembly, a set of operational goals for the system were determined. These goals are listed here with additional details below:

1. Reach an accelerating gradient of 10 MV/m while maintaining a cavity temperature near 4.2 K.
2. Minimize thermal gradients between the cryocooler cold head and cavity during RF operation.
3. Minimize thermal gradients across the cavity during cooldown, particularly at the superconducting transition.
4. Dampen vibrations produced by the cryocooler to minimize related cavity microphonics during RF operation.

An accelerating gradient of 10 MV/m was chosen as a convenient benchmark for cavity operation that is relevant to the applications discussed in the previous chapter. At this field level and temperature, the cavity Q_0 is expected to still be about 8×10^9 based on previous test results [PLM19]. The power dissipated in the cavity walls is estimated using the relation between dissipated power and quality factor (Equation 2.11),

$$P_{diss} = \frac{\omega U}{Q_0},$$

combined with the parameters $E_{pk}/\sqrt{U}$ and E_{pk}/E_{acc} as listed in Table 2.2. This calculation predicts a dissipated power of about 0.4 W at 10 MV/m. As this value is based on cavity performance in a helium bath, and it was not certain if the cavity would perform as well in a conduction cooled setup, a large safety factor was added and a 1 W heat load was assumed for the sake of the system design.

Minimizing the thermal gradient between the cryocooler cold head and cavity is required to keep the cavity temperature below or near 4.2 K during RF operation. The PT420-RM cryocooler has a cooling capacity of 1.8 W at 4.2 K for the 2nd stage cold head with 55 W at 45 K for the 1st stage cold head [Blu24]. A full cooling capacity range can be seen in Figure 4.1. Since the main heat load from the cavity is only taken to be 1 W, the cryocooler 2nd stage is expected to be below 4.2 K. In addition to the manufacturer's data, an early calibration test performed at Cornell showed that a 1 W heat load corresponds to a 2nd stage temperature of 3.5 K. Therefore, the thermal gradient between the cavity and cryocooler 2nd stage must be kept under 0.7 K to maintain a cavity temperature below or near 4.2 K.

Minimizing the thermal gradients across the cavity as it transitions into the superconducting state is necessary for optimal RF performance in Nb_3Sn cavities, as described in Chapter 2. A gradient of 200 mK/m or less along the cavity wall is desired to reduce the detrimental effects [Hal17]; for the 2.6 GHz cavity, this corresponds to a temperature difference of just 20 mK between the cavity irises. The vibrations produced by a cryocooler come from the various processes used to facilitate the primary heat exchange. Although pulse tube cryocoolers generally produce less vibration than GM-types, some method of dampening is still required to minimize direct transmission of such vibrations to the cavity. One initial step

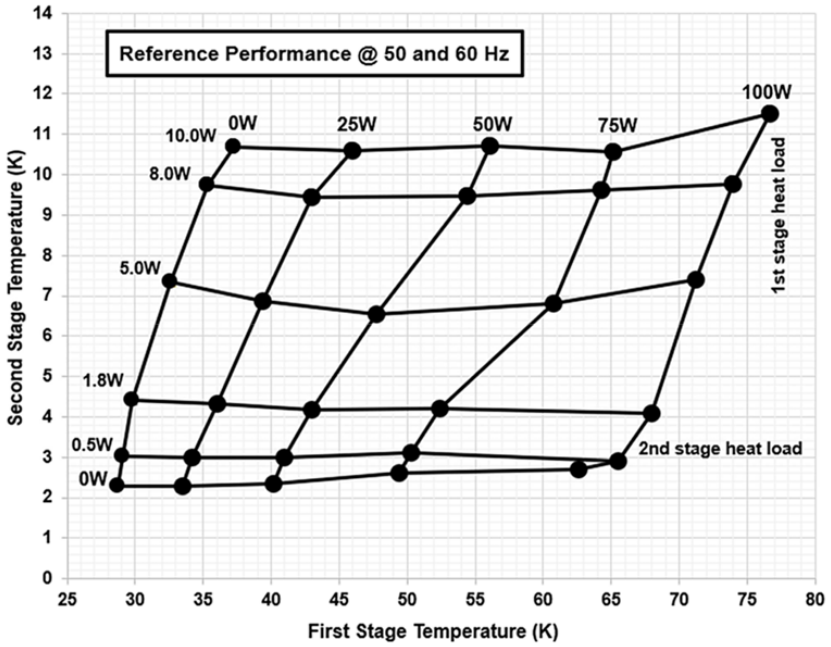

Figure 4.1: Cooling capacity of the PT420-RM cryocooler with CPA1114 compressor [Blu24].

towards this goal was the use of a cryocooler model (-RM) in which the primary exchange motor (main source of mechanical vibrations) is isolated from the rest of the cold head assembly.

4.2 Thermal Link Design and Simulation

The main challenge in designing such a system was achieving a sufficient thermal connection between the cryocooler 2nd stage cold head and the cavity, such that the operational goals could be met. Compared to cooling a cavity with liquid helium, in which the cavity experiences uniform cooling from the surrounding bath, in the new system the cavity heat load must be transported to the cryocooler through a dedicated thermal pathway. Finding a successful design involved an iterative process of creating a 3D model in Autodesk Inventor [Aut23] and then analyzing

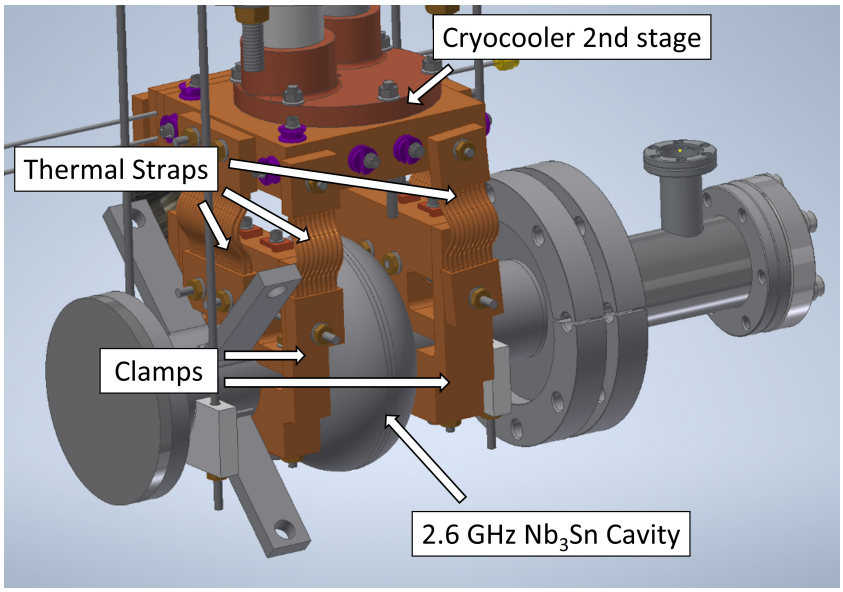

Figure 4.2: 3D model of the final thermal link design. Highlighted in the figure are the 2.6 GHz Nb_3Sn cavity, beam tube clamps, thermal straps and cryocooler 2nd stage cold head. Also visible is the extension piece for the forward power antenna to the right.

its thermal behavior via simulations in Ansys Mechanical [Ans23]. The results of said simulations could then be used to determine possible improvements for the next model iteration. The final design produced by this process, along with its thermal simulation results, is presented and discussed here.

The primary features of the thermal link between the cavity and cryocooler 2nd stage cold head are (a) beam tube clamps attached at the cavity irises and (b) braided thermal straps connecting the clamps to the cryocooler. Both of these components are made out of OFHC copper[1], with the clamps machined in-house and the thermal straps being purchased from a specialized manufacturer, Technology Applications, Inc (TAI) [TAI23]. These main features, along with the cavity and cryocooler 2nd stage cold head, are shown in a 3D model in Figure 4.2.

The clamp design was chosen for a couple reasons. First, since the cavity was

[1]Refer to Chapter 3 for discussion of materials for conduction cooling.

already fabricated, it was impractical to add any sort of permanent connection via welding. The beam tube clamps offered an effective way to attach to the cavity without significant alterations to the cavity itself. In addition, having clamps at the irises can offer better control of thermal gradients across the cavity during cooldown, as will be explored further in the next sections. The braided thermal straps were used to provide the necessary flexibility in the assembly to avoid excessive stress due to differential thermal contraction, while maintaining high thermal conductivity for heat transport thanks to the use of high-purity copper. While it's possible to make rudimentary thermal straps in-house, manufacturers such as TAI have optimized processes to ensure better contact between the mounting ends of the straps and the braids themselves, which can otherwise be a point of poor thermal contact [TAI23]. The flexible braided straps also offer some dampening of vibrations which would otherwise reach the cavity with little resistance.

Setting up reliable thermal simulations of the assembly requires accurate thermal conductivity values for the various materials used. For the OFHC copper components machined in-house, resistivity measurements on a sample piece indicated a residual resistivity ratio (RRR) of 150. Thus, thermal conductivity values for RRR 150 copper from NIST were used [BR13]. Thermal conductance (W/K) values for the different thermal straps were provided by TAI, which were then converted to an effective thermal conductivity. Lastly, the temperature-dependent thermal conductivity of RRR 300 Nb (see Figure 2.5) was assigned to the cavity, as the thermal transport in the cavity walls will be dominated by the bulk Nb rather than the much thinner Nb_3Sn film.

The main thermal boundary conditions used in the simulation are the 1 W heat load in the cavity cell and a fixed temperature of 3.5 K at the cryocooler cold

head. A fixed temperature (based on the cryocooler cooling capacity) was chosen to simplify the calculations. No radiative heat load is added since the cavity would be wrapped in superinsulation, resulting in a very small contribution compared to the cavity heat load. The low-power coupler is effectively thermally isolated and is thus excluded from the thermal model.

The results of these simulations[2] are shown in Figure 4.3. There are a few main points to highlight. First, the cavity temperature is about 4.47 K, corresponding to a thermal gradient of about 0.97 K between the cavity and cryocooler cold head. Although this is higher than the initial target, considering the large safety factor used for the cavity heat load, it was decided that this result was acceptable to move forward. The second point is that the top and bottom sides of the equator are nearly identical in temperature. This offers a clear confirmation that even without a direct thermal connection to the equator, there would still be even cooling around the whole cavity. In addition, the temperatures at the two beam clamps (on opposite sides of the cavity cell) are very similar, indicating that there is not an inherent risk of one side of the cavity warming up much more than the other during RF operation. Overall, these points confirm that this thermal link design is sufficient for the purposes of the proof-of-principle demonstration.

It is also worth noting a couple points of potential improvement for future designs, especially for larger systems. As mentioned previously, implementing an effective thermal connection directly to the cavity equator was particularly challenging for an already fabricated cavity. As shown in the thermal results, the relatively low thermal conductivity of niobium near 4 K ($< 100\,\mathrm{W/(K * m)}$) causes

[2]Publishing a journal article about this experiment required the inclusion of details about the simulation meshing itself. While the author believes most readers would consider this superfluous, here are some metrics in honor of Reviewer 2: this simulation used about 400,000 total elements, of which approximately 350,000 were tetrahedral and 50,000 were hexagonal. The more you know!

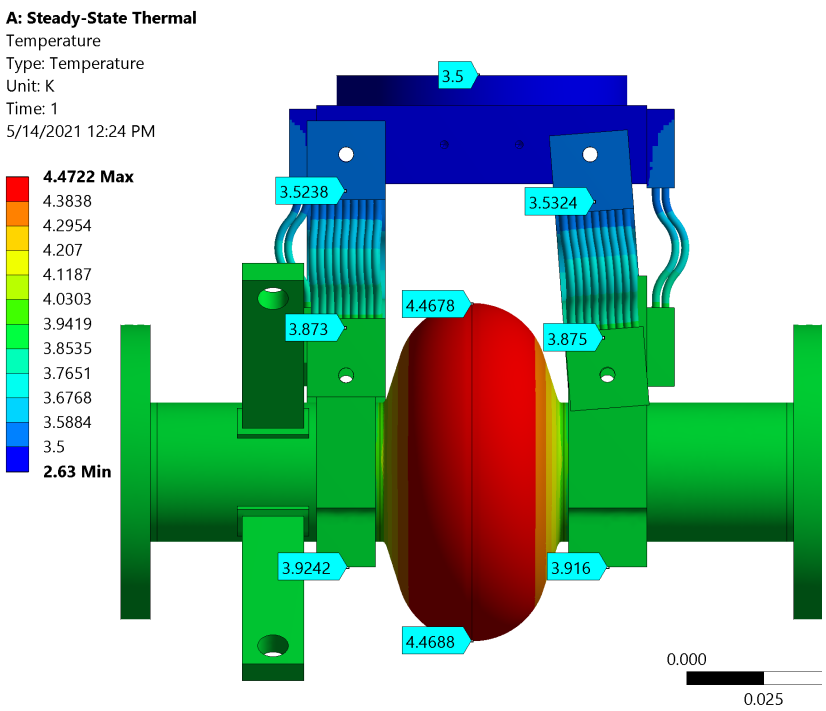

Figure 4.3: Numerical results from a thermal simulation of the final assembly design performed in Ansys. The cavity is shown to be at 4.47 K, slightly higher than the target of 4.2 K or below. However, given the large safety factor used for the applied heat load, this result was deemed to be satisfactory. The results also show equal cooling to both sides of the cavity.

the cavity cell to be noticeably warmer (about 0.5 K) than the copper clamps. This difference is acceptable due to the relatively small cavity heat load in this experiment, however it could quickly become an issue for larger and/or multi-cell cavities. When designing a new cavity for use in a larger system, having a direct thermal link to the equator region would be advantageous. Another potential improvement could come from the thermal straps. The simulation results show that for the total thermal gradient between the cryocooler cold head and the copper clamps, about 80-90% comes from the braided copper. This suggests that other options like straps made of metal foils, with a lower effective path length, may be better suited for larger systems with higher heat loads.

4.3 Full System Assembly

This cavity assembly was designed for use in one of the existing test pit dewars in Newman Lab, thus it was not necessary to design a new outermost vacuum structure. In addition, due to the large cooling capacity of the cryocooler 1st stage and the experiment being limited to low-power testing, the thermal performance of the remaining assembly did not pose as significant of a challenge. The main design considerations were the same as those for any sufficiently cold system, namely balancing the need to structurally support the cavity with the need to reduce static heat leak from room temperature (via both conduction and radiation). Since these components were not a particular focus of this study, this section will simply present the final full system design along with some images of putting the assembly together.

Figure 4.4 shows a model of the final design for the full system. The cavity and cryocooler 2nd stage cold head, along with the thermal link discussed in the previous section, can be seen near the bottom. Because the cold heads themselves cannot support much weight, the cavity is held by aluminum cradles hung from support bars above. These support bars are cooled to about 45 K by the cryocooler 1st stage cold head; the use of thin steel rods for supporting the cradles helps thermally isolate the cavity from the warmer temperature. To protect the cavity from room temperature thermal radiation, a copper thermal shield (also cooled to $\sim 45\,\mathrm{K}$) is placed around it. Lining the thermal shield is a Mumetal magnetic shield to protect the cavity from Earth's magnetic field. The entire assembly is suspended from a steel top plate, such that it can be lowered into one of the RF test pits at Newman Lab.

Different stages of the assembly process for the full system can be seen in Figure

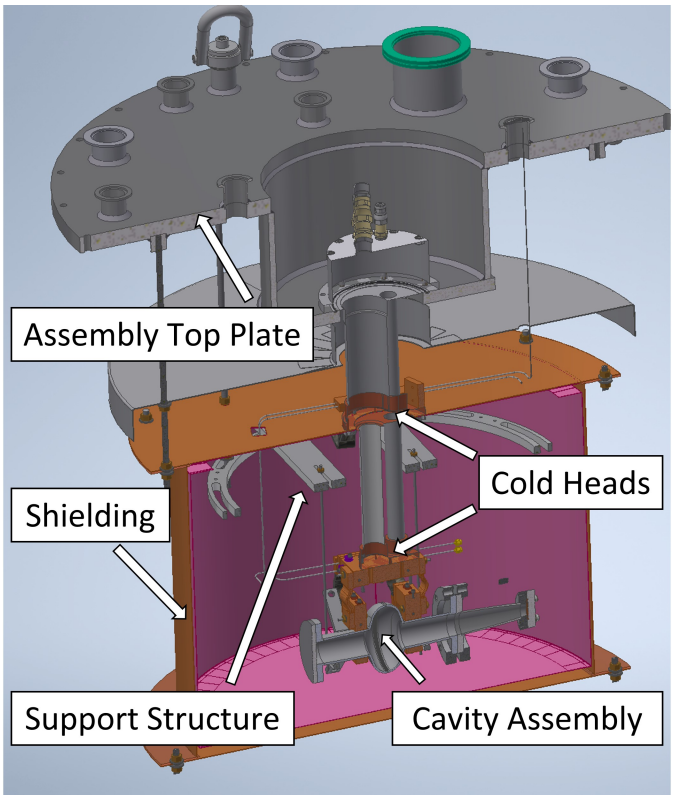

Figure 4.4: 3D model of the full experimental system for the proof-of-principle demonstration. More details of the cavity assembly, shown at the bottom, are visible in Figure 4.2.

4.5. Figure 4.5a shows the cavity assembly with all sensors and instrumentation attached. Cernox temperature sensors are attached to the cavity equator, both copper clamps, the cryocooler 2nd stage cold head, and the forward power coupler. The sensors on the clamps and cold head are in a special bobbin-like encasing (CD package), which helps improve thermal anchoring of the sensor and reduces the risk of self-heating. The remaining sensors are the standard type (SD package) [Cry23]. All of the Cernox sensor wiring is anchored to the 2nd stage cold head via copper bobbins as well. While possibly redundant for the CD-type sensors, this is necessary for the SD-types to eliminate self-heating (and thus incorrect readings). Two flux gate sensors were suspended near the cavity equator in the vertical and horizontal directions, with the horizontal sensor being parallel to the

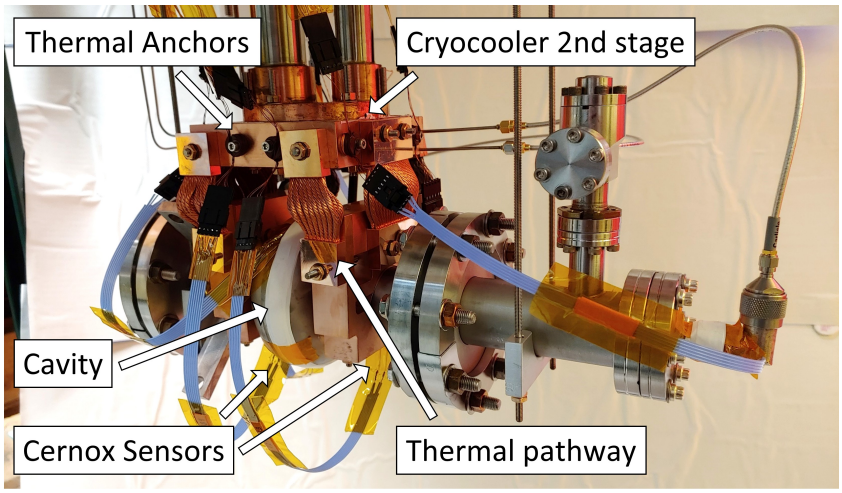

(a)

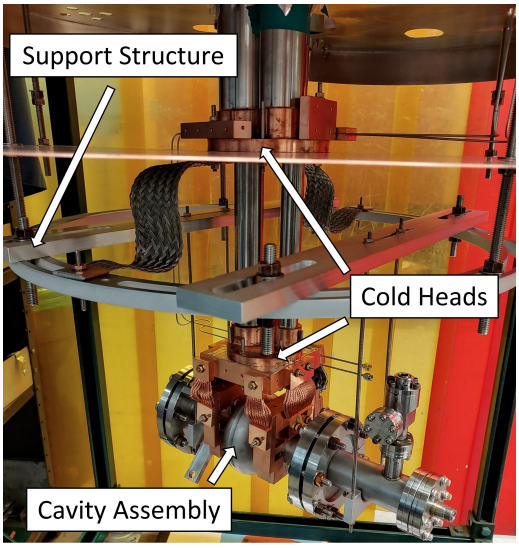

(b)

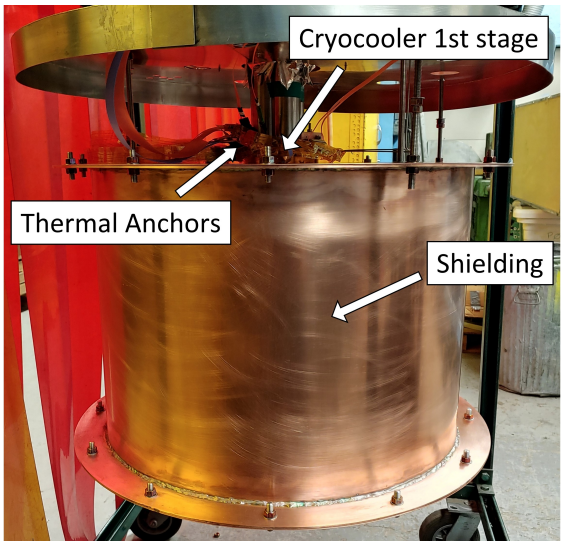

(c)

Figure 4.5: Various stages of assembly for the full system: (a) cavity assembly with sensors; (b) full assembly (no sensors) before shielding is added; (c) after shielding has been attached.

cavity's longitudinal axis.

The full assembly (without sensors or instrumentation) can be seen in Figure 4.5b, prior to attaching the thermal and magnetic shielding. Visible in the center of the image is the support structure used to suspend the cavity assembly, as well as thermal straps connecting it to the cryocooler 1st stage cold head. In addition,

copper blocks are attached to the 1st stage cold head, which are used to thermally anchor both the RF semi-rigid cables and various sensor cables. These anchored cables can be seen in Figure 4.5c, along with the attached shielding.

To improve thermal contact between critical surfaces, such as those at the 1st stage cold head and between the 2nd stage cold head and cavity, a small amount of Apiezon N cryogenic grease is used to help fill in small scratches or other microscopic features. Though the grease does not have particularly good thermal conductivity, it is still an improvement over having small, empty gaps between the surfaces [Api24]. Thinly rolled indium was placed between the 2nd stage cold head and mounting block as well as wrapped around the cavity beam tubes where the copper clamps were attached. This was used in place of Apiezon N grease to ensure maximum thermal contact in these critical regions where there otherwise may be larger gaps than what the grease is effective for. Lastly, heat loads from thermal radiation were reduced at both the 1st and 2nd stage assemblies by using multi-layer insulation (MLI) comprised of alternating layers of aluminized mylar and fiberglass. Ten layers were wrapped around the cavity assembly while 30 layers were wrapped around the thermal shield.

4.4 RF Testing Results & Discussion

A comparison of the quality factor vs accelerating gradient from several RF tests is shown in Figure 4.6. Following the initial cooldown, as shown in Figure 4.7, the cavity performance was notably worse than the previous baseline test in liquid helium. The cavity only reached an accelerating field just under 8 MV/m with a low-field Q_0 of just under 2×10^9. During this cooldown, the thermal gradient

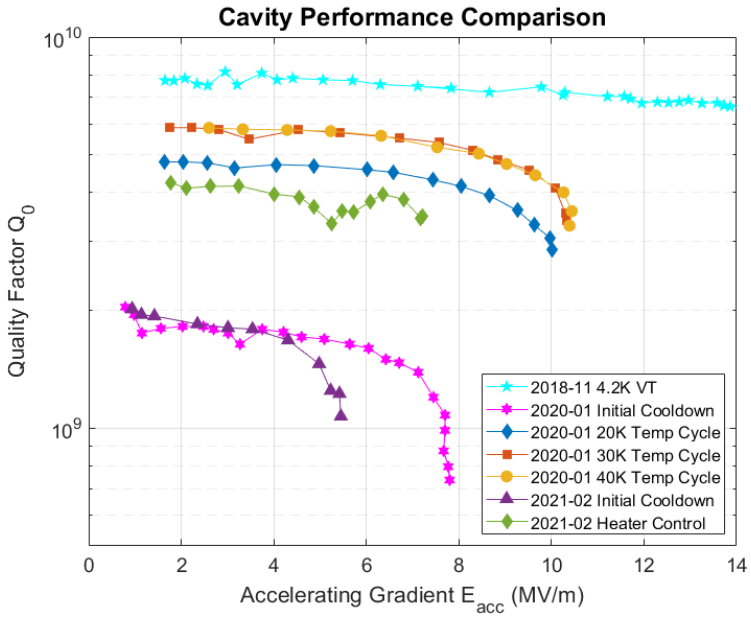

Figure 4.6: Comparison of quality factor vs accelerating gradient for the 2.6 GHz Nb_3Sn cavity from seven different tests. These tests include a baseline helium bath test (VT) and various conduction cooled tests following initial system cooldowns or temperature cycles.

across the cavity near T_c was on the order of a few hundred mK, much higher than the target 10 mK for a 2.6 GHz Nb_3Sn cavity. To remedy this, the use of temperature cycling just above T_c was explored as a way to reduce these thermal gradients. In this set of tests, the cavity was re-cooled from 20 K, 30 K and 40 K. This resulted in a significant improvement: after all three cycles, the cavity achieved stable RF operation just above 10 MV/m. After the 20 K temperature cycle, the low-field Q_0 was 5×10^9, while both the 30 K and 40 K cycles resulted in a low-field Q_0 of 6×10^9. Magnetic fields just under 10 mG were measured at the cavity before the initial cooldown for this set of tests. These results represent the world's first-ever demonstration of a conduction-cooled SRF cavity operating stably at 10 MV/m. This accelerating gradient is at a level relevant to the intended small-scale applications introduced in Chapter 3, making this result a significant milestone in the development of compact SRF systems.

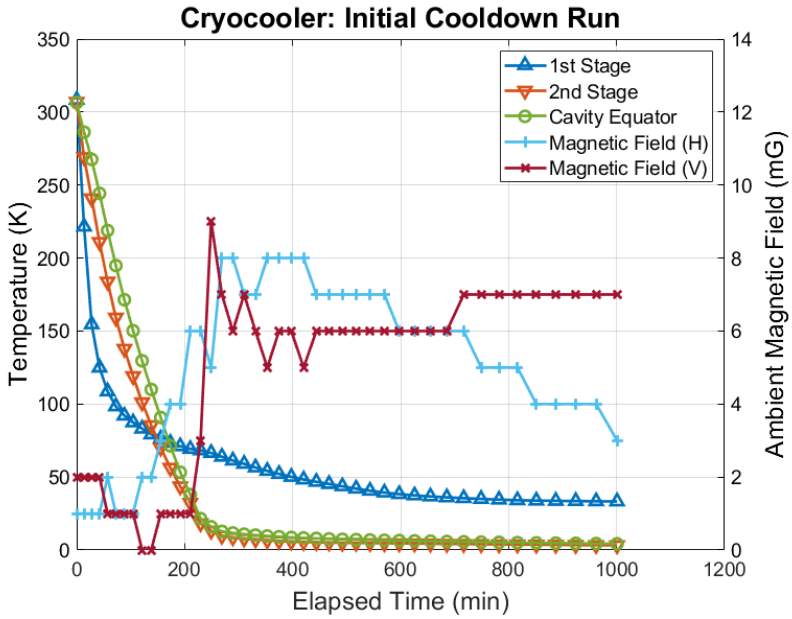

Figure 4.7: Assembly temperatures and ambient magnetic fields measured during an initial (uncontrolled) cooldown of the conduction-cooled 2.6 GHz cavity assembly. This Figure is duplicated from Figure 3.3 for convenience.

To explore the possibility of fine-tuned control over spacial thermal gradients, a pair of 1 kΩ resistors were added to the beam tube clamps to act as heaters. These heaters were independently controlled by two power supplies which were manually adjusted during cooldown. Another set of initial cooldown and temperature cycling tests were performed; in this version, the heaters were used to warm the cavity to about 19 K while simultaneously balancing the temperatures of the two beam tube clamps. Following the initial uncontrolled cooldown, the cavity only reached about 5.5 MV/m with a low-field Q_0 of 2×10^9. The heater-controlled temperature cycle produced a notable improvement in performance, in which the cavity reached just above 7 MV/m with a low-field Q_0 of 4×10^9. The magnetic fields at the cavity were measured to be less than 5 mG before the initial cooldown. Further analysis of these cooldown and test results will be discussed in the remainder of this section.

4.4.1 Effects of Controlled Cooldown

To further examine the effect that thermal gradients across the cavity during cooldown have on RF performance, the low-field surface resistance R_s and thermal gradient were compared for each of the conduction-cooled tests. Low-field values are used to minimize the contribution from the BCS resistance (R_{BCS}), which is strongly temperature-dependent. Experimental data shows that a 2.6 GHz Nb_3Sn cavity has an R_{BCS} of 4 nΩ and 2.5 nΩ at 3 K and 2.5 K, respectively [PLM19]; these correspond to cavity temperatures measured at low fields in these tests.

Figure 4.8 shows the dependence of the low-field R_s on the thermal gradients at T_c. The occurrence of a significant change in the ambient magnetic field measured at the cavity was used as the most reliable indicator of the cavity transitioning to the superconducting state (see e.g. Figure 4.7). This measured change typically lasts on the order of a minute, leading to some uncertainty in the time of transition and thus the true value of the thermal gradient; this is represented by the horizontal error bars in the figure. A clear reduction in the surface resistance is present when the thermal gradients across the cavity at T_c are minimized (within each set of tests), which can be achieved through the use of well-controlled cooldown procedures. Even within the different temperature cycles in the first set of tests, the 20 K cycle had a slightly higher thermal gradient and thus worse performance than the 30 or 40 K cycles.

There are a couple points to consider regarding the results from the heater control test. First, the heater-controlled temperature cycle was the only method able to reliably achieve the target thermal gradient of 200 mK/m or less. Although a basic temperature cycle is slightly simpler, the amount of time required to hold the assembly above T_c is then purely determined by how long it takes the assembly

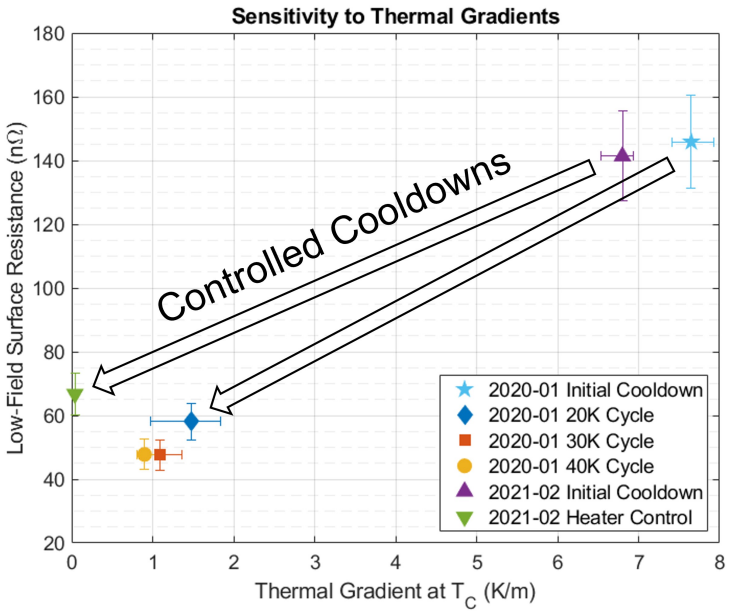

Figure 4.8: Low-field surface resistance R_s vs thermal gradient across the cavity during the superconducting transition. The thermal gradient was determined using the temperatures measured at the cavity irises. Within each set of tests, controlled cooldowns with smaller thermal gradients result in a significantly reduced surface resistance.

to naturally equilibrate. The use of heaters is able to greatly speed up this process even with very simple control methods. This is illustrated in Figure 4.9, which shows that the small gradient achieved using the heaters is also the most stable during the cooldown process.

Second, even though the measured thermal gradient is smallest in the heater control test, the RF performance is worse than that of the other temperature cycles. This suggests there may also be differences in thermal gradients around the equator (azimuthal), which were not measured in these tests. It is possible that while the iris-to-iris thermal gradient was minimized in the heater control test, the azimuthal gradient increased and contributed to the worsened cavity performance. To address this issue in future studies, additional temperature sensors and heaters will be used to properly measure and reduce any azimuthal gradients present during cooldown.

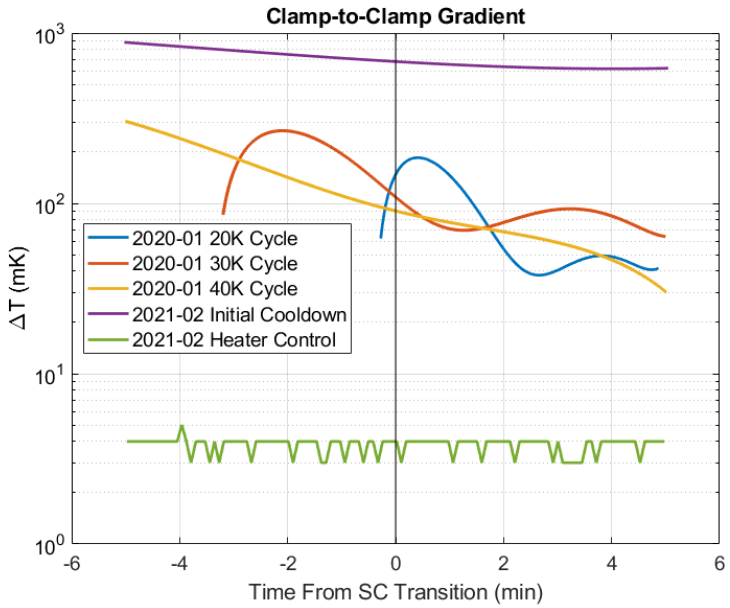

Figure 4.9: Thermal gradient between the two beam tube clamps (outside cavity irises) during cavity cooldown. Controlled cooldowns via basic temperature cycle or heater control over order(s) of magnitude improvement compared to initial uncontrolled cooldowns from room temperature.

Other possible factors unrelated to the cooldowns could include an increased static heat load in the later tests, or a degradation of the cavity surface or vacuum due to the cavity remaining sealed for long periods between tests (i.e. not re-cleaned and assembled for each set).

4.4.2 Cavity Assembly Temperatures

Due to the absence of a helium bath, the warming of the cavity with increasing field strength is easily measured. Figure 4.10 shows the temperatures of the cavity assembly during RF operation in both the 30 K temperature cycle test and the heater control test. In the former, the whole cavity assembly remained under 2.5 K while under stable CW operation up to about 4 MV/m. At the highest field of 10.3 MV/m, the cavity reached 4.2 K while the 2nd stage cold head remained

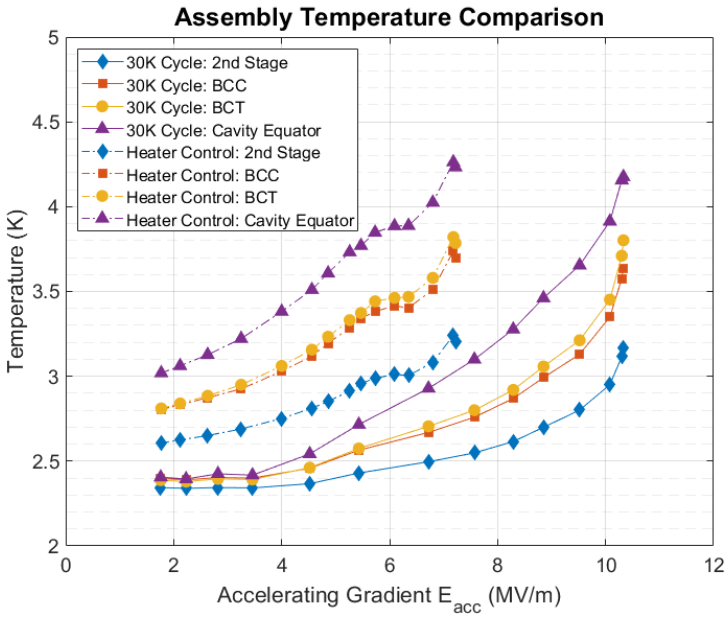

Figure 4.10: Cavity assembly temperatures during RF operation following the 30 K temperature cycle test and the most recent heater control test. The temperatures shown are from the cryocooler 2nd stage cold head, both copper beam tube clamps, and cavity equator.

at 3.2 K. This achieves one of the main goals of the experiment: obtaining stable operation at 10 MV/m with a cavity temperature near 4.2 K. The copper clamp temperatures (labeled BCC and BCT) were between those of the cavity and 2nd stage cold head, as one would expect.

In comparison, the assembly temperatures in the heater control test start noticeably higher, with the cavity equator measuring above 3 K at an accelerating gradient of just 2 MV/m. It is clear that the field dependence of the temperature is significantly higher as well. However, the final assembly temperatures are the same as those in the 30 K temperature cycle test, although the maximum accelerating gradient is lower. This indicates that these final temperatures correspond to the warmest stable state before thermal runaway occurs.

4.4.3 Static Heat Loads

The markedly different low-field cold head temperatures seen in Figure 4.10 indicate a non-negligible change in static heat load reaching the cavity assembly. As discussed previously, these heat loads are caused by static heat leak from room temperature reaching the cavity via conduction or thermal radiation. One way to measure this change is to compare the temperatures of the cryocooler cold heads prior to RF operation with the cooling capacity curves provided by the manufacturer. Figure 4.11 shows such a comparison. The RF-off temperatures from the basic temperature cycle tests are marked with a green dashed line while those from the heater control tests are shown with an orange "X". A dashed line is used for the basic temperature cycle tests because it was learned later on that the SD-type Cernox temperature sensor on the 1st stage cold head had unreliable thermal contact (it was later replaced with a more secure CD-type sensor). Thus the temperature of the 1st stage is not certain for this test, so the measured 2nd stage temperature only defines a horizontal line on the plot. However, based on where the dashed line intercepts the 0 W curve for the 2nd stage, an upper limit of about 42 K can be placed on the 1st stage. By comparison, the heater control tests had reliable temperature measurements for both stages, so an exact point on the plot can be marked.

Based on the temperature of the 2nd stage, the cavity assembly was very well isolated from static heat loads in the basic temperature cycle tests. However, the heater control tests show an increased static heat load of about 0.25 W. This increased static heat load compromises how well the cavity is able to perform during RF operation, as the ability of the cryocooler to extract the cavity heat load is reduced. While it is difficult to determine the exact source of the increase in static

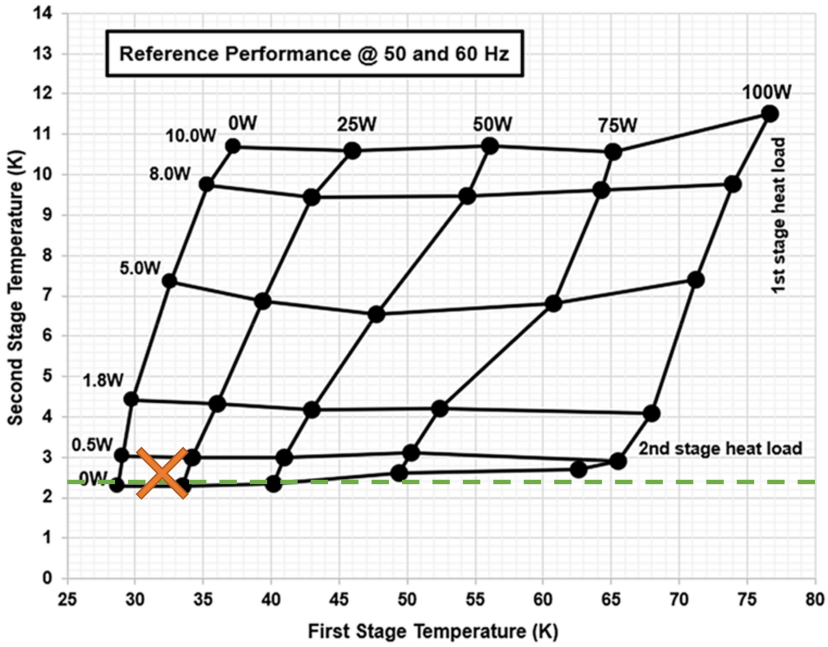

Figure 4.11: Cooling capacity of a PT420-RM cryocooler relating the heat loads and temperatures of both stages [Blu24]. Markers indicate the temperatures measured with RF off for both sets of tests (basic temperature cycle in green, heater control in orange).

heat load, one contribution may come from the RF cables which were replaced during the two sets of tests. A new forward power cable was used for the heater control tests which had less RF attenuation but higher thermal conductivity than the cable used in the basic temperature cycle tests. Another potential contribution could be worse thermal anchoring of instrumentation at the cryocooler 1st stage, causing more heat to reach the 2nd stage.

4.5 Comparison to Simulation

With the data collected from the RF tests, comparisons can be made between various experimental results and simulations performed in Ansys Mechanical [Ans23] (such as those discussed previously). Making these comparisons can offer insight

into new improvements to consider for future studies as well as determining whether the thermal simulations offered accurate predictions. This helps indicate how well such simulations can be relied on for future projects, or whether changes need to be made in how they are set up.

Figure 4.12 shows a comparison between the experimentally measured temperatures and numerical results calculated in Ansys. Figure 4.12a corresponds to 10 MV/m from the 30 K temperature cycle while Figure 4.12b corresponds to 7 MV/m from the heater control test. For each simulation, a heat load was applied to the cavity while the 2nd stage cold head temperature was fixed. The experimental values for these boundary conditions are 0.78 W and 2.95 K for the former and 0.38 W and 3.08 K for the latter. As before, these heat loads are calculated using the corresponding field levels and cavity quality factors.

In the first comparison (Figure 4.12a), there is good agreement overall between the simulated and experimental temperatures. This indicates that in most cases, there was sufficient thermal contact across the cavity assembly to be well-described by the model parameters described earlier. However, the figure also shows a slightly higher experimental temperature on one of the beam tube clamps (left side in the figure), which could indicate that the thermal contact on one end (or both ends) of the thermal straps on that side is slightly degraded. This highlights a possible improvement of ensuring uniform thermal contact between the two sides of the assembly through e.g. application of identical torques at the mounting points.

The second comparison (Figure 4.12b) shows that both the cavity and beam tube clamps have notably higher temperatures in experiment than what is found in the simulation. One contribution to the increased thermal gradients will come from a larger static heat load, as discussed in the previous section. However, the

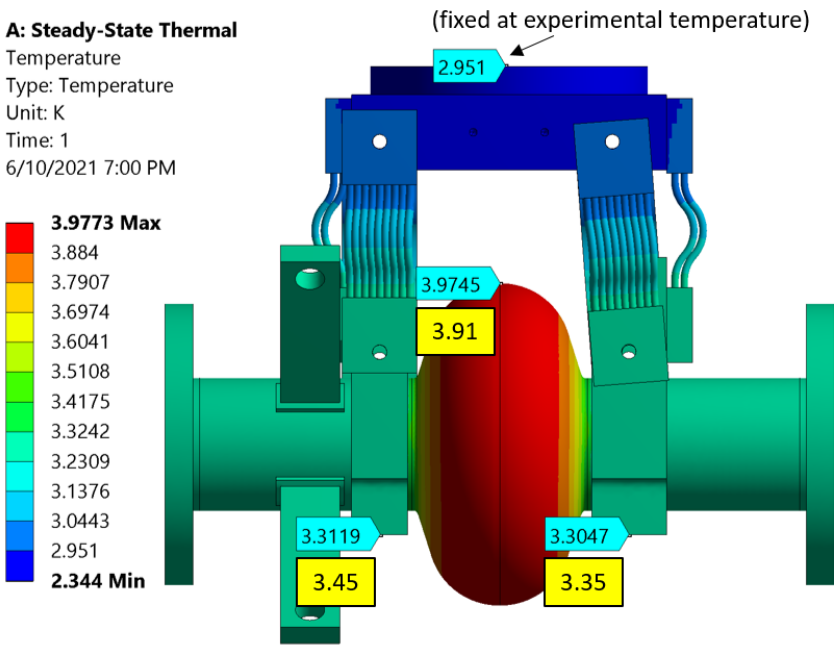

(a)

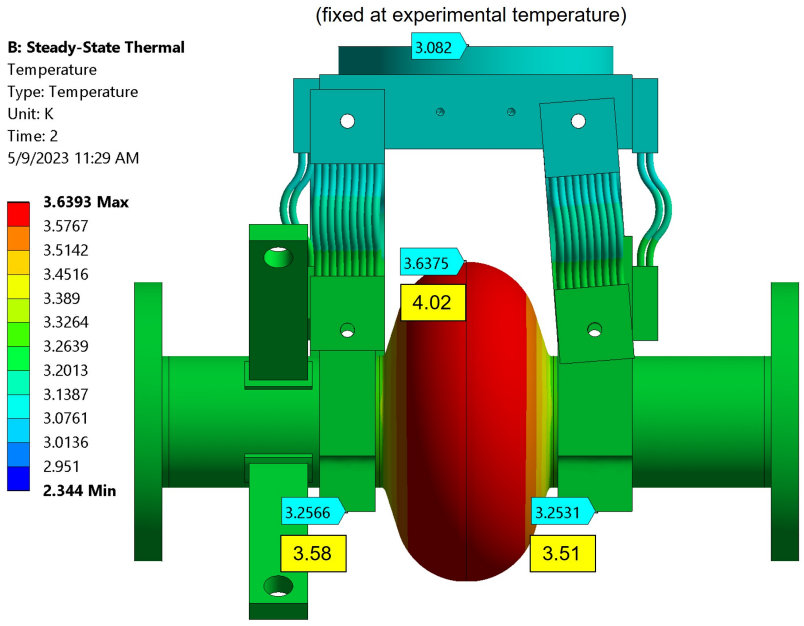

(b)

Figure 4.12: Comparison of experimental temperatures measured via Cernox (yellow/lower) to numerical simulation results (teal/upper). (a) 10 MV/m from the 30 K temperature cycle; (b) 7 MV/m from the heater control test.

majority of this temperature difference comes from the beam tube clamp temperatures. The temperature gradient between the beam tube clamps and cavity equator

is only 0.06 K higher in the experimental values, while the gradient between the cryocooler 2nd stage and the beam tube clamps is 0.25 K higher, a factor of two increase from the numerical results. This suggests that the thermal contact issue in this case is focused on the mounting points of the thermal straps to the beam tube clamps and/or cryocooler 2nd stage. This would match the implementation of set torques for attaching the thermal straps in this test, which were lower than what was used in the earlier tests. The torques were lowered in order to avoid crushing and permanently deforming the Inconel Belleville washers being used, as this had occurred previously and had lead to strong magnetization of the washers. This indicates that future studies should take into account the reduced thermal conductance at such contact points depending on what torques are possible.

4.5.1 Cavity Thermal Conductivity

Another comparison between the numerical simulations and experimental results (as well as theoretical predictions) can be made by calculating the cavity's thermal conductivity. This can be used to both check for reasonable thermal behavior and to find an estimated RRR value for the cavity's niobium walls, as it is assumed that the niobium dominates the thermal transport behavior compared to the Nb_3Sn film. This is useful to determine since the RRR value of the bulk niobium substrate following the Nb_3Sn coating process is not well known. Part of the coating process heats the cavity to about 1150 °C which occurs in a reaction chamber with unknown levels of residual gasses. It is possible that impurities such as nitrogen or oxygen could diffuse into the cavity, reducing the RRR.

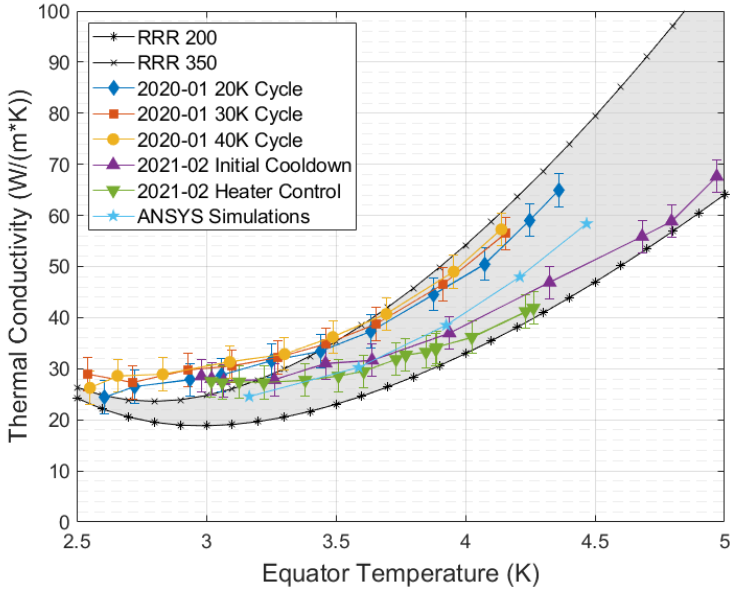

Figure 4.13: Niobium thermal conductivity curves extracted from both experimental data and Ansys simulations. The shaded region represents the range of values between theoretical curves for RRR 200 and 350 niobium.

Thermal conductivity k can be calculated as follows:

$$k(T) = (P_{\text{diss}}(T) + P_{\text{static}})/((A/L)_{\text{eff}} * \Delta T_{\text{av}}(T)). \tag{4.1}$$

ΔT_{av} is the thermal gradient between the cavity equator and beam tube clamps, averaged between the two sides of the cavity. Generally, A is the cross-sectional area and L is the length of the object through which heat is transferred. In this case, $(A/L)_{\text{eff}}$ is an effective geometric constant with units [m] which plays the same role and was calculated for a 2.6 GHz half-cell in Ansys. The calculation of $(A/L)_{\text{eff}}$ takes into account the dissipated power distribution in the cavity.

Figure 4.13 shows the results of these calculations. Above 3.5 K, the experimental data falls between theoretical curves for niobium with RRR 200 and 350 with slight discrepancy at lower temperatures. This indicates that the bulk niobium substrate of the cavity maintained a high RRR even through the Nb_3Sn coating process. The plot also includes calculated values based on the results of the ther-

mal simulations, which fall within the same range as the experimental results. This confirms that using the thermal conductivity of 300 RRR niobium in the original thermal model was an accurate choice.

4.6 Summary

This chapter explored the design and testing of a proof-of-principle experiment meant to demonstrate the possibility of operating an SRF cavity with a cryocooler in place of liquid helium. A 2.6 GHz Nb_3Sn cavity was used, with copper clamps at the cavity irises making up the primary thermal connection between the cryocooler 2nd stage cold head and the cavity. This cavity underwent several rounds of RF testing with various changes and improvements made to the assembly in between. In the best RF tests, the cavity reached 10 MV/m while remaining under 4.2 K, achieving the primary objective of this experiment. This was the world's first demonstration of a conduction-cooled SRF cavity operating stably at accelerating gradients relevant to the small-scale applications this research is motivated by. In addition, comparison of different cavity cooldowns and corresponding RF performance clearly revealed the importance of using controlled cooldowns to minimize thermal gradients across the cavity near T_c in order to achieve improved performance. Different methods of controlled cooldowns were tested, including basic temperature cycling and heater control, demonstrating the effectiveness of these methods.

Beyond the cavity performance, this study also provided several points of interest regarding possible design and assembly improvements for future projects. Initial design work indicated that a choice of better (though likely more expen-

sive) thermal straps, such as foils rather than braids, could offer a significant improvement to the thermal behavior of the cavity assembly. Comparing static heat loads from different cooldowns highlighted the importance of considering how any changes made to the system can affect such static loads, which in turn influence the maximum achievable cavity performance. Finally, comparisons between experimental data and numerical simulations further emphasized the importance of using consistent, verified methods for assembling critical thermal connections in order to obtain results as predicted. Many of these considerations were used as guidelines for the design of a new conduction-cooled SRF cryomodule, as presented in the following chapter.

CHAPTER 5

DESIGN OF A NEW CONDUCTION-COOLED CRYOMODULE

Following the successful proof-of-principle demonstration described in the previous chapter, a new project was proposed: extending the conduction cooling method to a full standalone SRF cryomodule. In addition to the cavity, the entire system would be cooled only using cryocoolers with no liquid cryogenics involved. This required designing a new system from the ground up, with particular focus on the accelerating cavity and forward power coupler. Various aspects of the thermal design were guided by the lessons learned from the previous experiments with the 2.6 GHz cavity. The first section of this chapter will outline the primary goals and challenges that drove the design of this new system. The following two sections will focus on the cavity and coupler, discussing these key components in greater detail. The remaining section will cover a variety of topics, including the vacuum vessel, thermal shield, support structure and other auxiliary components.

5.1 Goals and Challenges

As described in Chapter 3, the applications that motivate the design of such a system require medium energies ($\sim$ 1-10 MeV) and high powers ($\sim$ 0.1-1 MW). The operating goals of the new system fall on the lower end of this range, with an intended energy gain of 1 MeV and maximum power of 100 kW – see Table 5.1. These specifications provide a more realistic benchmark for an initial design while allowing for possible improvements in future phases. Even so, achieving successful operation at this level while relying solely on conduction cooling poses significant challenges.

Property	Value	Units
Frequency	1.3	GHz
Energy Gain*	1	MeV
Max Current	100	mA
Max Power	100	kW

* For relativistic beam.

Table 5.1: Cryomodule Operating Specifications

The first major challenge is achieving effective cooling of the cavity assembly without the use of liquid helium. The difficulty arises from the limited cooling capacity of the cryocooler(s). During the early stages of the system design (when the cryocoolers were purchased), the most powerful 4 K cryocoolers could remove up to 2.5 W heat at the 2nd stage cold plate. For the new cryomodule, a new PT425-RM cryocooler was purchased, which provides 2.35 W of cooling at 4.2 K [Blu24]. Together with the PT420-RM reused from the proof-of-principle demonstration, the new system has a total heat load limit of 4.15 W at 4.2 K. While the cryocooler cold heads themselves can run warmer without issue if there is a higher heat load, designing the cavity to run warmer can increase the risk of thermal runaway occurring at a lower field than desired. For example, Figure 4.10 shows that the maximum stable temperature for the 2.6 GHz Nb_3Sn cavity in the proof-of-principle demonstration was about 4.2 K. Considering the possibilities that the cavity performance ends up worse than expected or other contributions to the total system heat load end up larger, it is safest to design the system with 4.2 K operation in mind.

The second primary challenge is to design a high-power coupler capable of operating in the conduction cooling system. The coupler is used to bring high-power electromagnetic waves from a waveguide to the cavity with relatively low RF losses. This often involves transforming the waves into a mode that is transmitted

to the cavity more easily, such as a coaxial mode. In the case of the new system, the power coupler was originally required[1] to transmit 100 kW to the cavity. Based on the available cooling capacities of the cryocoolers and the heat load generated by the cavity, only about 2 W of RF losses are allowable at 4.2 K. Achieving this requires significant RF optimization and careful consideration of how the heat loads are distributed in the coupler.

The following sections will present and discuss the design solutions to these main challenges, along with designs chosen for other important components of the cryomodule. All RF simulation was performed using CST Studio Suite (high-frequency solver) [Das22] while thermal and mechanical analysis was performed in Ansys Mechanical [Ans23]. Key material properties for these calculations are: electrical conductivity (RF); temperature-dependent thermal conductivity (thermal); density and isotropic elasticity, which requires Young's modulus and Poisson's ratio (mechanical). There are many more properties that can be added to the various simulations to enable calculation of more intricate quantities, but the few listed here are sufficient for what is used in this work. Values for such material properties can typically be found in online resources such as NIST [BR13] and MatWeb [Mat24].

5.2 A New SRF Cavity: LCC1-1

While the proof-of-principle study was able to rely on a regular 2.6 GHz cavity, the new system required a cavity which was better optimized for (a) the operational goals of the cryomodule and (b) a conduction-cooled setup. This meant a new

[1] Updated power delivery targets will be discussed in section 5.3.

cavity had to be designed in order to meet these needs. Dubbed LCC1-1 – for **L**TE band, **C**onduction **C**ooling, **single**-cell, **first** cavity made – this section will discuss the design process for the new cavity, taking into account both RF and thermal requirements.

5.2.1 RF Design

Though many different cavity shapes exist, elliptical cavities (and slight variations of them) are currently the standard choice for $\beta = 1$ accelerating structures. To determine the best design approach for LCC1-1, the following operational goals were considered:

1. Achieve stable cavity operation at 10 MV/m, providing approximately 1 MeV energy gain (for a relativistic beam).
2. Maintain a high cavity Q_0 of $\sim 1 \times 10^{10}$ at this accelerating gradient to ensure low dissipated power.
3. Carry high beam current (100 mA) for high throughput applications, such as those mentioned earlier.

The third goal in particular suggested that the 1.3 GHz 2-cell injector cavities of Cornell's Energy Recovery Linac (ERL) development [B$^+$02] would provide a good starting point for designing LCC1-1. The injector cavities were designed for high current as well as strong HOM damping due to all relevant HOMs propagating into one of the two (asymmetric) beam tubes [SBG$^+$03]. To simplify the design, a single-cell cavity was desired over the original 2-cell version. This was achieved by removing the center half-cells and joining the two end half-cells; this ensured that

Parameter	ERL 2-cell	LCC1-1	Units
Freq.	1300	1300	MHz
G	–	263	Ω
R/Q	218	106	Ω
$E_{pk}/\sqrt{U}$	–	16.7	$(MV/m)/\sqrt{J}$
E_{pk}/E_{acc}	1.94	2.06	–
B_{pk}/E_{acc}	4.28	4.44	mT/(MV/m)

Table 5.2: Comparison of cavity parameters for the Cornell ERL 2-cell injector cavities [SBG+03] and LCC1-1. This table is an abridged version of Table 2.2.

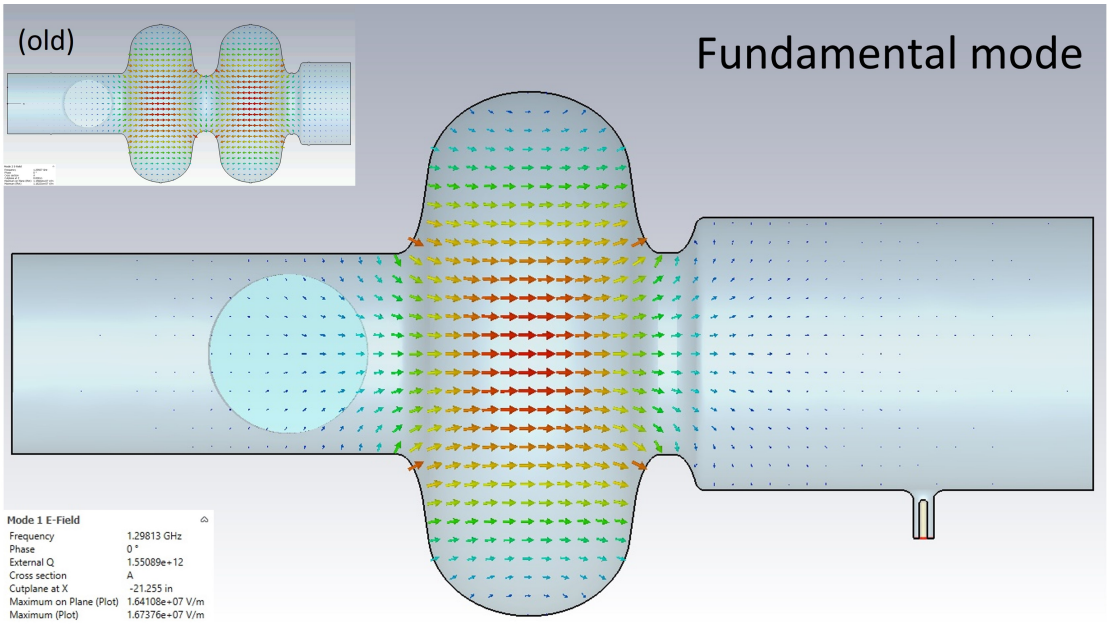

Figure 5.1: Fundamental accelerating mode (π-mode) for LCC1-1. The inset shows the 2-cell design from Cornell's ERL injector cavities for comparison.

LCC1-1 would have the same desired RF properties. The cavity parameters (e.g. E_{pk}/E_{acc}) were only slightly altered by this modification – see Table 5.2. Figure 5.1 shows the fundamental accelerating mode of LCC1-1, with that of the original 2-cell design for comparison.

Combining the first two operational goals indicates that the cavity must maintain a $Q_0 \sim 1 \times 10^{10}$ at an accelerating gradient of 10 MV/m. Achieving this at 4.2 K, for use with cryocoolers, is what necessitates the use of Nb_3Sn over pure

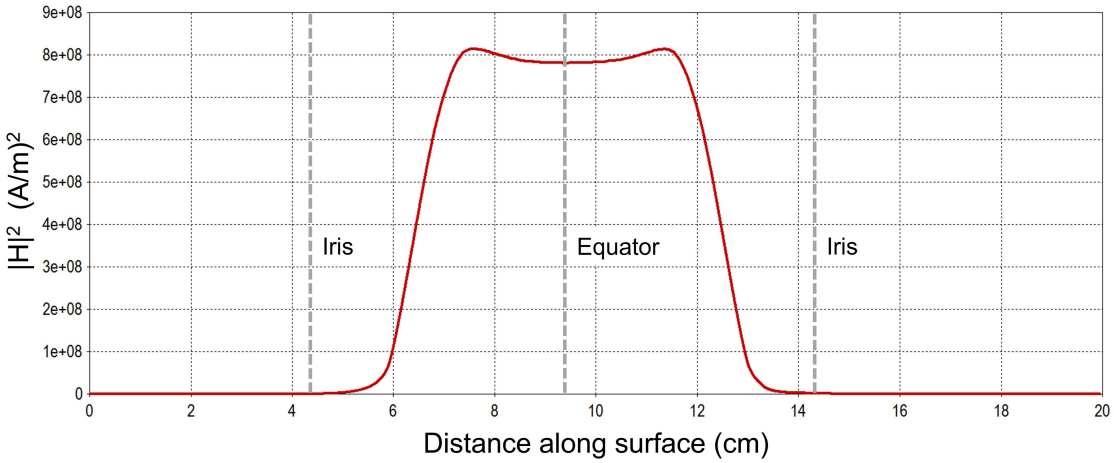

Figure 5.2: Plot of $|H|^2$ along the RF surface of LCC1-1 for an accelerating gradient of about 8 MV/m (simulations are normalized to $U = 1$ J). Note that the total cavity length is about 42 cm; this plot focuses on the central cell.

niobium. Thus LCC1-1 would need to receive a standard Nb_3Sn coating via the usual thermal evaporation process used at Cornell (see Chapter 2 and e.g. [Por21]). Using LCC1-1's cavity parameters, a Q_0 of 1×10^{10} at 10 MV/m predicts a dissipated power of about 1.25 W. The dissipated power distribution is proportional to $|H|^2$; Figure 5.2 shows this quantity as calculated on a curve along the surface of LCC1-1.

5.2.2 Thermal Link Design

While the RF design essentially determines the inner shape of the cavity, the outer structure is determined by the thermal requirements. In this case, the cavity had to be compatible with a conduction cooling system. This conduction design had to meet the following requirements:

1. A direct connection to the cavity equator is needed to remove the dissipated power during RF operation.

2. Thermal gradients across the cavity during cooldown must be minimized to improve cavity RF performance.
3. Efficient thermal connections are needed to maintain a cavity temperature near 4.2 K during RF operation.

The first requirement is based on findings from the proof-of-principle study, in which only including a thermal connection at the cavity beam tubes resulted in the equator reaching temperatures up to 0.5 K higher than the rest of the assembly. This can be remedied by welding niobium rings directly to the equator region which are then bolted to high-purity (5N) aluminum rings to provide high thermal conduction; this approach is inspired by Fermilab's work discussed previously [DPG+20]. In order to best extract the cavity heat load based on the distribution profile shown in Figure 5.2, these niobium rings are each located 2 cm outboard of the equator.

The second requirement is met by also including niobium rings welded near the cavity irises. Similarly, these rings will have 5N aluminum rings bolted to them to improve the thermal performance. These iris rings extract smaller heat loads near the beam tubes while also acting as mounting points for resistive heaters. As shown in the previous study, using independently controlled heaters on both sides of the cavity during a cooldown or temperature cycle was the most reliable way to achieve the minuscule thermal gradients needed for Nb_3Sn cavities to reach optimal RF performance. In order to minimize the generation of magnetic fields near the cavity while using the heaters during cooldown, non-inductively wound $\sim$1 kΩ resistors are used with twisted-pair wiring.

A sufficient thermal connection between the cavity and cryocoolers requires the use of materials with especially high thermal conductivity around 4.2 K. As

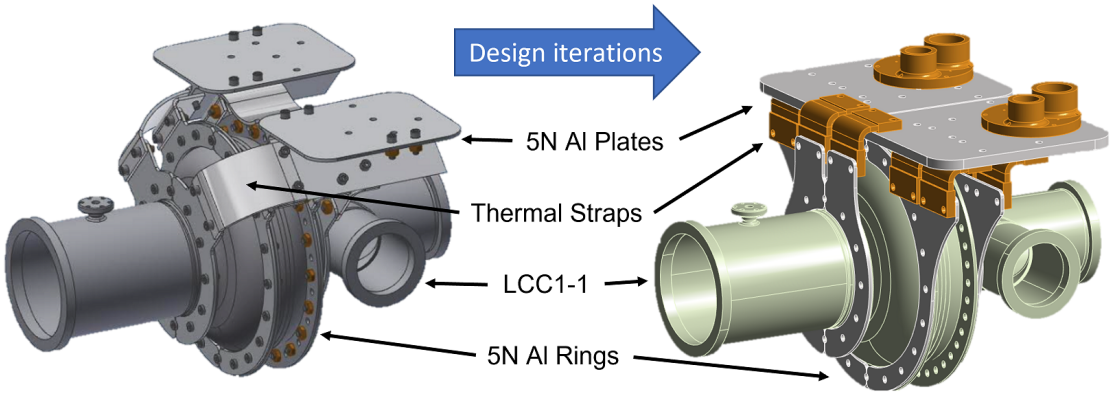

Figure 5.3: Original and final versions of the 4.2 K link design connected to the cavity. Factors that contributed to the design changes include vendor challenges, spatial limitations, overall simplification and cost reduction.

discussed in Chapter 3, only high-purity (e.g. 5N) aluminum and copper satisfy this need. While it was originally planned to use 5N aluminum foil straps for the connection between the cavity and cryocoolers, challenges which arose during discussions with available manufacturers made this option less attainable. Other factors such as spatial limitations and preferring a simpler design also played a role. In addition, the increase in production cost and lead time for ultra high-purity foil straps, compared to more typical high-purity braided straps, often far outweigh the increase in thermal performance. With this in mind, P5-502 CuTS (braided copper thermal straps) from TAI were chosen; a total of twelve straps are used to connect the cavity to the cryocoolers, with four straps per equator ring and two straps per iris ring. CAD models of the original and final 4.2 K thermal link design connected to LCC1-1 can be seen in Figure 5.3.

To test the effectiveness of these design choices, thermal modeling of the cavity and full beam line was performed. The first thermal boundary condition applied is a 1.5 W heat load to the inner surface of the cavity cell; this comes from the expected heat load of 1.25 W discussed previously with an additional safety factor. For simplicity, the heat load distribution (see Figure 5.2) is approximated as a

rectangular pulse function. The next set of boundary conditions are fixed temperatures along the assembly: the cryocooler 2nd stages are fixed at 4.2 K, copper thermal straps connected to the ends of thin-walled transitional beam tubes are fixed at 55 K[2], and finally the outer ends of the beam tubes are held at room temperature.

Resulting temperature profiles from these thermal simulations can be seen in Figure 5.4. The top left image shows more detail of LCC1-1 and the 4.2 K thermal link, with the ends of the beam tubes reaching about 4.6 K. The top right image focuses just on LCC1-1, showing that the cavity cell temperatures remain at or below 4.4 K. Given that the cavity equator temperatures are < 0.1 K warmer than the iris temperatures (compared to about 0.5 K in the proof-of-principle study), it is clear that the main cavity heat load is better extracted with this design, and thus the first thermal design requirement is met. Considering the safety factor included for the simulated cavity heat load, the resulting cavity temperatures remaining close to 4.2 K confirms that the third requirement is satisfied. The bottom image shows the temperatures along the entire beam line along with the boundary conditions described previously; components outside of the cavity and 4.2 K thermal link will be discussed in a later section.

While a static thermal analysis cannot directly test the second requirement, as it pertains to active cooldowns of the system, it is very reasonable to believe that the heaters mounted on the iris rings will provide effective control of thermal gradients, just as they did in the previous study. In addition, the top right image of Figure 5.4 shows very uniform cooling between the two irises even without heater control taken into account. This further suggests that minimizing the thermal

[2]This temperature was determined by analysis of the thermal shield and related components, as discussed in section 5.4.

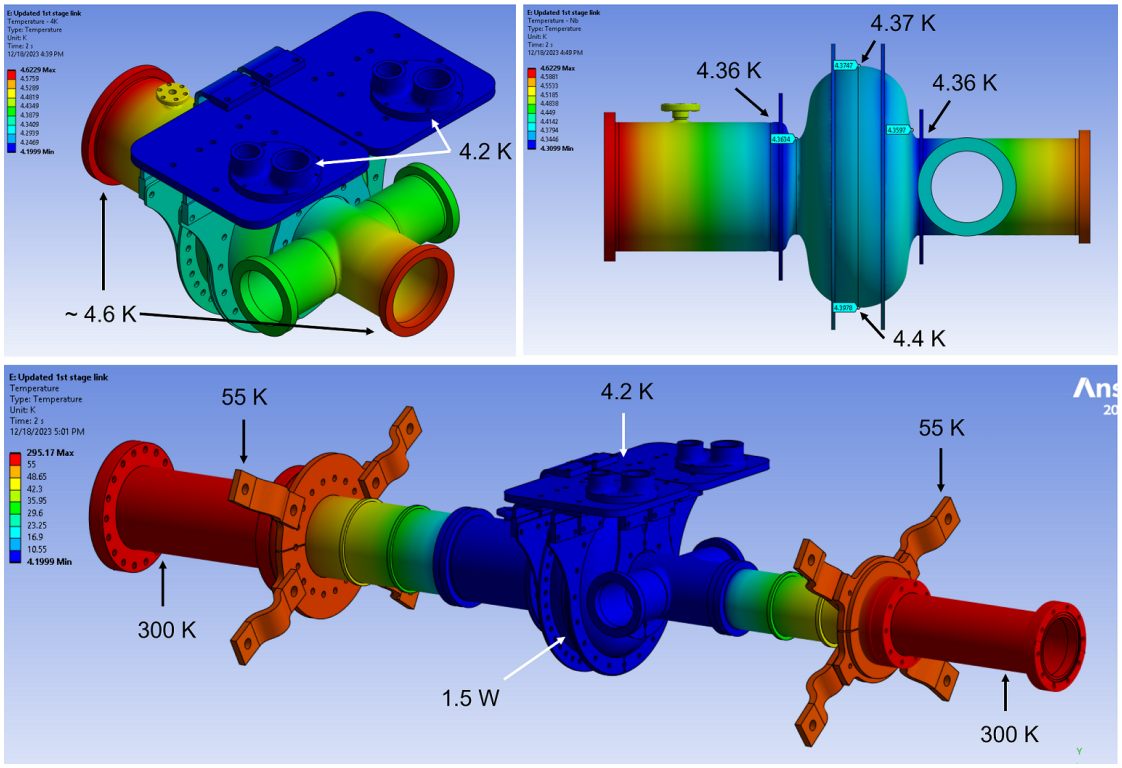

Figure 5.4: Results of thermal simulations completed in Ansys. Top left: detailed view of LCC1-1 and 4.2 K thermal link, showing the ends of the beam tubes at 4.6 K. Top right: detailed view of LCC1-1 only, showing temperatures around the cavity cell at or below 4.4 K with a thermal gradient of just 0.03 K around the equator. Bottom: view of the full beam line with thermal boundary conditions indicated.

gradients during cooldown is attainable with this design, thus confirming that all of the requirements laid out for the cavity's thermal behavior have been met.

5.3 Forward Power Coupler

Based on the high power delivery required for the new coupler, the design process again used the injector module from Cornell's ERL as a starting point. The ERL injector couplers were designed to handle high average power (target 75 kW) with strong coupling ($Q_{\text{ext}} = 4.6 \times 10^4$) to deliver power to a beam with a current up

to 100 mA [VBL+05]. While these power delivery capabilities match very closely to those desired for the new coupler, the resulting heat loads are well above the new system's limitations; more detail can be found in the following discussion on design challenges. The injector couplers use a twin coaxial design meant to reduce the transverse kick applied to the beam. Using twin couplers means that for the original operational goal of the new cryomodule, each of the new couplers would only need to deliver 50 kW to the beam. However, during the design process there was increasing interest in pushing the capabilities of the couplers further such that each one could deliver up to 100 kW. The remainder of this section will present the completed design process for the new couplers, addressing the main challenges and considerations involved. This discussion will closely follow what was written for the proceedings of SRF 2023 [SHL+23a].

5.3.1 Primary Challenges

Although the ERL injector couplers provided a good starting point for the new design, many modifications were required for the couplers to be usable in the new conduction-cooled cryomodule. These can be summarized by the following challenges which were used to guide the design process:

1. Enable up to 100 kW operation (per coupler) while reducing 4.2 K heat load to ~ 1 W.
2. Remove all fluid cryogenic cooling and replace with conduction-cooling capabilities.
3. Reduce cost by simplifying overall design while maintaining necessary functionality.

The result of these design changes is illustrated in Figure 5.5, where Figure 5.5a shows a CAD model of the ERL injector coupler and Figure 5.5b shows the newly designed coupler for the conduction-cooled system. Both models have key components labeled, many of which will be focused on in the discussions below.

The first challenge presented the most significant obstacle to overcome. This restriction indicates that the heat load at 4.2 K must be a factor of about 100000 smaller than the targeted forward power. For comparison, the ERL injector couplers have a heat load of ~ 3 W at 5 K for 75 kW operation per coupler [VBL+05]. Reducing the 4.2 K heat load by a factor of 3 while increasing the forward power by 33 % required significant optimization of the coupler's RF design in order to minimize reflections and improve heat load distribution.

One key factor was the use of an "RF shield" to act as the outer conductor of the coaxial line – see Figure 5.5b. This shield was inspired by a design developed at Fermilab [DPG+20], which was then further modified for use in the new coupler [She22]. The purpose of this RF shield is to reduce the heat load at 4.2 K by "redirecting" the RF losses to the 45 K heat load. This is done by ensuring that the shield is only thermally anchored to the 45 K intercept, which is accomplished using small ceramic spacers at both ends to prevent thermal contact to colder or warmer components.

Another design optimization was the addition of a quarter-wave transformer to each side of the inner bellows. The bellows represent a perturbation in the coaxial line impedance, and thus will generate reflections unless properly compensated. In addition, the perturbation varies as the bellows are stretched or compressed. To mitigate this effect and maintain low reflections, a small length of the inner conductor on both sides of the bellows can have its radius increased slightly. This

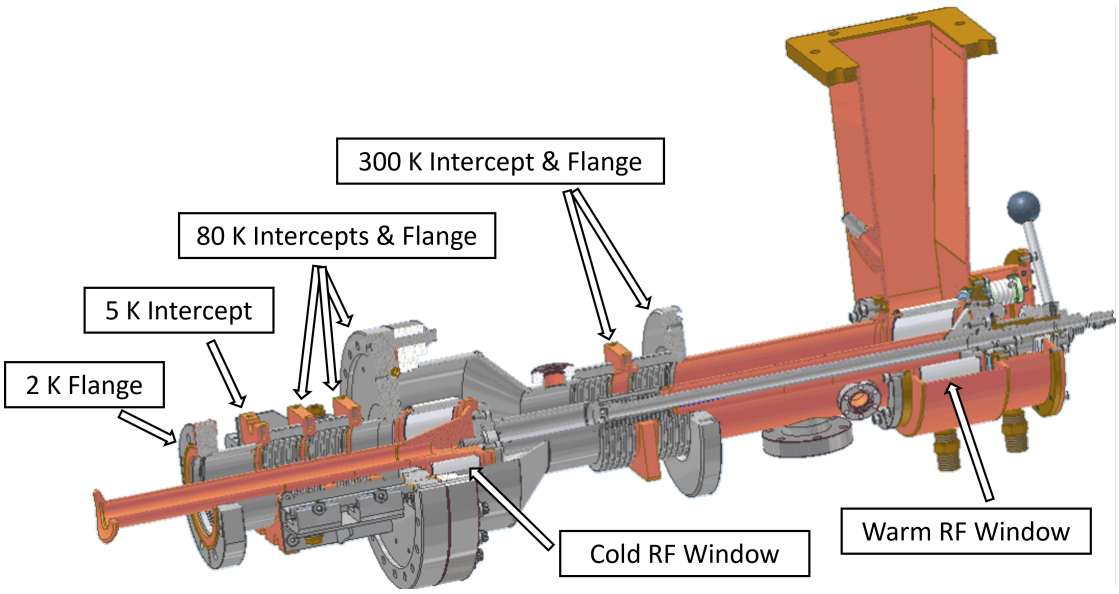

(a) ERL injector coupler

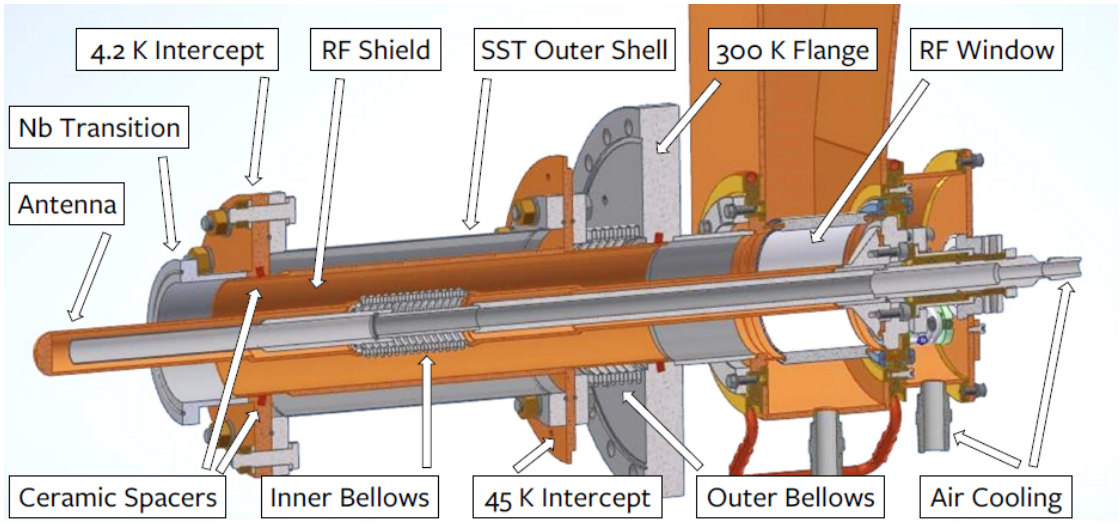

(b) New conduction-cooled coupler

Figure 5.5: (a) CAD model of the ERL injector coupler [VBL+05] with the various heat intercepts and two RF windows highlighted. The intercepts in this coupler use heat pipes carrying gaseous cryogens for effective cooling. (b) Final design of the high-power couplers for Cornell's new conduction-cooled cryomodule. The Nb transition piece connects to the RF coupler ports on LCC1-1 such that the antenna end is flush with the cavity beam tube.

presents a more gradual impedance change in the coaxial line. The relevant length is roughly $\lambda/4 \approx 58$ mm, hence the term quarter-wave transformer. The radius of

the transformer section is then optimized in order to minimize reflections for the full ± 8 mm stroke of the inner bellows [She22].

The second challenge relates to how the heat loads can be extracted from the new coupler. In Cornell's ERL injector modules, heat pipes bring liquid cryogenics directly to the heat intercepts placed at different stages of the coupler, as shown in Figure 5.5a. This method was used to handle the high heat loads associated with continuous high-power operation [VBL$^+$05]. In the new cryocooler-based, cryogen-free cryomodule, however, similarly high heat loads must be extracted via a conductive path between the coupler intercepts and cryocooler cold heads. As such, it must be ensured that the heat intercepts offer strong thermal contact to both the coupler components as well as the thermal path which will be used to extract the resulting heat. This motivated the use of large copper disks for the intercepts, which would provide a reliable connection between the coupler's RF surfaces and the rest of the thermal path to the cold heads. These intercepts can be seen in Figure 5.5b.

The third challenge is motivated by reducing the complexity and cost of the system to make it more accessible and reliable. Simplifying the coupler design results in fewer possible points of failure and a simpler assembly and installment process. Two major steps taken to achieve this were removal of the cold RF window and only using one set of outer bellows; these changes can be seen between Figure 5.5a and 5.5b. Taking out the cold window significantly simplifies the "cold" portion of the new coupler and also eliminates any concern of particles being ejected out of the cavity and striking the ceramic. While the ERL injector couplers had multiple sets of bellows to accommodate significant transverse deflection of the coupler, the new design is reduced to a single set of bellows which is only required

to allow for thermal contraction.

The remaining sub-sections will discuss the results of RF and thermal simulations using the new coupler design, as well as structural considerations which were studied. It should be noted that the RF and thermal simulations were part of an iterative process which led to the design solutions discussed above, and it will only be the final results which are shown below.

5.3.2 RF & Thermal Simulation

RF design of the coupler was performed by analyzing key components (e.g inner bellows, RF shield) individually before combining everything into a full model[3]. Figure 5.6 shows the final model as constructed in CST. The waveguide portion of the model (seen on the right end) was directly modeled after the ERL injector couplers, while the remaining components were newly designed. Of particular interest are the RF shield and inner bellows with quarter-wave transformers as discussed previously. Frequency domain simulations were used to minimize the input power reflection coefficient S_{11} at the operational frequency of 1.3 GHz, where

$$S_{11} \equiv 10 * \log_{10}(P_r/P_f) \tag{5.1}$$

and is given in decibels (dB). As seen in Figure 5.7, this optimization achieved an S_{11} value of less than -80 dB, indicating the reflected power is a factor of 10^8 smaller than the forward power. This ensures that there are no significant reflections in the coupler, which would unnecessarily increase the resulting heat loads.

[3]Many thanks to Valery Shemelin, who performed the groundwork RF design for the coupler.

In addition, the antenna tip was modified to obtain optimal beam coupling at full extension of the inner bellows. The optimal coupling is given by [PKH08]:

$$Q_{\text{ext}} \approx \frac{V_c^2}{P_b(R/Q)} = \frac{V_c}{I_b(R/Q)}, \tag{5.2}$$

where V_c is the cavity voltage, P_b is the power delivered to the beam, (R/Q) is the shunt impedance, and I_b is the time-averaged beam current. Using $V_c = 1\,\text{MV}$ ($10\,\text{MV/m} * 0.1\,\text{m}$ effective accelerating length for LCC1-1), $I_b = 100\,\text{mA}$ and $(R/Q) \approx 100\,\Omega$, an optimal value of $Q_{\text{ext}} \approx 10^5$ is found. Since there are two couplers delivering power, the antenna end was designed to achieve a Q_{ext} of 2×10^5 per coupler. With the inner bellows fully compressed, the maximum Q_{ext} is 1.77×10^6, offering nearly a full order of magnitude variation.

The RF model in Figure 5.6 also shows the resulting material losses calculated for the various components of the coupler. These losses were then applied as heat loads to a separate mechanical model in Ansys to simulate the thermal response to different levels of forward power, namely 0, 50 and 100 kW. These levels represent static conditions, the original operating specification, and the updated target power. Additional boundary conditions applied in the model include: thermal radiation on all inner surfaces of the coupler; air cooling of the RF window and inner conductor; RF shield intercept held at 45 K; transition piece intercept held at 4.2 K.

Results of the thermal simulation corresponding to 100 kW forward power are shown in Figure 5.8. The entire RF shield remains near 45 K, indicating good thermal isolation thanks to the ceramic spacers. In addition to protecting the 4.2 K components, the RF shield also prevents overheating on the outer bellows. As shown, the maximum temperature on the bellows is just under 310 K, even without the use of copper plating (see Figure 5.6). The maximum temperature on

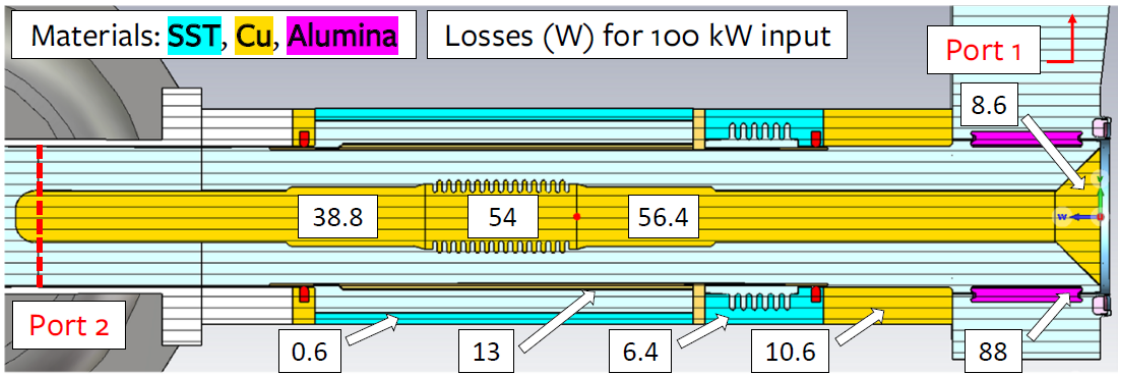

Figure 5.6: RF model of the newly designed coupler. Material assignments are indicated via the highlighted text in the upper-left corner; white components are perfect conductors and lighter blue areas are vacuum. Port locations are shown in red while the boxed numbers list the resulting RF losses (in Watts) for 100 kW forward power. Note that all (non-vacuum) components shown are cylindrically symmetric, and all heat loads labeled are for the entire component.

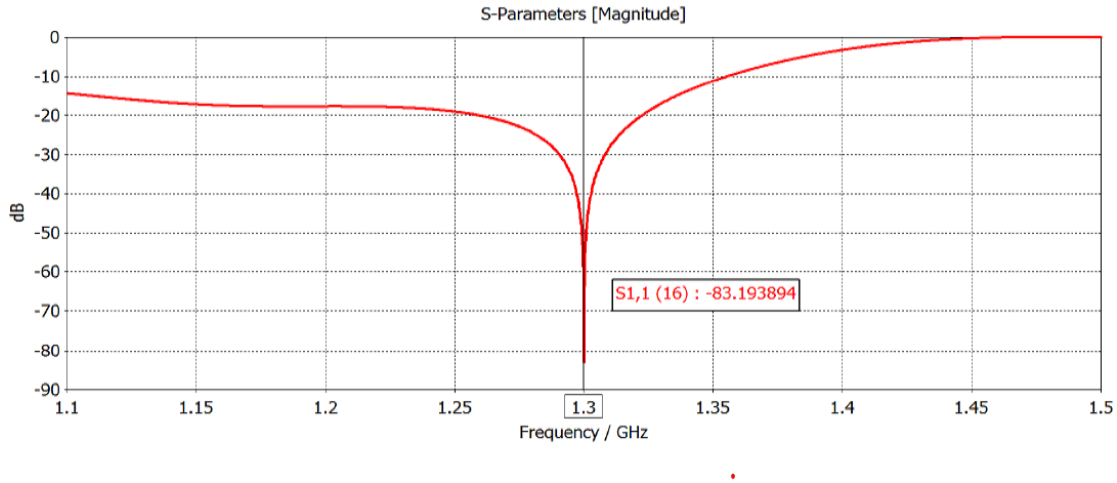

Figure 5.7: Optimized S_{11} parameter, shown between 1.1 and 1.5 GHz. Minimum S_{11} achieved is less than -80 dB at 1.3 GHz.

the inner conductor is just over 350 K, which occurs on both the inner bellows and the end of the antenna. The RF window only warms up to about 325 K due to the direct air cooling provided.

Table 5.3 lists the resulting heat loads for the new coupler at 4.2 and 45 K for various forward powers P_F, along with the heat loads from the ERL injector coupler at 5 and 80 K for 75 kW forward power. This shows that the heat loads

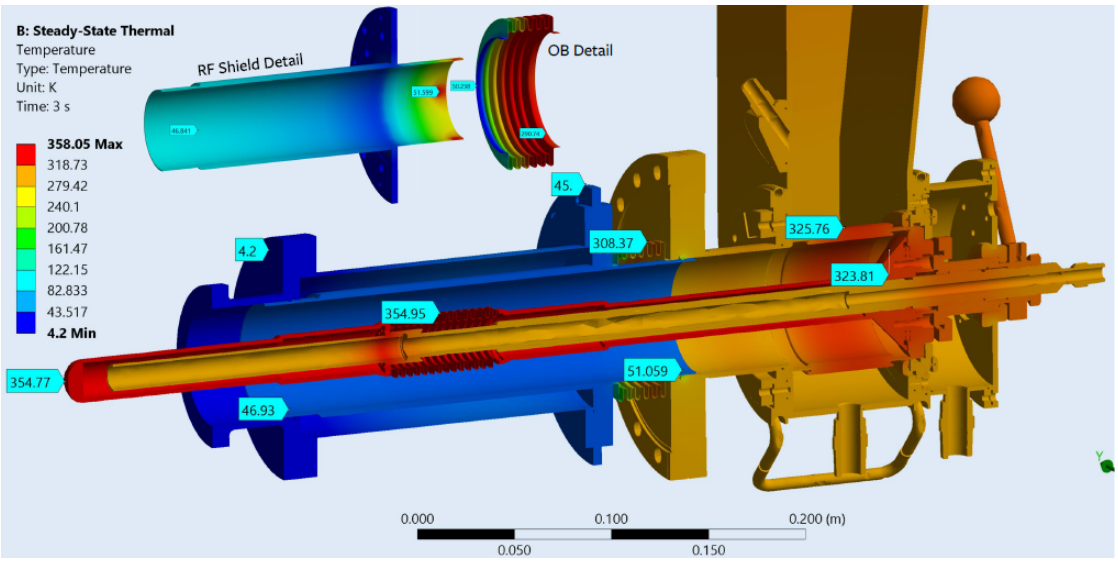

Figure 5.8: Results of a thermal simulation for 100 kW forward power in the coupler. The temperature scales for the two inserts are different from that of the main model, and are included to show more detailed temperature profiles of the RF shield and outer bellows. Associated heat loads are listed in Table 5.3.

Coupler Heat Loads (W)				
	New Coupler:		ERL Injector*:	
P_F (kW)	at 4.2 K	at 45 K	at 5 K	at 80 K
0	0.46	21.1	–	–
50	0.80	29.5	–	–
75	–	–	~ 3	< 75
100	**1.11**	**37.9**	–	–

* [VBL+05]

Table 5.3: Coupler Heat Load Comparison

in the new coupler have successfully been reduced compared to the ERL injector coupler, even for a higher forward power. Especially important is the 1.11 W heat load at 4.2 K for 100 kW forward power in the new coupler, as this confirms that the first primary design challenge for the coupler has been satisfied. With the second and third challenges being addressed by the design choices discussed, all of the RF and thermal requirements for the new coupler have been satisfied.

5.3.3 Potential Multipacting

One drawback of the RF shield is that the small gap between the end of the shield and the rest of the coupler's outer conductor (for example the 4.2 K intercept) can be susceptible to multipacting. Multipacting refers to a cascade of electron collisions which can occur if (a) the electron time of flight between two surfaces matches the period of the oscillating fields and (b) the surface materials eject one or more electrons when they are struck [PKH08]. Multipacting is detrimental to RF performance (in both cavities and couplers, for example), as the continuous ejection of more electrons absorbs much of the RF power available, and the electrons striking the RF surfaces can cause excessive heating [PKH08]. In general, multipacting conditions are difficult to solve for analytically, and complex geometries are tested for potential multipacting using specialized software [YOP01].

Simple geometries such as two parallel plates, meanwhile, do have analytical solutions for multipacting conditions [SB20]. Since the gap between the RF shield and the 4.2 K intercept is much smaller than the radius of the RF shield, this region can be approximated as two parallel plates. The multipacting band, or the set of gap sizes and field conditions that can lead to multipacting, for this geometry is indicated by the grey shaded region in Figure 5.9. The vertical dashed lines correspond to different values of the gap size d between the RF shield and 4.2 K intercept. The coupler design uses $d = 0.6$ mm, as this value avoids the multipacting band for any gap voltage (i.e. any forward power sent through the coupler). However, small imperfections in machining and/or assembly may lead to slight variation from this ideal value. While any smaller gap still avoids multipacting altogether, Figure 5.9 shows that even a gap of $d = 0.7$ mm starts to enter the multipacting band for certain power levels.

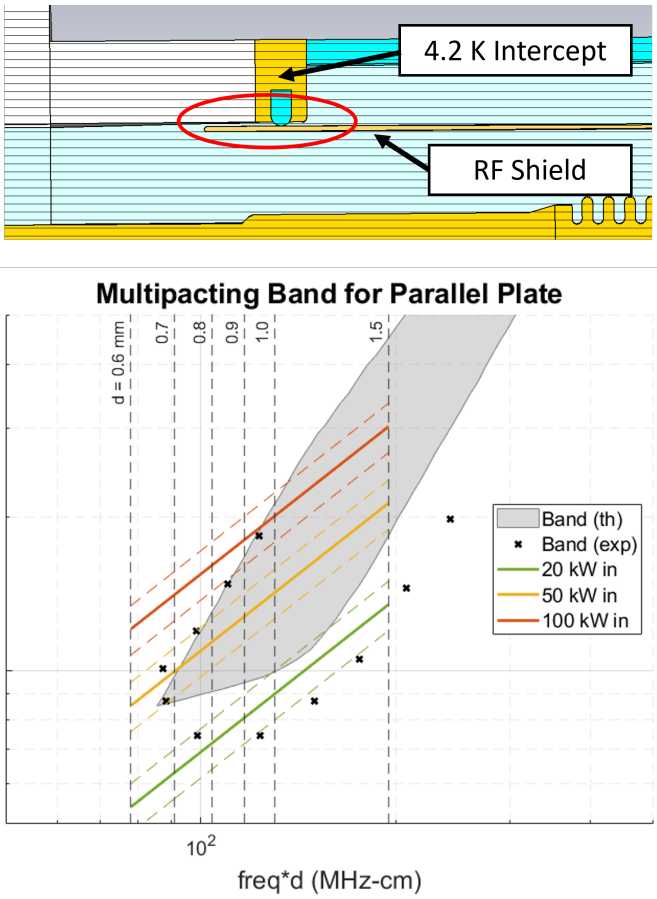

Figure 5.9: Potential multipacting in the forward power coupler between the RF shield and 4.2 K intercept. Above: detail of potential multipacting location. Below: Plot of the gap voltage vs the product of the oscillating field frequency and gap distance. The shaded region indicates the theoretical bounds of the multipacting band [SB20], while black X's indicate experimental values for the boundary [HW54]. The colored lines correspond to different amounts of forward power (dashed lines represent error bounds).

While this may seem to be a critical flaw, multipacting is often able to be processed through if it does occur. This typically involves sending high power to the component (cavity or coupler) to actually increase the intensity of the multipacting, such that the electron collisions can gradually "clean up" the RF surfaces until they no longer emit more electrons [PKH08]. Even if this were to fail, Figure 5.9 indicates that operating at a lower forward power of 20 kW would avoid the (theoretical) multipacting band regardless of the size of the gap between the RF

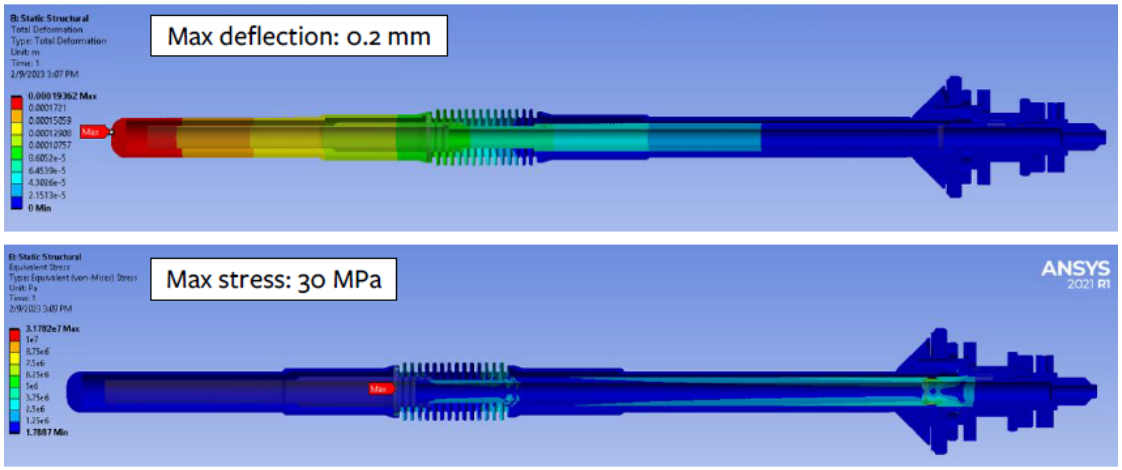

Figure 5.10: Top: Total deformation of the inner conductor assembly, showing a maximum deformation of 0.2 mm at the antenna tip. Bottom: Total stress (von-Mises) in the inner conductor assembly, showing a maximum of about 30 MPa.

shield and 4.2 K intercept.

5.3.4 Structural Stability

Once the RF and thermal behavior of the coupler was understood, a couple areas of concern had to be examined for structural stability before fully finalizing the design. The inner conductor assembly became a concern due to the removal of the cold RF window from the coupler. Eliminating this intermediate support results in a long lever arm acting on the connecting joint which mounts the inner conductor to the rest of the coupler body (see the right side of Figure 5.5b). In addition, the flexibility of the inner bellows puts more stress on the tuning rod assembly inside the inner conductor, as the end of the inner conductor would otherwise be unsupported. The wall thickness of the first segment of the tuning rod was increased to help address this concern.

Figure 5.10 shows deformation and stress results from a structural analysis

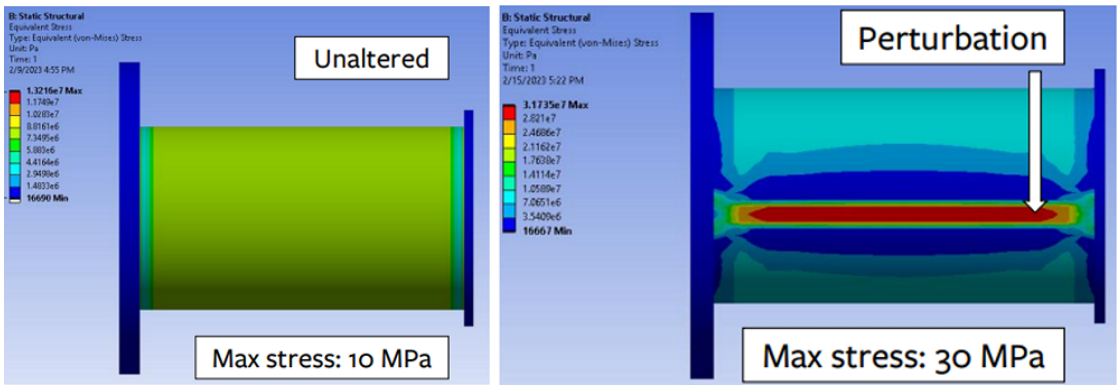

Figure 5.11: Left: stress results for the unaltered steel shell, showing a maximum stress of about 10 MPa. Right: stress results for the steel shell with a perturbation added, showing a maximum stress of about 30 MPa.

performed in Ansys. A maximum deformation of 0.2 mm is seen at the end of the inner conductor, while a maximum stress of about 30 MPa is seen where the tuning rod connects to the inner conductor at the far end of the bellows. The tuning rod is made of 316 stainless steel, which has a yield strength between 200-300 MPa. This confirms that the assembly stresses are well within a safe operating range. A modal analysis was also performed on the structure, which showed a fundamental mechanical resonance mode at 44 Hz. While there was an original attempt to adjust the design to increase said mode frequency above 60 Hz, it was found that the necessary increase in rigidity was impractical – for example, further increasing the tuning rod wall thickness so much that the air cooling capabilities would be significantly hindered. Therefore, it was decided to keep the original design with a fundamental mode at 44 Hz.

A second area of concern was the outer steel shell between the 45 K and 4.2 K intercepts. This component is used as a heat dam to minimize heat flow between the two intercepts. As such, it has a wall thickness of only 0.5 mm. During the eventual assembly of the full cryomodule, the coupler will be pumped under vacuum with the cavity while still surrounded by atmospheric pressure. As such, a structural

analysis was completed for this component to check for stability against buckling. Results of this analysis are shown in Figure 5.11, both for an unaltered model as well as one in which a perturbation was introduced to the cylindrical shell. This was done to check how much of an effect an imperfection in the cylindrical structure would have. The unaltered model had a maximum stress of about 10 MPa, while the perturbation increased the maximum stress to about 30 MPa. Both of these values are well within the yield strength of 316 stainless steel, confirming that this component will withstand the expected pressure difference without modifications.

5.4 Cryostat and Auxiliary Components

While the cavity and coupler represent the two most individually complicated components of the system, the rest of the cryomodule presents its own challenges. The design of the remaining cryomodule components was guided by the following considerations:

1. After taking into account the heat loads of the cavity and couplers, only $\sim$0.5 W remains at 4.2 K for the remaining components.
2. Overall size and complexity should be minimized to reduce weight and cost.
3. Components must accommodate thermal contraction and mitigate vibrations.

These points offer a combination of thermal and mechanical requirements along with an overall goal of removing any unnecessary parts where possible. This section will discuss some of the main components that address these considerations: the vacuum vessel, thermal shield and thermal link, beam tube bellows and transition

pieces, support structures, and sensors and instrumentation. Figure 5.12 shows the completed cryomodule design with these components indicated. LCC1-1 is also visible in the center. The couplers are not shown in this view, but they would be connected to the side RF ports of the cavity when in use.

5.4.1 Vacuum Vessel

While larger cryomodules often use cylindrical vacuum vessels for the improved structural stability, a basic rectangular shape is generally simpler and easier to fabricate for a small system such as this one. However, a rectangular vessel requires the addition of stiffening ribs to prevent buckling when the system is pumped down to vacuum. As such, multiple rounds of structural modeling were performed to produce a satisfactory layout of the stiffening ribs. Achieving $\sim 1\,\text{mm}$ or less of deflection was used as a primary metric for each panel. The stress safety factor was also considered to ensure there were no isolated regions of excessively high stress, which could lead to mechanical failure. The vessel panels and stiffening ribs are all made of 304 stainless steel; the panels are 0.25 inch thick while the ribs are 0.5 inch wide and 1 inch high, with the exception of those on the top panel which are 1.5 inch high (same width).

Figure 5.13 shows various examples of different stages of the vacuum vessel design and stiffening rib optimization process. Image (a) shows the vacuum vessel top panel without any ribs added; with a maximum deflection of almost 2.5 mm, this is insufficient on its own. Image (b) shows the result of the optimization process for the top panel – a maximum deflection of only 0.9 mm has been achieved, satisfying the goal of 1 mm or less. Image (c) shows the final structural model of the full vacuum vessel, in which all panels have completed the optimization process. The

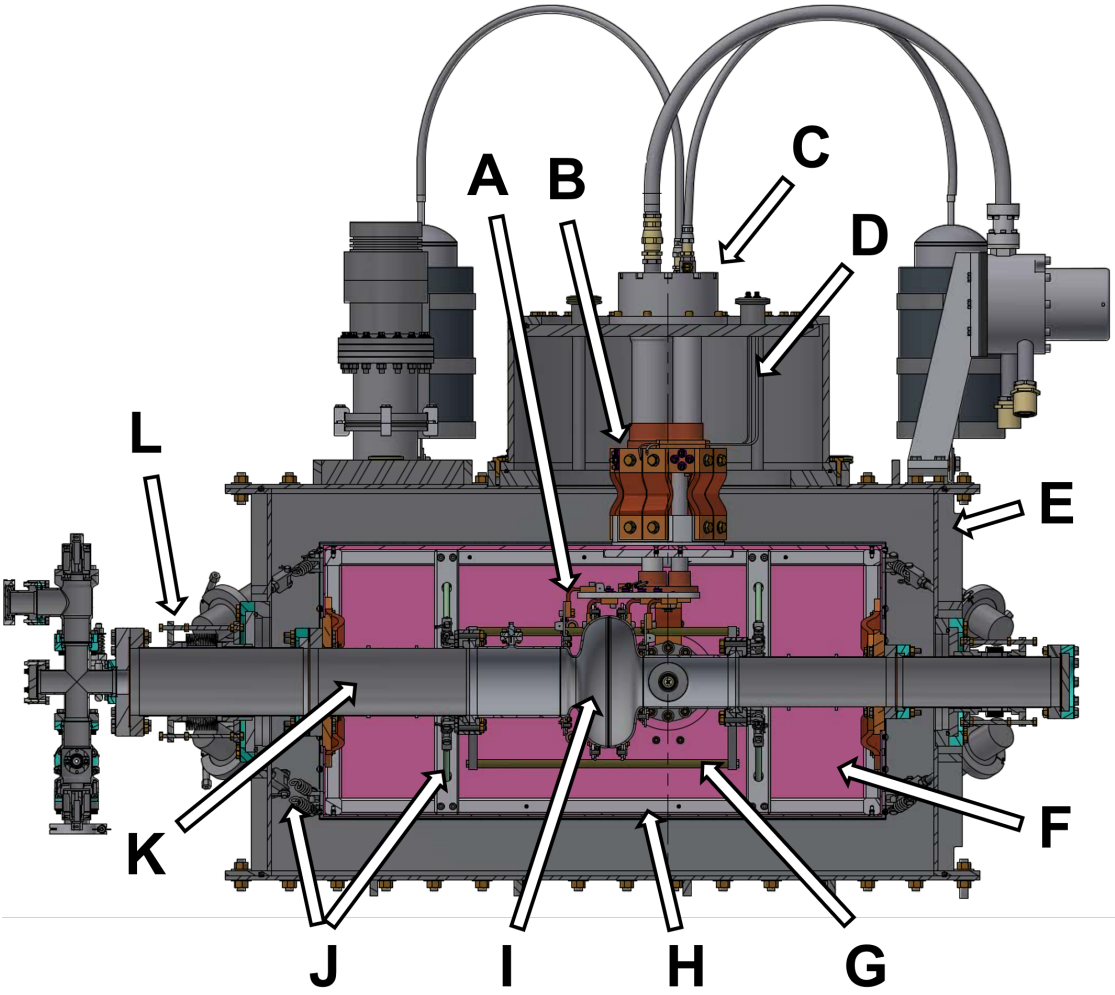

Figure 5.12: CAD model of the final cryomodule design highlighting the following components (clockwise from above): (A) 4.2 K thermal link, (B) 45 K thermal link, (C) cryocooler cold head assembly, (D) RF cables (forward/reverse and transmitted), (E) vacuum vessel, (F) thermal and magnetic shielding, (G) titanium support rods, (H) aluminum support frame, (I) cavity LCC1-1, (J) G10 support rod assemblies, (K) thin transitional beam tubes, (L) beam tube bellows. Many of these components are discussed and shown in further detail in the rest of this section. The design of LCC1-1 and the 4.2 K thermal link was discussed in section 5.2. The forward power couplers discussed in section 5.3 are not shown in this view, but are connected to the cavity's RF coupler ports.

legend in this image shows a maximum deflection of about 1.05 mm which occurs on the large beam tube end panel. With various attempts at modifying the layout proving unsuccessful, this was deemed close enough to the target deformation to

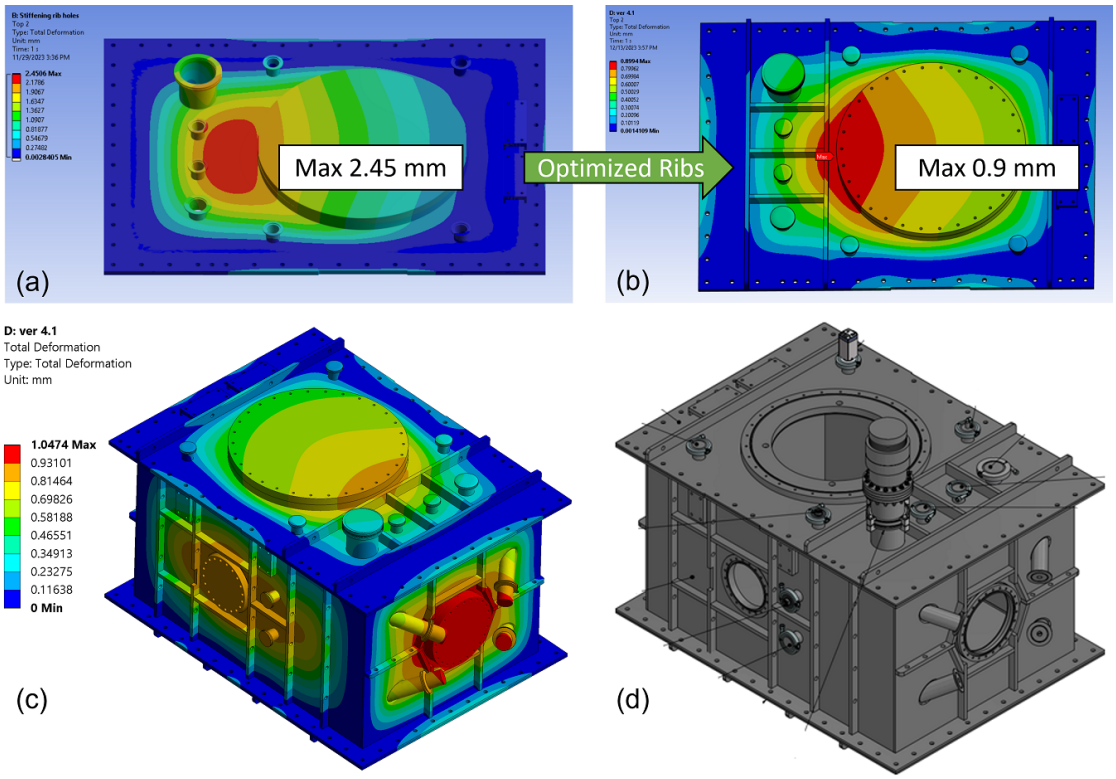

Figure 5.13: Various stages and components of the vacuum vessel design process: (a) Top panel with no stiffening ribs; (b) Top panel with optimized stiffening rib layout; (c) Final structural model of the vacuum vessel with stiffening ribs optimized on all panels; (d) Final CAD model of vacuum vessel.

be satisfactory. Image (d) shows the final CAD model of the vacuum vessel, with some external instrumentation also visible.

5.4.2 Thermal Shield

The use of a thermal shield at some intermediate temperature between room temperature and 4 K is crucial for reducing the static heat load at the coldest part of the system, e.g. an SRF cavity. The first factor comes from conductive heat leak which is proportional to $\Delta T/L$, where ΔT is the temperature difference between the ends of the connecting component and L is the length. Consider a beam tube

extending from a cavity at 4 K to room temperature. At a given spot on the beam tube a distance L away from the cavity, an intermediate heat intercept can be used to decrease the temperature at that spot by extracting some of the heat. Thus ΔT between that location and the cavity has been decreased, and so too is the remaining heat leak at the cavity.

An even larger factor is thermal radiation. Due to the cryomodule being under vacuum, heat is radiated freely between surfaces in a "line-of-sight" manner which is unaffected by the distance between them. The radiative heat transfer between two components is proportional to $(T_{\text{hot}}^4 - T_{\text{cold}}^4)^\dagger$ – a much more considerable temperature dependence than conductive heat transfer. While cryomodules with liquid cryogenics often cool their thermal shields somewhere between 40 - 80 K using either helium or nitrogen, the new system will cool the shield with the cryocooler 1st stages around 45 - 50 K. Using such a thermal shield results in the radiative heat load reaching the coldest components being reduced by a factor of about $(50^4 - 4^4)/(300^4 - 4^4) \approx 1/1300$. This difference illustrates how crucial it is to mitigate thermal radiation in cryomodule design.

The new thermal shield consists of Al-1100 panels mounted to a solid frame of 1 inch^2 Al-1100 bars; these can be seen in Figure 5.12 labeled "Thermal Shield" and "Support Frame". Most of the panels are 0.125 inch thick, while the top panels and upper coupler-side panels are 0.25 inch thick. The increased thickness on these four panels gives improved heat transport in the more critical areas of the shield, as determined in the thermal modeling discussed below. Al-1100 is used for the panels and frame as it has comparable thermal conductivity to high-purity copper near 50 K while having just one-third of the density. Commercial copper braid was

†Note that this expression is definitely not equal to $(T_{\text{hot}} - T_{\text{cold}})^4$, which the author definitely did not mix up when writing the first draft.

used for the thermal straps to connect the thermal shield to the cryocooler 1st stages and the heat intercepts on the couplers and beam tubes. These braids are 6 inches long with 300 kcmil wire equivalence, which provides sufficient thermal conductance across the strap.

Thermal modeling was performed to determine the expected temperature profile and heat loads at 45 K. Materials used in the model include Al-1100 (panels and frame), 50 RRR copper (thermal straps, typical for electrolytic tough pitch copper), 100 RRR copper (heat intercepts) and 316 stainless steel (beam tubes). Thermal boundary conditions applied include fixed temperatures of 300 K at the outer ends of the beam tubes, 45 K at the cryocooler mounts and 4.6 K at the inner ends of the beam tubes (based on cavity thermal modeling). Heat loads of 0, 21.1, 19.5 and 37.9 W are applied at the coupler intercepts to represent the conditions of no couplers, static load only, 50 and 100 kW forward power per coupler, respectively (based on coupler thermal modeling). A radiative heat flux of 1.5 W/m^2 is applied to all exterior surfaces – this value is expected based on the use of MLI surrounding the thermal shield assembly[4] [Baz21].

Figure 5.14 shows various results from this modeling. The upper image shows an example of the full temperature profile along with the locations of the thermal boundary conditions applied. This result corresponds to 37.9 W applied to the coupler intercepts, but not much detail of the thermal shield itself can be seen due to the large temperature range across the beam tubes. The middle and bottom image exclude the beam tubes such that the temperature variation across the shield and frame is visible. The middle image again corresponds to a 37.9 W coupler heat load, which shows a maximum temperature of 59 K on the coupler intercept.

[4]This heat flux value is cited for MLI surrounding an 80 K shield, but $(300^4 - 50^4)/(300^4 - 80^4) \approx 1$, so the same value is used for the 50 K thermal shield model.

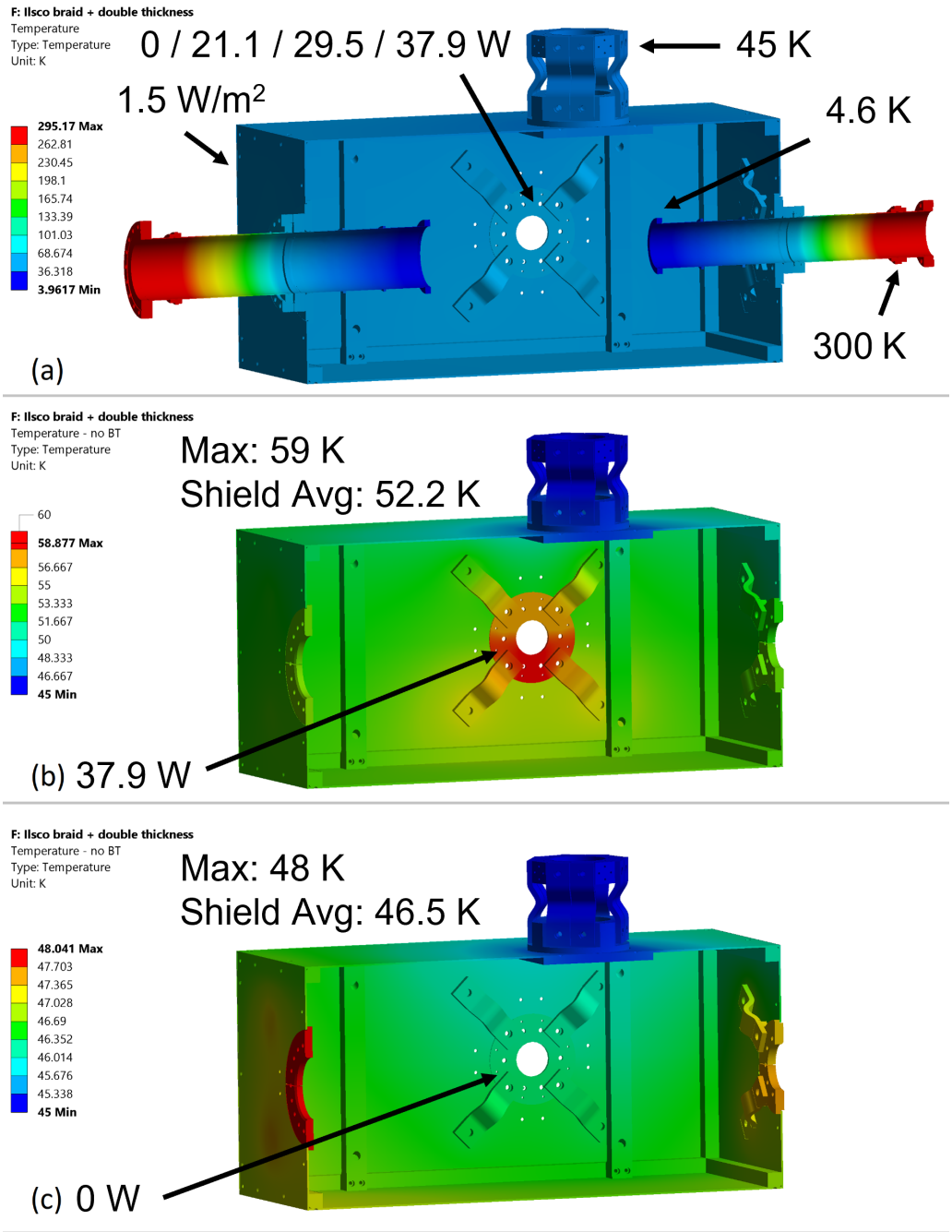

Figure 5.14: Thermal modeling results for the thermal shield and related thermal connections, including the aluminum frame, coupler heat intercepts and beam tubes from room temperature to 4 K (cavity not included). (a) Temperature results for the full model with thermal boundary conditions indicated. Not much detail is visible on the thermal shield due to the large temperature range on the beam tubes. (b) Temperature results excluding beam tubes for maximum coupler heat load (corresponding to 100 kW forward power each). (c) Temperature results excluding beam tubes corresponding to low-power testing without couplers installed.

The average temperature of the shield and frame, excluding the intercepts and cryocooler mounts, is 52.2 K. As seen in the image, the temperature across the shield is quite uniform, with most areas remaining within a couple K of the average. This confirms that this thermal shield design provides sufficiently even cooling to prevent any excessive hot spots from forming, even at the maximum power operation of the couplers.

The bottom image of Figure 5.14 corresponds to the case of low-power testing in which the couplers are not yet installed. As expected, the average temperature of the shield and frame is reduced to 46.5 K (assuming the cryocooler 1st stage is kept at 45 K via heaters). In addition, the maximum temperature of 48 K is now located on the beam tube intercept since the only heat load at the coupler intercept is thermal radiation.

5.4.3 Bellows & Transition Tubes

Besides the cavity itself, the beam tubes are comprised of bellows assemblies and transition tubes (one one each side of the cavity – see Figure 5.12). The bellows themselves are attached outside of the beam tube and thus are only exposed to the insulation vacuum rather than the cavity vacuum. The main purpose of the bellows is to allow for some flexibility during assembly and to accommodate thermal contraction of the cavity and beam line components during cooldown. Based on the lengths and materials of the beam line components ($\sim$ 0.4 m of niobium and $\sim$ 1 m of 316 stainless steel), about 3.6 mm of total contraction is expected. The small bellows can compress about 5 mm while the large bellows can compress about 14 mm, providing more than enough range for the expected thermal contraction.

Thin 316 stainless steel tubes are located between the thermal shield intercept and the cavity to act as a heat dam, reducing the amount of static heat leak that reaches the cavity. The walls of these tubes are only 0.5 mm thick, so stiffening rings had to be added to increase the rigidity. This helps to prevent buckling when the cavity is pumped down to vacuum as well as prevent any other mechanical failure during assembly. The same structural modeling is done as with the vacuum vessel stiffening ribs, though this case is much simpler as it only requires adding a couple stiffening rings equally spaced between the flanges of the tube. The resulting temperature profile of these transition tubes can be seen in the bottom image of Figure 5.4. This modeling showed that the static heat load at 4.2 K was only 0.22 W. This is a lower static heat load than the later tests conducted in the proof-of-principle study, even though the cavity now has a direct connection to room temperature along the beam tubes. This confirms that the thin-walled transition pieces are effective as a heat dam.

5.4.4 Support Structures

Supporting the cold components inside the cryomodule involves a balance of structural and thermal considerations. Simply put, increasing the strength of a structure for a given material often involves increasing the cross-section, but this will increase the amount of heat reaching the cold mass. Thus it is necessary to use materials which provide the strength needed to support the components in the cryomodule while having a low thermal conductivity to mitigate static heat leak from room temperature. One such material is G10, which is a composite of fiberglass layers and epoxy which are compressed under high pressure and heat [Ass98]. With a tensile strength comparable to that of 304 stainless steel [Mat24] but with

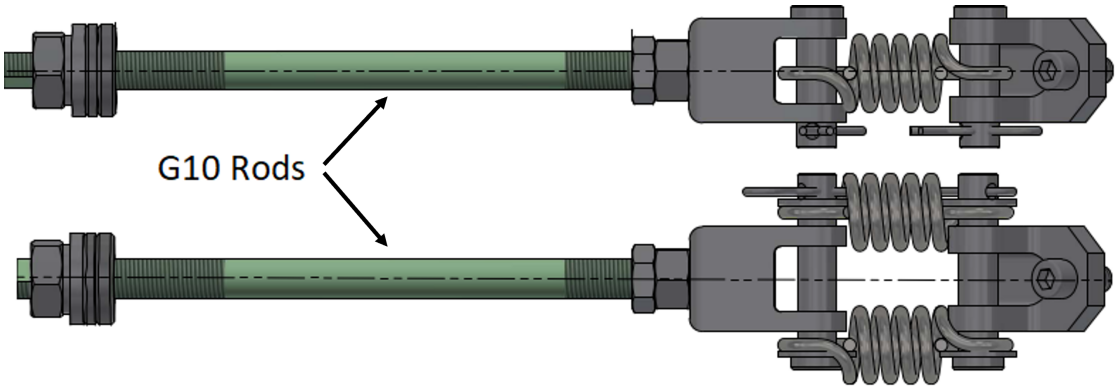

Figure 5.15: Examples of the final support rod design used in the cryomodule; the G10 component is visible in green.

roughly 20x less heat transfer [Baz21], G10 is an ideal material to use for support structures in cryogenic settings.

The new cryomodule uses a set of eight G10 rods with clevises and springs at the ends to suspend the aluminum frame from the vacuum vessel and another set of eight to suspend the cavity and beam tubes from the aluminum frame. Examples of the full support rod design can be seen in Figure 5.15. The springs between the rods and the supported structure offer flexibility for alignment during assembly as well as accommodation for thermal contraction during system cooldowns. The lower design shown in the figure has two springs per support rod as these are used to support the weight of the aluminum frame and everything mounted to or supported from it, thus a greater tension limit is needed compared to the other rods.

5.4.5 Sensors & Instrumentation

A variety of sensors and instrumentation will be used to monitor and control parts of the cryomodule during operation. A total of 16 Cernox sensors will be used for

temperature monitoring both during cooldown and RF testing:

- 8 CU-type sensors on the top and bottom of the cavity rings (2 per ring)
- 2 CU-type sensors on the cavity beam tube flanges
- 4 CD-type sensors on the cryocooler stages (1 per stage per cryocooler)
- 1 SD-type sensor on the antenna feedthrough
- 1 SD-type sensor on the bottom thermal shield panel

Note that this arrangement of sensors is designed for the initial low-power testing of the cryomodule. Once the couplers are installed, more sensors would be required to monitor various temperatures on the couplers as well. Two flux gates are mounted near the cavity equator using a G10 holder. One is oriented vertically (parallel to the larger component of Earth's magnetic field in the testing location) and one is oriented parallel to the cavity axis.

Heaters are located throughout the assembly in order to apply additional heat loads to the system both for temperature cycling and controlling the cryocooler temperatures during RF operation. There are a total of six heater circuits on the 4.2 K assembly – one per cavity ring and one per cryocooler 2nd stage. These heaters use 25 W resistors and are used primarily for precise control of thermal gradients during temperature cycles, as described in the previous chapter. They also provide the ability to calibrate the cryocooler 2nd stage temperatures to the applied heat load. This allows any issues with the thermal link to be diagnosed by warming up each cavity ring individually and recording the resulting temperatures at each end.

External instrumentation for the cryomodule includes: roughing and turbo pump for the insulation vacuum; let-up nozzle for bringing the system back to

atmosphere; convectron and cold cathode gauges for pressure monitoring; forward and transmitted power cables; helium gas reservoirs and motor units for the cryocoolers. The turbo pump and cryocooler parts can be seen on top of the cryomodule in Figure 5.12.

5.5 System Heat Loads

Another key result of the thermal modeling described in the previous sections is determining the heat loads at the two stages of the cryocoolers. This is done by adding a heat reaction result in the model which automatically calculates the amount of heat flow required to maintain a fixed temperature boundary condition. Thus, with the cryocooler stages represented by fixed temperatures of 45 K and 4.2 K, the heat reaction results correspond to the heat load at each stage. This was included in the thermal modeling of the cavity, couplers and thermal shield, though the thermal shield modeling only included the result for the 1st stage at 45 K.

The resulting heat loads are listed in Table 5.4[5], along with added contributions from the G10 support rods and thermal radiation. The heat loads listed for the couplers correspond to 50 and 100 kW operation per coupler. These individual contributions are summed together in the "All Sources" row, which shows (at maximum coupler operation) heat loads of 94.44 W on the 1st stage and 4.08 W on the 2nd stage. The next row lists the 1st stage heat load as found in the thermal shield modeling described in the previous section, which turned out to be 93.20 W

[5]The 4.2 K heat load for all Cernox sensors was calculated to be about 5 mW, while the flux gate wiring would contribute even less. These values were decided to be small enough compared to the other contributions to exclude from the main table.

Heat Loads (W)		
Source	1st Stage	2nd Stage
Cavity + Beam Tubes	13.30	1.74
Coupler*	29.50 / 37.90	0.80 / 1.11
G10 Support Rods	0.34	0.02
Thermal Radiation (est.)	5.00	0.10
All Sources (incl. 2x coupler)	77.64 / **94.44**	3.46 / **4.08**
Thermal Shield Model	76.40 / **93.20**	
Cryocooler Limits	**110**	**4.15**

* Coupler heat loads are for 50 kW / 100 kW operation.

Table 5.4: Total Heat Loads in the Cryomodule

at full coupler power. This agrees very well with the summation of the individual contributions. Given the combined cryocooler limits of 110 and 4.15 W at the 1st and 2nd stages, respectively, these results confirm that the full cryomodule can operate as designed within the cooling capacity available.

5.6 Summary

After a successful proof-of-principle study, efforts began to design a new standalone SRF cryomodule cooled with only commercial cryocoolers. Meant for small-scale applications, the operating goals of this system are to deliver 100 kW power to a 100 mA beam in order to provide an energy gain of 1 MeV. Designing such a system to operate with conduction cooling posed many challenges, particularly with designing a new SRF cavity and high-power coupler. Several considerations regarding RF, thermal and mechanical behavior had to be taken into account to ensure these components would meet the operational requirements.

Primary requirements which guided the cavity design included the need to

operate at 10 MV/m for the intended energy gain, maintaining a high Q_0 for low dissipation, and the ability to carry high beam current without excessive losses. Based on these conditions, a modified single-cell version of the injector cavities from Cornell's ERL was designed. Once this was completed, a new thermal link connecting the cavity to the cryocooler 2nd stages was needed. This design required a direct connection at the cavity equator for improved RF heat load extraction, effective mitigation of thermal gradients across the cavity during cooldown, and sufficient connections to maintain an operating temperature near 4.2 K. Primary design choices to satisfy these requirements included the use of four niobium rings welded near the equator and irises, high-purity (5N) aluminum rings which would be bolted to the niobium rings, and twelve high-purity copper thermal straps to connect the 5N aluminum rings to 5N aluminum mounting plates attached to the cryocoolers. Thermal modeling of this design proved that all of the requirements were satisfied, and the performance was significantly improved from the design used in the proof-of-principle study.

Designing a high-power coupler capable of operating within the cooling limitations of the cryocooler posed an even greater challenge. Based on the operational goals of the system, the injector couplers from Cornell's ERL were again used as a starting point for the new design. However, significant changes had to be made for the new couplers, such as enabling up to 100 kW forward power with only 1 W heat load at 4.2 K, replacing all fluid cryogenic cooling with conduction cooling, and reducing the cost by simplifying the overall design. Key components for solving the first challenge included the addition of quarter-wave transformers to the inner bellows to minimize reflections and the addition of an RF shield which acts to absorb most of the RF losses and extract the resulting heat at a higher temperature. The remaining challenges were primarily addressed by using large copper

disks as thermal connection points, removing the cold RF window such that only one warm window is used and removing one set of outer bellows. RF simulations and thermal modeling confirmed that the new design only had a 1.1 W heat load at 4.2 K, satisfying the main design requirement for the new coupler.

The design of other notable cryomodule components was discussed, such as the vacuum vessel and thermal shield. Several iterations of mechanical modeling were used to optimize the design and layout of stiffening ribs added to the vacuum vessel to better protect it from buckling when the system is pumped under vacuum. Thermal modeling was performed for the thermal shield and connected components to better understand what temperatures are expected on the shield for different cryomodule testing conditions. Finally, heat loads at the two cryocooler stages calculated in the various thermal modeling were compared to the total limits of the two cryocoolers used for the new system. It was shown that the combined heat loads are indeed just within the limits set by the cryocoolers, indicating that the cryomodule design was fully successful and is able to meet the operational goals while only being cooled by the two cryocoolers.

CHAPTER 6

CAVITY COMMISSIONING

Following the successful design of the new conduction-cooled cryomodule described in Chapter 5, the next step was to begin commissioning the system starting with the SRF cavity, LCC1-1. Commissioning the first cavity of a new design is no simple task and can take a considerable amount of time, as will be evident throughout this chapter. The first step of the process is fabrication, involving machining the raw material into the final component shapes and then electron-beam welding them together to form the final completed cavity; this portion of the commissioning is discussed in the first section of this chapter. Figure 6.1 shows the first page of the system's technical drawing sheets used for machining, which features LCC1-1 with some key dimensions labeled. The following section covers the niobium baseline vertical test and the cavity treatments and preparations leading up to it. The next section details the Nb_3Sn coating run for LCC1-1 as well as the vertical test that followed. Overall the cavity commissioning proved to be successful, demonstrating sufficient RF performance for initial testing of the full cryomodule later on.

6.1 Fabrication

The fabrication process for LCC1-1 followed the same general process described in Chapter 2. Most of the cavity is made out of 3 mm thick high-RRR niobium (typically RRR $\approx$ 300), either formed from tubes or sheets which are pressed into their final shape using pairs of dies. The main cavity half-cells and large beam tube stub piece (transition from 78 to 106 mm ID) are made from 1/8 inch thick high-RRR sheet. Different thicknesses were used based on what material was

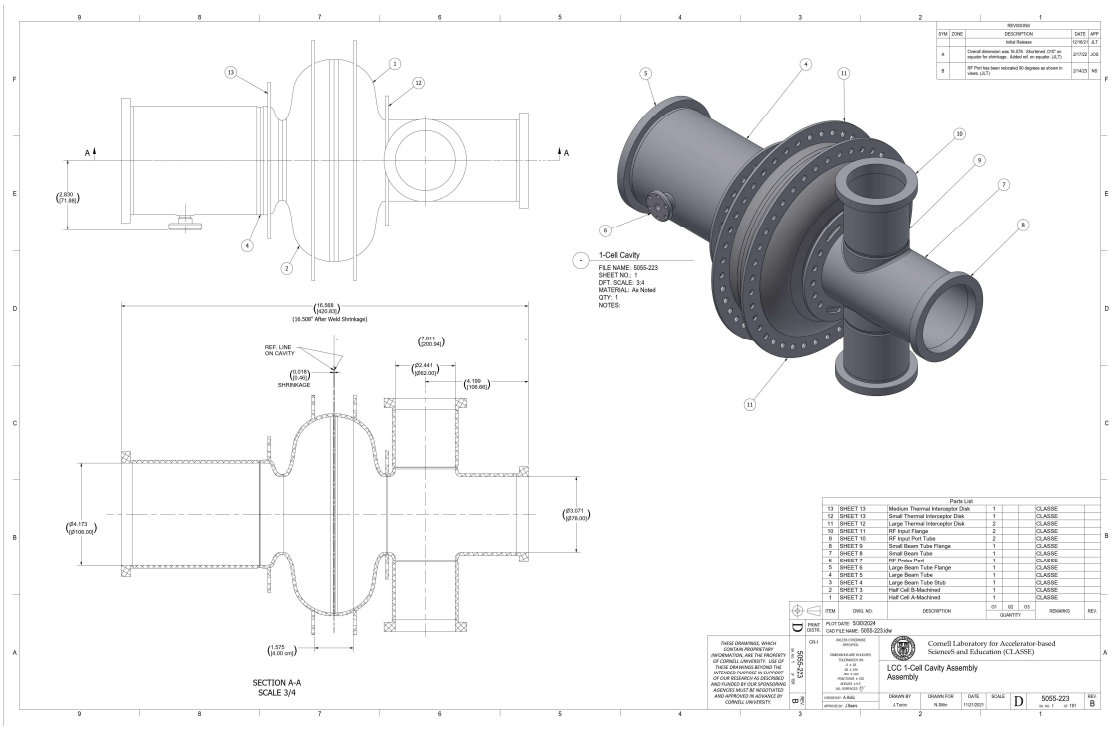

Figure 6.1: First page of the technical drawing sheets for the conduction-cooled cryomdodule project. A print of the LCC1-1 CAD model is seen on the right, while 2D drawings with various dimensions called out are on the left.

already available in the lab's supply. The four cavity flanges and pickup probe port are made of reactor grade niobium (reducing cost), while the heat intercept rings are also 3 mm thick high-RRR niobium. All material required for fabrication of LCC1-1 was acquired at the start of 2022.

Although the design was based on the Cornell ERL injector cavities, the modifications which were made required new planning for fabrication, particularly for the stub pulls on the large and small beam tubes and the welding sequence. Stub pulling dies had to be modified for use with 3 mm thick tubes, and a stub punch piece was used in place of a puller for the RF probe. This was done due to there being issues with the small pulling plug breaking when used. Figure 6.2 shows drawings of the two dies which were made, along with the punch and pull tools used. Representations of the beam tubes are also included. It is noteworthy that

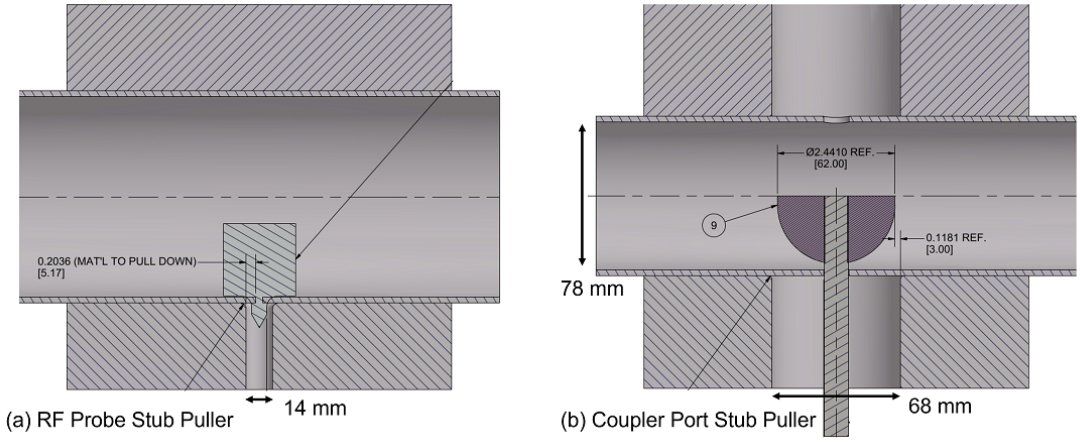

Figure 6.2: Drawings of the stub puller dies used for (a) the RF probe port on the large beam tube and (b) the coupler ports on the small beam tube. As indicated in the figure, the diameter of the pulled coupler port stubs is nearly as large as the small beam tube diameter itself, making this a particularly challenging task.

the diameter of the pulled coupler port is a significant portion of the small beam tube diameter. This creates a difficult pull to complete without damaging the material, and for this reason multiple practice pulls were done on spare tubing first. With the added planning and test parts involved, machining of the cavity parts lasted approximately from March to June of 2022.

Figure 6.3 shows the final welding sequence for LCC1-1; a more detailed outline of each step can be found in the Appendix. The order of welds needed particular attention due to components such as the large beam tube adapter and coupler ports, as these provided extra challenges in ensuring line-of-sight clearance for the beam welder. In addition, newly optimized beam parameters had to be determined for many of the welds. Some considerations include how much beam penetration is desired and at what angle the beam will hit the target area. The first picture of Figure 6.4 shows an example of a failed weld in which the parameters were not chosen correctly; the next picture shows the same weld done successfully. The remaining pictures in the figure show other examples of the welding process along

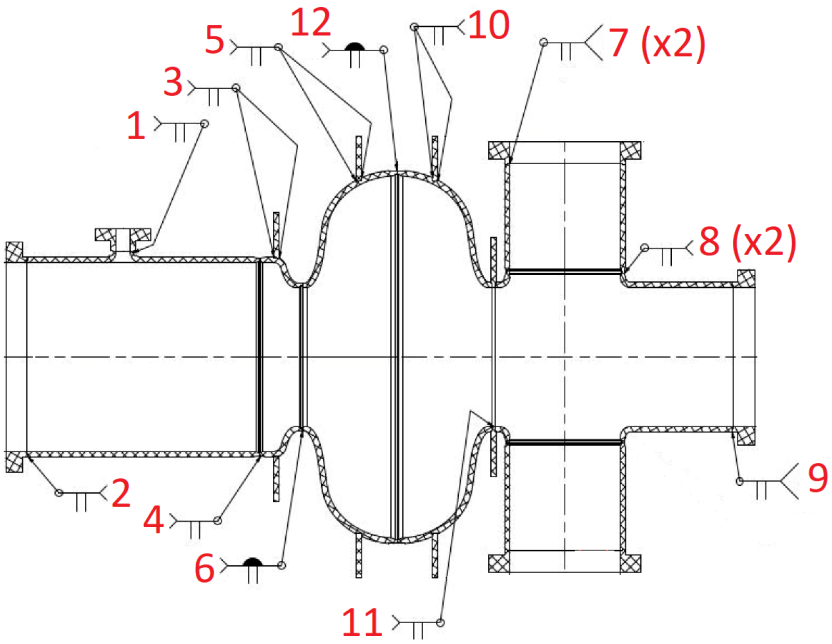

Figure 6.3: Designed sequence of electron-beam welding for LCC1-1.

with the completed cavity. The steering coil of the electron beam gun is visible at the top of images (c), (d), (e) and (g). In total, the welding process lasted from July 2022 to February 2023.

6.2 Baseline Preparation and Testing

After completion of the e-beam welding, the cavity was ready to begin chemical treatment in preparation for a baseline (pure niobium) vertical test in a helium bath. The main goal of the treatment was to provide a good substrate surface for the eventual Nb_3Sn coating, with the vertical test providing a confirmation whether this was achieved. Therefore a basic treatment procedure was planned: (i) bulk buffered chemical polish (BCP) and electro-polish (EP) for a total of 120 µm (roughly 70 + 50) based on the amount of removal used for the original ERL injector 2-cells [G+07], (ii) vacuum furnace bake at 800 C for 3-5 hours, (iii)

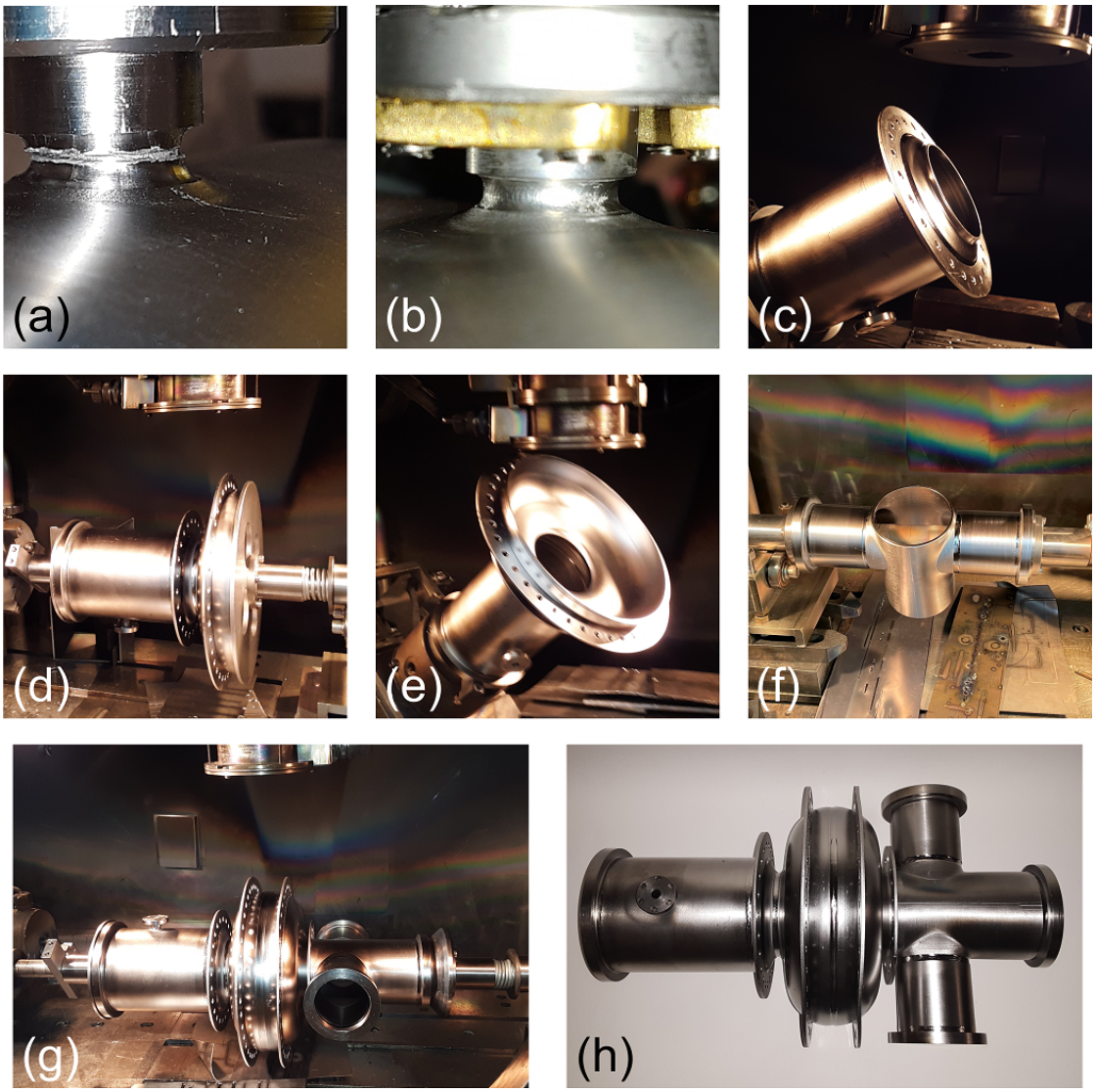

Figure 6.4: Various stages of the e-beam welding process of LCC1-1: (a) failed weld of the RF probe port (step 1) due to incorrect beam parameters, (b) successful weld of the probe port (image taken during later assembly), (c) weld step 4, (d) weld step 6 (outside), (e) weld step 6 (inside), (f) weld step 8, (g) weld step 12, (h) e-beam welding completed.

final EP of ~ 5 µm following the bake to remove any contaminants. A high-pressure rinse (HPR) with DI water would be performed in the cleanroom between the bulk EP and furnace run to ensure there is no residual acid or other contaminants left in the cavity during the heat treatment, as these could get baked into the RF surface and degrade the cavity performance.

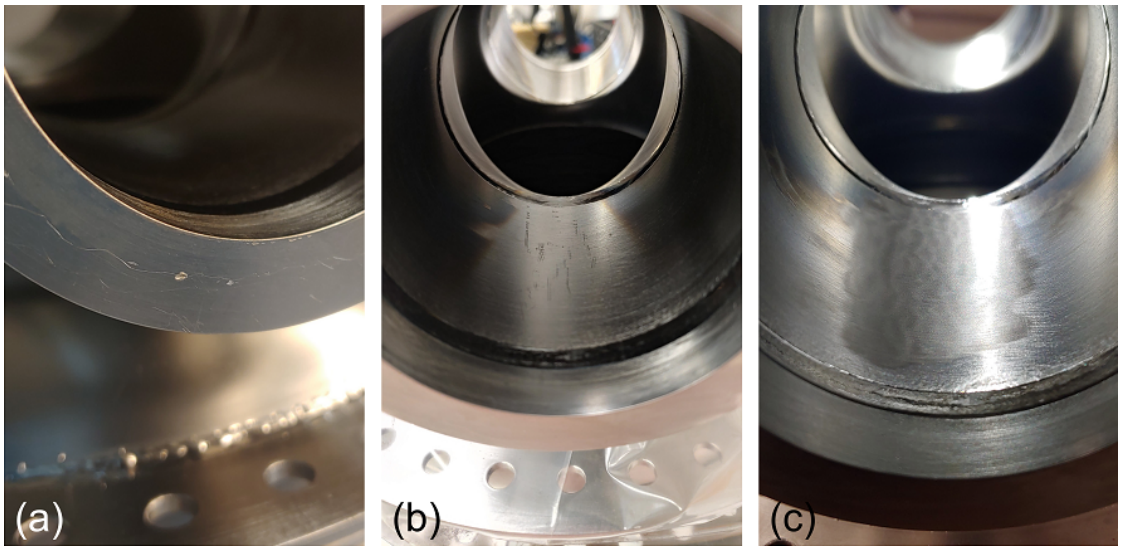

Figure 6.5: Mechanical polishing of marks seen on the cavity prior to chemical treatment: (a) small gouges on the sealing surface of a flange, (b) marks inside the coupler port, (c) coupler port after mechanical polishing.

However, an inspection of the cavity revealed that there were scratches in the coupler ports and small gouges on some of the cavity flanges which had to be removed before the main chemical treatment began. Examples of these marks can be seen in Figure 6.5. The exact source is unclear, though the marks may have been caused by mishandling during machining, fixturing used during e-beam welding or by mishandling afterwards. In any case, the marks were mechanically removed using a 3M Very Fine (VF) polishing wheel attached to a drill motor. To prevent contamination, the polishing wheels which were used were either new or only used on niobium parts previously. Figure 6.5 also shows an example of one of the coupler ports after being polished with this method, resulting in successful removal of the marks.

6.2.1 Chemical & Heat Treatment

Following the successful mechanical polishing, the planned cavity treatment began in May 2023; Figure 6.6 shows the setups used for the different treatments. First, the polished flanges were given a quick soak in a small tub of BCP solution (not included in figure); this had to be done separately since the flanges are sealed during the main BCP to prevent acid from leaking out of the cavity. Afterwards the bulk BCP was performed. Though a 70 µm removal was originally planned, a mistake in measurement of the etching sample resulted in a removal of just 45 µm. To compensate for this, the bulk EP had to be increased to ~ 80 µm total (40 µm per side). While this is not an issue as far as the cavity is concerned – in fact a larger bulk EP typically results in a smoother surface – it does lead to a longer process since EP removal is much slower than that of BCP. After the EP and subsequent HPR run were completed, the cavity was transferred to the vacuum furnace for the 800 C bake. Unfortunately, as the furnace temperature was ramping up there was some malfunction in the furnace operation that could have negatively affected the cavity if the run proceeded; thus the run was terminated and the system was allowed to cool back down naturally. After a two month delay waiting for repairs, the cavity was successfully baked at 800 C for 5 hours in July 2023. Finally, a short EP (6 µm total) completed LCC1-1's chemical and heat treatments.

The results of the three stages of chemical etching are shown in Figure 6.7; from left to right is the bulk BCP, bulk EP and final (short) EP. As expected, the surface looks especially smooth after the EP cycles. One irregularity is the presence of defects visible near the cavity iris on the small beam tube side, which first showed up after the bulk EP. The inset image in Figure 6.7(b) shows these in greater detail (the yellow hue is a reflection of the cleanroom camera). Noticing

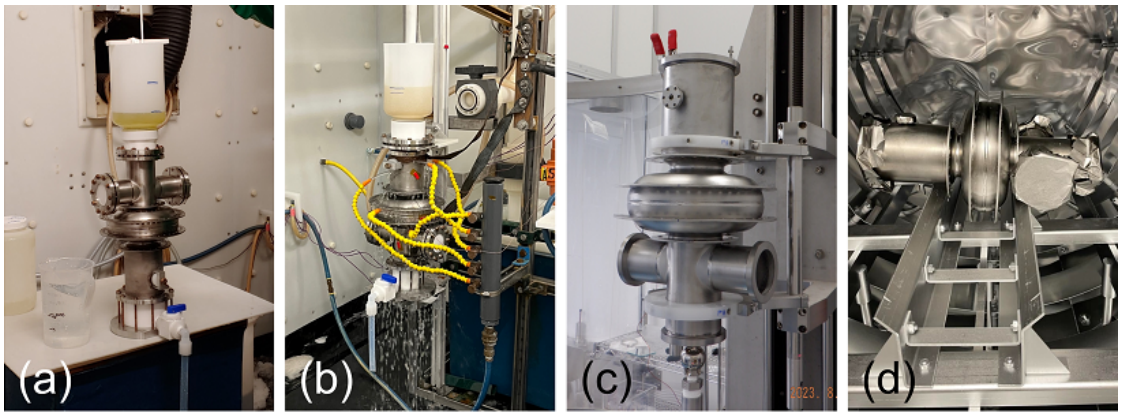

Figure 6.6: Setups for the chemical and heat treatments performed on LCCC1-1: (a) buffered chemical polish (BCP), (b) electro-polish (EP), (c) high-pressure rinse (HPR), (d) vacuum furnace bake.

that the defects are roughly aligned with the pickup probe port near the top of the image, it is clear that the defects were not present after the bulk BCP (see the same small port in the upper left of Figure 6.7(a)). The defects are still present after the final EP, as seen in Figure 6.7(c). It is still unclear whether the bulk EP directly produced these defects in some manner, or whether they were always present under the surface and were simply "uncovered" after enough material had been removed. Unfortunately, due to one of the heat intercept rings being welded very close to that iris (see e.g. Figure 6.4(h)), it is very difficult to properly mount a temperature sensor in that location to try to monitor any local heating during RF testing.

6.2.2 Test Preparation

After the final EP was completed, the cavity was transferred to the cleanroom for final preparation for the first baseline RF test. The first HPR run was completed with the cavity open, as shown in Figure 6.6(c). Unfortunately, around this point in the process the AC system in the cleanroom malfunctioned, causing the tem-

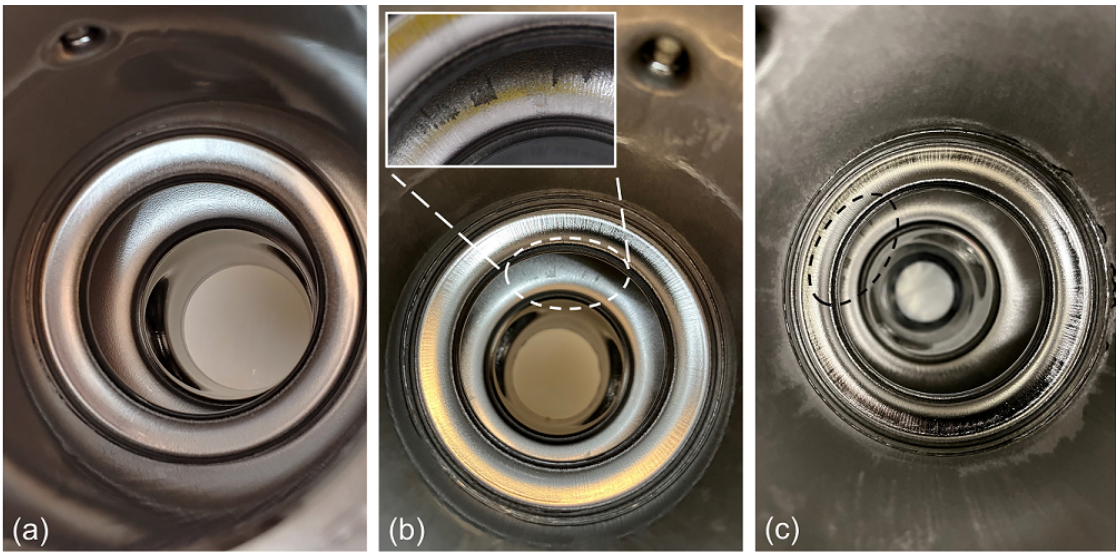

Figure 6.7: Surface finish results following the three main chemical treatments of LCC1-1: (a) bulk BCP, (b) bulk EP, (c) final EP. The surface defects first visible after the bulk EP are shown in greater detail in the inset image in (b).

perature to quickly increase from the typical mid-60 °F to above 90 °F. At these temperatures working in the cleanroom becomes a hazard, and considering how much of the assembly remained, it was decided to wait until the situation improved to continue. This led to another two month delay waiting for repairs to be completed. Afterwards it was decided to redo the first HPR run; thus two more HPR runs were completed at the start of October 2023, first with the cavity open then again with 316 stainless steel blanks added to the large beam tube and coupler ports via indium seals. The pickup probe port was left open to prevent water from possibly collecting on the copper antenna. After the HPRs were completed, the pickup probe was attached to the port and the whole cavity was attached to one of the test pit inserts; both connections similarly used indium seals.

With all seals complete, the cavity and insert were pumped down to vacuum using a pumping line in the cleanroom. Once a sufficiently low pressure was reached (low 10^{-7} Torr), a helium leak check was performed by spraying small amounts of

helium onto the seal flanges while monitoring the signal of a residual gas analyzer (RGA) on the pumping line. Once it was determined that all seals were leak tight, the insert was moved out of the cleanroom and into the main test pit area. A typical arrangement of sensors were added, namely three Cernox sensors (one at the equator and each iris) and two flux gates (one at the equator and top iris, both oriented vertically). Additional instrumentation included a helium level stick, a helium stinger used for adding helium to the pit dewar, and a heater circuit for warming up the cavity. Figure 6.8 shows the completed cavity and insert assembly fully prepared for RF testing in late October 2023.

Given that LCC1-1 is a new cavity, the appropriate length of forward power coupler (FPC) on the test insert had to be checked and a new pickup probe antenna had to be designed. First, the cavity RF model was extended from the small beam tube end (left side of Figure 5.1) and a model of a test insert FPC was added. Several RF simulations were run to calculate Q_{ext} of the FPC for different values of "IC_pen", which is the length that the inner conductor penetrates into the small beam tube of the cavity. Figure 6.9 shows an image of the model used in the simulation (the cavity extends to the right of what is shown) along with a plot of Q_{ext} vs IC_pen.

Added to the plot in green and orange are a set of calculated $Q_{\text{ext}-\text{FPC}}$ values which would be appropriate for the baseline niobium and Nb_3Sn vertical tests; this range of values can be used to determine the correct length for the forward power coupler. These values are calculated using three factors: (i) the expected cavity Q_0 in each test, (ii) a calculated $Q = 7.3 \times 10^{10}$ from the blanks on the large beam tube and coupler ports, and (iii) a targeted coupling factor ≈ 0.3 for all tests. As shown in the plot, all of the desired values for $Q_{\text{ext}-\text{FPC}}$ fall within a $\approx 1.5\,\text{inch}$

Figure 6.8: LCC1-1 fully assembled onto a test pit insert with sensors and instrumentation added. Cernox sensors are attached at the equator and each iris, while flux gates are mounted vertically at the equator and top iris.

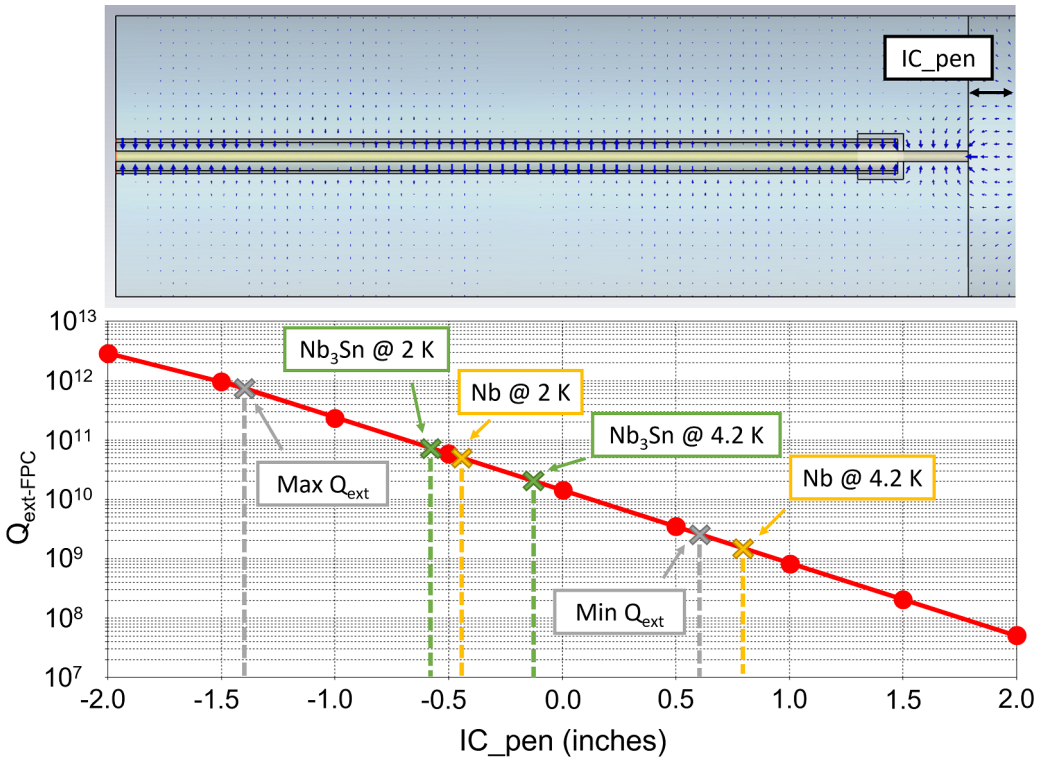

Figure 6.9: Above: Example electric field profile for the forward power coupler added to the cavity RF model, with the inner conductor ending where the cavity small beam tube begins. Below: Plot of the coupler Q_{ext} vs IC_pen (amount the inner conductor penetrates into the small beam tube). Orange and green marks indicate appropriate Q_{ext} values for the indicated vertical tests. Grey marks indicate the Q_{ext} range of the coupler which was chosen.

range of IC_pen, which is within the roughly 2 inch variation that can be achieved on the test inserts[1]. While a new pair of inner and outer conductor could have been machined to precisely fit the desired range, there was already a set available which provided a very close match – the range provided is indicated by the grey marks added to the plot. Since the niobium test at 4.2 K is not the most critical, it was deemed acceptable to use lower coupling (higher Q_{ext}) than the ideal value.

The probe antenna was also designed using the same cavity RF model, and

[1]The test pit inserts at Newman Lab have a bellows below the cavity location and a stepper motor which connects to the cavity top plate and support structure. This allows the cavity to be moved up and down while the forward power coupler stays fixed, thus changing $Q_{\text{ext}-\text{FPC}}$ (and by extension, the coupling factor).

can be seen in the right side of Figure 5.1. Determining the appropriate antenna length was simpler due to the probe having fixed coupling with a single targeted $Q_{\text{ext}-\text{probe}} \sim 10^{13}$. A high Q_{ext} is desired such that the probe does not contribute noticeably to the behavior of the cavity during RF testing.

6.2.3 RF Testing & Results

After inserting LCC1-1 into one of the Newman Lab test pits and pumping down the pit dewar, helium was added to the dewar for a basic fast cooldown: the cavity temperature reached 4.2 K in about 40 minutes. At the superconducting transition, the ambient magnetic fields were about 15 mG at the top iris and 5 mG at the cavity equator. The 15 mG in particular is higher than expected, though this is not as much of a concern for pure niobium performance, as discussed in Chapter 2. A short low-field RF test was conducted at 4.2 K, primarily to make sure all the testing hardware and software were set up properly before pumping on the helium to reach 2 K. The low-field Q_0 in the 4.2 K test was measured to be $\sim 3 \times 10^8$, which is quite typical for a pure niobium cavity without any special treatments such as a "low-T" (120 C) bake [PKH08, Man20]. The data from this test can be seen in Figure 6.10.

After decreasing the cavity temperature to 2 K, another RF test was performed. A low-field Q_0 of about 1 - 1.5 $\times 10^{10}$ was measured, which is again a typical value for pure niobium [PKH08, Man20]. As the field magnitude was increased, signs of multipacting were unexpectedly seen starting around 6 MV/m. Increasing the forward power allowed the cavity to "skip" a first band of multipacting and reach a stable state (no processing) at 8 MV/m. More multipacting was present between roughly 8.5-9.5 MV/m. Two examples of data acquisition points are shown

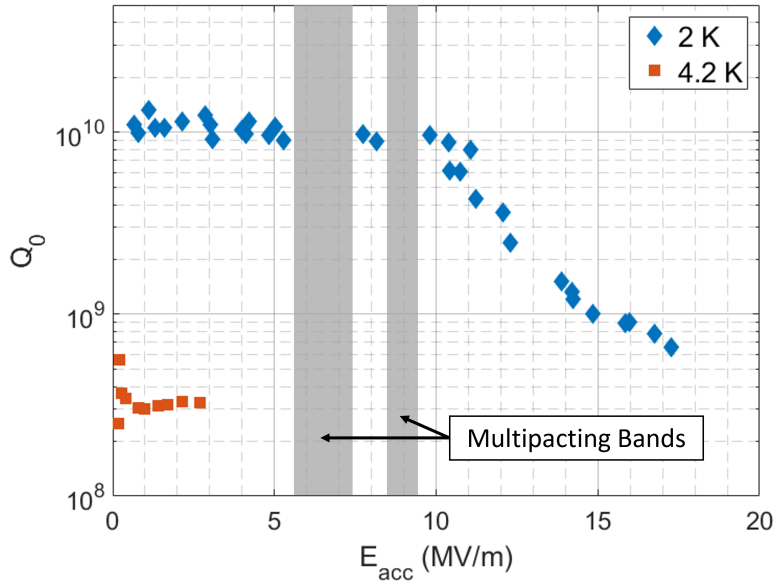

Figure 6.10: Plot of cavity quality factor vs accelerating gradient at both 2 K and 4.2 K. The low-field 4.2 K test was used to make sure the system was set up properly before moving on to the 2 K test. Two multipacting bands were seen between $\sim$ 6 - 10 MV/m, as indicated by the grey bands. An error of 10% is assumed for both Q_0 and E_{acc} (see Chapter 2).

in Figure 6.11; the example on the left shows the effects of multipacting in the continuous Q vs E curve (circled in orange), while the example on the right shows a "clean" curve without these effects. Beyond the multipacting bands, a strong Q-slope began around 10 MV/m. The cavity Q_0 steadily decreased as the accelerating gradient increased, ending around 7×10^8 at 17 MV/m. Radiation monitor readings indicated that field emission began around 10 MV/m and increased significantly up to the final field of 17 MV/m; this would contribute to the drop in measured Q_0 as more power was being absorbed by the field emitter. The test was stopped as the accelerating gradient was no longer increasing when more power was sent to the cavity. These results can also be seen in Figure 6.10.

After the test was completed, it was realized that multipacting between 3.5 - 8 MV/m had been previously reported during the commissioning of the original

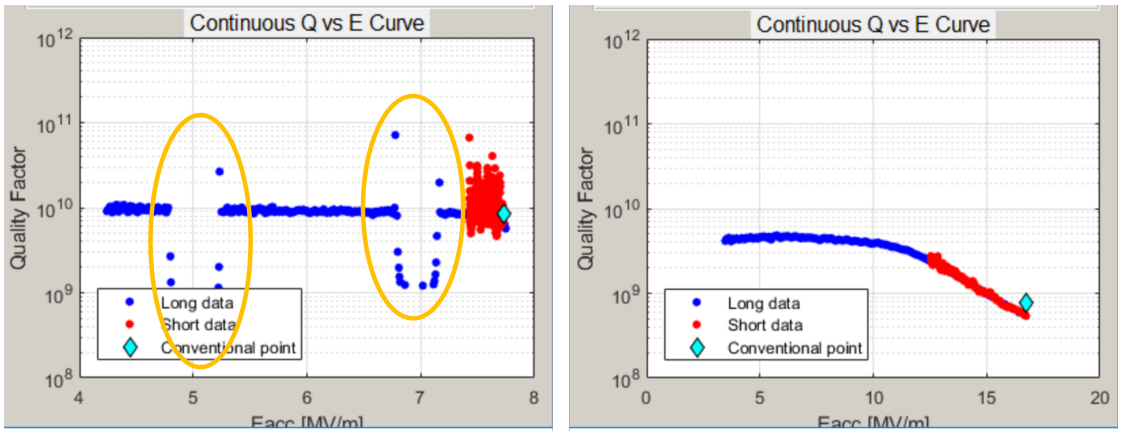

Figure 6.11: Examples of data acquisition via the RF testing software used by Cornell's SRF group. Left: acquisition showing the effects of multipacting in the continuous Q vs E curve (circled in orange). Right: "clean" data acquisition with no signs of multipacting.

ERL injector cavities [G+07]. This was also unexpected at the time[2], as multipacting simulations performed in MultiPac [YOP01] during the designing of the injector cavities had shown no signs of multipacting [SBG+03]. However, these original simulations only included the cavity cells but not the enlarged beam tube, which turns out to be where the multipacting occurs. Unfortunately, the original design paper (and other earlier reports or proceedings which did not have mention of multipacting) was used as the main reference for the design of LCC1-1.

Despite the detrimental effect of multipacting being present, the baseline niobium test was deemed overall successful. The cavity reached a field of 17 MV/m in the 2 K test, which is well above the final targeted operating field of 10 MV/m. In addition, the achievable accelerating gradient was likely limited by the measured field emission, which has the potential to be rectified by more careful cleanroom preparation. The results indicate that the niobium substrate is a good enough quality to proceed to the next stage of commissioning, which is coating LCC1-1 with Nb_3Sn to enable efficient cavity operation at 4.2 K.

[2] 2007

6.3 Nb_3Sn Coating and Testing

Following the baseline niobium test, the cavity was brought back into the cleanroom, let up to atmosphere with pure nitrogen, and disassembled. After disassembly, the cavity flanges received a light nitric acid etch to remove any remaining indium. The cavity was then moved back into the cleanroom and given an ultrasonic cleaning in pure DI water followed by an HPR run with all ports open. After the HPR run, the cavity was ready to be placed into the Nb_3Sn furnace to be coated, which will be discussed more below. With a new coating of Nb_3Sn, the cavity went through the same final test preparation procedure as described in the previous section: two HPR runs, assembly onto the test insert, pump down to vacuum, and attaching sensors and instrumentation after being removed from the cleanroom. The only difference was that the Nb_3Sn test required the use of a special slow-cool stinger used for much slower cooldowns, as described in Chapter 2. The same forward power coupler and pickup probe described in the previous section were used as well. All preparations for the Nb_3Sn vertical test were completed in February 2024.

6.3.1 Nb_3Sn Furnace Run

In planning the Nb_3Sn coating run for LCC1-1, there was concern that the heat intercept rings also being coated could negatively impact the conduction cooling performance (recall that the cavity remains open in Cornell's Nb_3Sn furnace setup). As mentioned in Chapter 2, although Nb_3Sn films tend to be 3 µm or less, the thermal conductivity is about 10^3 times worse than that of niobium at 4.2 K. Thus a 3 µm film of Nb_3Sn has similar heat transport properties to a 3 mm thick

niobium substrate. To check the severity of this effect, the resulting temperature gradient across the film can be estimated using

$$\Delta T = Q * L/(k * A), \tag{6.1}$$

where Q is the heat flow, L is the length, k is the thermal conductivity and A is the area. Estimated values are $Q = 0.75\,\mathrm{W}$ (1.5 W modeled heat load split between two equator rings); $L = 3 \times 10^{-6}\,\mathrm{m}$ (max film thickness); $k = 3 \times 10^{-2}\,\mathrm{W/(m * K)}$ (for Nb_3Sn at 4.2 K, see Figure 2.5); $A = 3\,\mathrm{mm} * 63\,\mathrm{cm} \approx 2 \times 10^{-3}\,\mathrm{m^2}$ (estimated width of heat transport band * inner circumference of equator rings). Plugging in these values results in an estimated thermal gradient of $\approx 40\,\mathrm{mK}$ across the Nb_3Sn coating on the equator rings. This was determined small enough to not be concerned, such that there was no need to use niobium foil or other methods to cover the rings during coating. Applying a heat flux probe to the cavity thermal model described in Chapter 5 indeed showed that the majority of the heat flowing through the equator rings is restricted to a narrow 3-5 mm band.

Figure 6.12 shows LCC1-1 in the bottom of the Nb_3Sn furnace, ready for the coating run to begin. Clean plastic bags (flipped inside out such that the clean surfaces faced outward) were used as buffers in the upper portion of the furnace with stainless steel walls. This was done to ensure the cavity did not come into contact with the walls and possibly pull stainless steel contaminant down into the main coating chamber. As seen in the image, LCC1-1 is nearly as wide as the furnace itself; in fact there is only about 0.2 inch clearance between the widest points on the cavity and the furnace walls. Combined with a larger weight (≈ 17 lbs) compared to standard TESLA single-cell cavities, cleanly lowering LCC1-1 into the furnace by hand was a challenging task in itself.

While the original plan for LCC1-1 was to receive a standard coating as de-

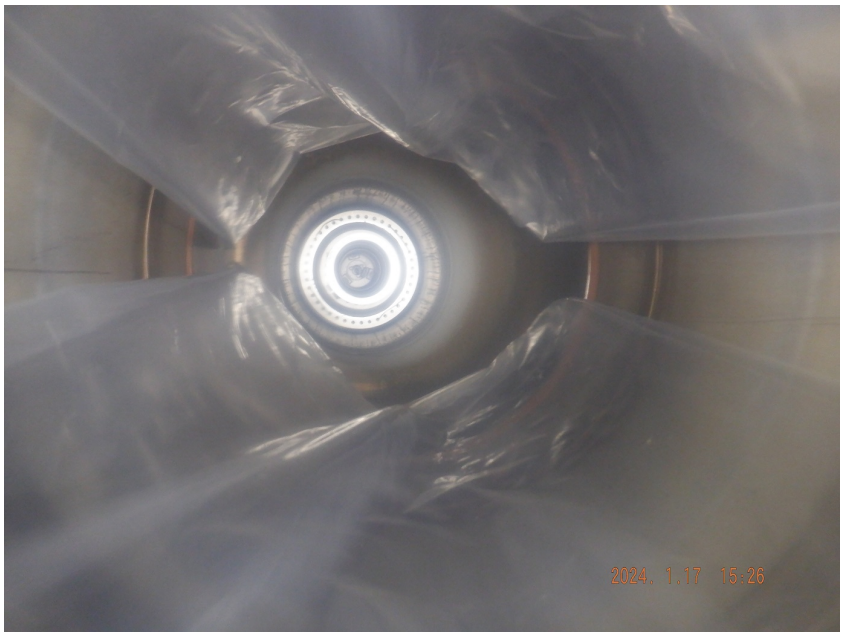

Figure 6.12: LCC1-1 placed in the bottom of the Nb_3Sn furnace. Visible at the top and bottom of the image are clean plastic bags used as buffers in the upper stainless steel portion of the furnace. These were added due to the large diameter of the cavity being only slightly smaller than that of the furnace.

scribed in Chapter 2, unfortunate circumstances prevented this from happening. After the typical 5 hours of nucleation at 550 C, the temperature ramp-up for the coating stage was started. However, rather than increasing, the temperatures actually began to decrease. The heater set points were returned to their nucleation stage values while troubleshooting began. It was discovered that the computer connection cable for the secondary heater was disconnected from the heater control box. To avoid possible electrical hazards, both primary and secondary heater set points were temporarily set to zero and the physical furnace control key turned off before reconnecting the secondary heater cable. However, pressing the "heater on" button on the furnace control panel after this caused the entire interlock chain to trip. This effectively triggered a cooldown of the cavity and chamber while control of the furnace could not be re-established due to the broken interlock. Following unsuccessful troubleshooting, the furnace was left overnight after confirming that

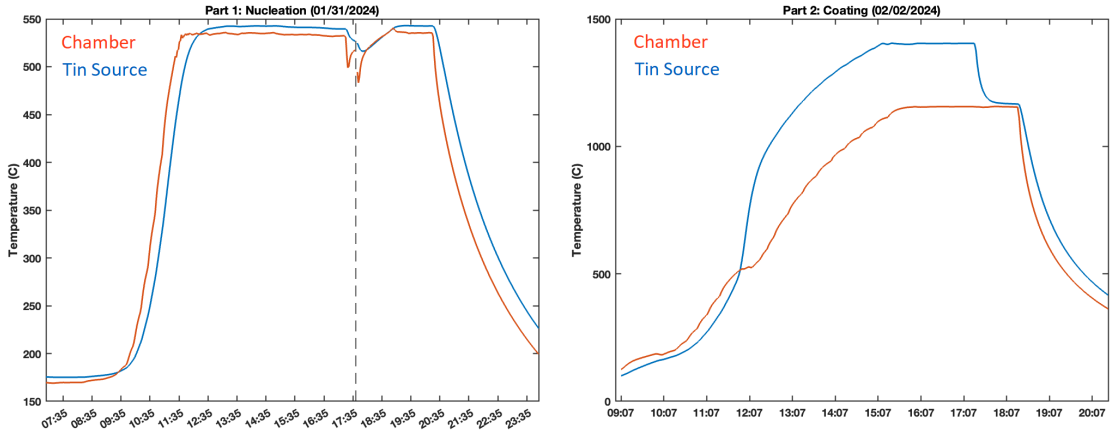

Figure 6.13: Nb_3Sn coating profile for LCC1-1. The longer nucleation duration was due to the secondary heater not being connected properly, while the break between the nucleation and coating stages was due to an accidental trip in the system interlock.

the system's state was stable[3].

The next day it was discovered that power cycling the DC power supply for the primary heater fixed the broken interlock. The secondary heater was tested and demonstrated normal functionality. With the situation rectified, the remainder of the coating process was performed the following day. This was done by immediately ramping the chamber temperature to 1150 C and the tin source temperature to 1400 C, as would normally be done directly following the nucleation stage. After holding these temperatures for 1.5 hrs of coating, the secondary heater was turned off for 1 hr of annealing. This completed the Nb_3Sn coating process for LCC1-1; the temperature profiles for the chamber and tin source are plotted in Figure 6.13.

Multiple images of the resulting Nb_3Sn coating are shown in Figure 6.14: (a) and (b) were taken with a regular camera immediately after the cavity was removed from the furnace, while (c) and (d) are scanning electron microscope (SEM) images with length scales 2 µm and 1 µm, respectively, of a witness sample which was hung

[3]Even if far from ideal.

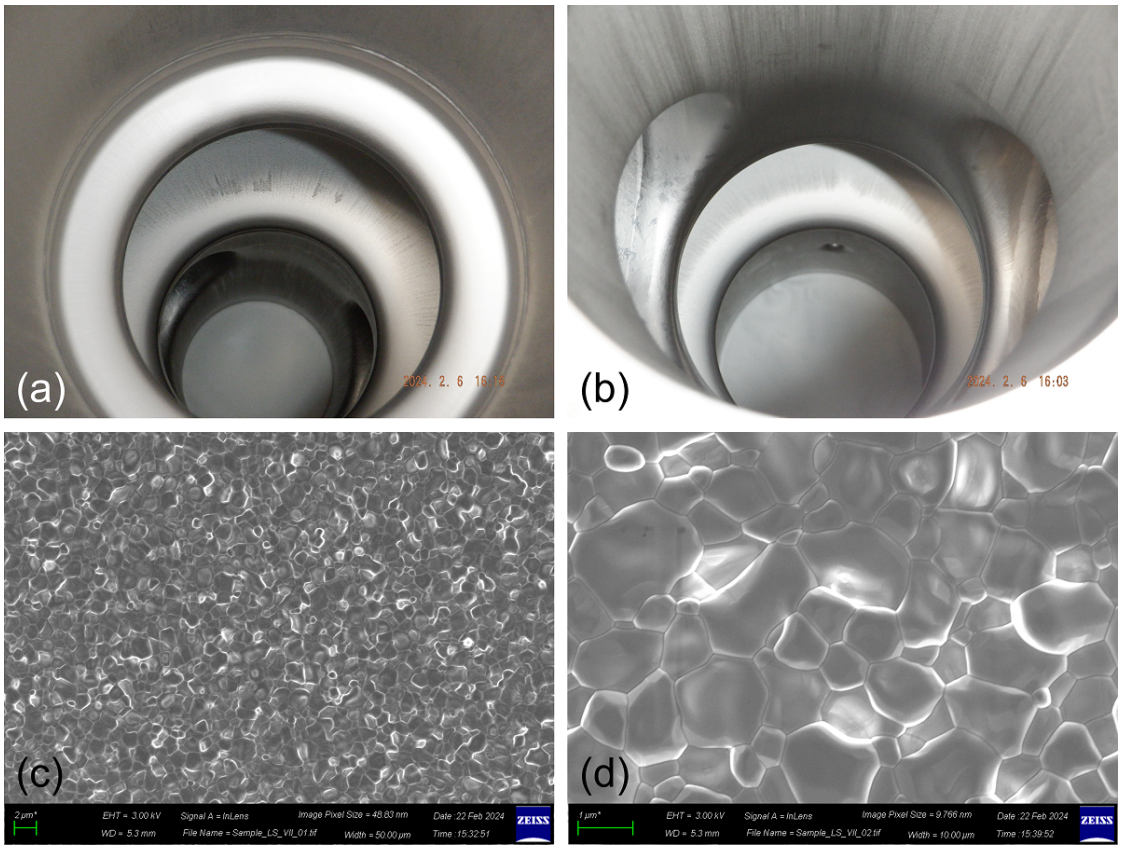

Figure 6.14: Nb_3Sn coating results for LCC1-1. Images (a) and (b) show pictures taken of the inner surface after coating, with the same defects on the cavity iris still visible. The coating otherwise appears similar to a standard coating result. Images (c) and (d) show SEM scans of the witness sample present during the coating, with length scales of 2 µm and 1 µm, respectively, indicated by the green bars in the bottom left.

above the cavity during the coating run. Overall, images (a) and (b) show a fairly uniform matte coating which is similar to those produced by the standard coating process. The defects at the cavity iris are still visible in the first image, though it was not expected that a ~ 3 µm coating would be enough to cover them. The SEM images show a generally uniform distribution of Nb_3Sn grains on the scale of ~ 1 µm which is typical of the standard coating process [Pos14, Hal17, Por21].

6.3.2 RF Testing & Results

With LCC1-1 moved into one of the test pits and pumped down, the slow-cool procedure was ready to begin. This process begins the same as a normal cooldown until the cavity has reached about 35 K. At that point, the heaters mounted inside the slow-cool stinger are turned on at maximum power and both the stinger and main helium dewar valve are left only slightly open. The dewar valve is adjusted so that the cavity temperature levels off between 20 - 25 K. Once this is achieved, a careful balance of adjusting the stinger heater power and dewar valve set point is performed to slowly cool the cavity through the superconducting transition at $T_c = 18$ K while maintaining a small temperature difference between the cavity irises. Previous studies found that targeting 200 mK/m or less is ideal for mitigating the effects of thermoelectric currents during cooldown [Hal17]. For a 1.3 GHz cavity, this corresponds to an iris-to-iris temperature difference of about 40 mK[4].

An example view of the temperature and magnetic field monitoring software used during cavity cooldowns is shown in Figure 6.15. The left plot shows the three sensor temperatures as the cavity cools through T_c. Note that channel 1 and channel 3 correspond to the top and bottom iris sensors, respectively. These two temperatures were kept within 60 mK or less during the cooldown for several K near T_c, achieving a small thermal gradient very close to the ideal value. The plot on the right shows the magnetic field measured at the top iris. There is a clear jump in the field at the 145 min mark, which matches precisely to when the cavity cooled down through 18 K – this provides a reliable confirmation of when

[4]Based on the cited study, the correct length is measured along the cavity wall rather than directly along the cavity axis. Thus for this calculation, the iris-to-iris distance for LCC1-1 is ≈ 20 cm rather than ≈ 10 cm.

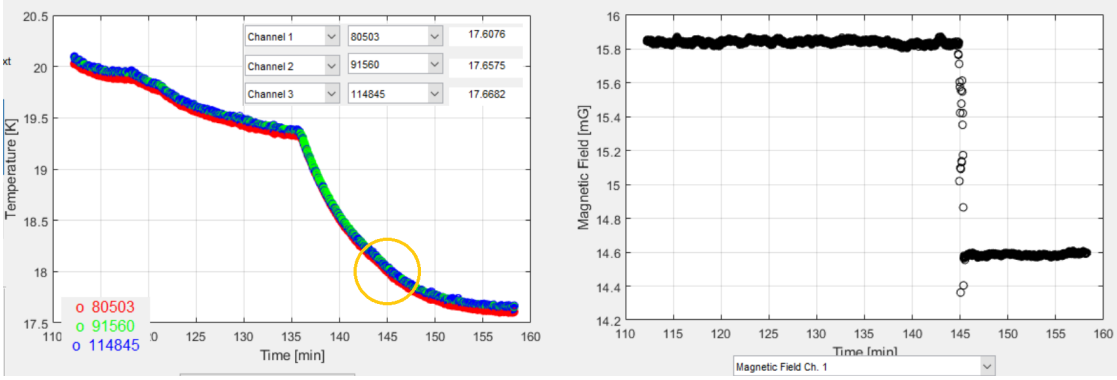

Figure 6.15: Cavity temperature and ambient magnetic field monitoring software used during cavity cooldowns, showing the superconducting transition in the Nb_3Sn test of LCC1-1. This cooldown was able to achieve very small thermal gradients, but the ambient magnetic fields were unusually high.

the superconducting transition occurred. Unfortunately, the ambient magnetic field reading was again quite high: about 16 mG for the top iris and 14 mG for the cavity equator (not shown). This high of ambient field is much more problematic for a Nb_3Sn cavity, which will trap most if not all magnetic flux present during the superconducting transition.

During the 4.2 K RF test, the same multipacting seen in the previous test was present once again. In this case, the multipacting was present between about 5.5 - 6.5 MV/m and around 7.5 MV/m. Multipacting can pose a larger challenge to Nb_3Sn cavities for a couple reasons. First, the secondary electron yield (SEY) is generally higher than that of niobium [AJNK15], increasing the chances of multipacting occurring. Second, processing through multipacting is riskier in Nb_3Sn cavities due to the significant detrimental effect that quenches have on the cavity quality factor. Often it is necessary to send relatively high power to the cavity to effectively process. This can progress very slowly, where the field level is throttled by the multipacting, before the cavity suddenly "breaks through" the multipacting band and the fields inside jump to a much higher magnitude. This sudden

increase in field level poses a significant risk of quenching the cavity depending on how much power was used for processing. Nevertheless, quenching a Nb_3Sn cavity is less of an issue during vertical testing, so all multipacting was successfully processed during the 4.2 K test. Fortunately, the benefits of processing often remain as long as the cavity is not warmed up above T_c, which proved true during the 2 K RF test when no multipacting was present (the cavity did not quench during the 4.2 K test).

Figure 6.16 shows a plot of the cavity quality factor vs accelerating gradient for the 4.2 K and 2 K Nb_3Sn RF tests. The 2 K results include both pre- and post-quench data, with the post-quench quality factor showing a noticeable drop as expected for a Nb_3Sn cavity. The low-field Q_0 is about 1×10^{10} in the 4.2 K test and 2×10^{10} in the 2 K test. These are both lower than the current state-of-the-art at Cornell (2×10^{10} and 4-5 $\times 10^{10}$, respectively [Por21]), but not uncommon for a more "average" Nb_3Sn cavity performance. However, the 2 K test displays a strong Q-slope immediately while the 4.2 K test has a Q-slope starting near 4 MV/m. In both tests, the cavity Q_0 eventually drops below 1×10^9 before the cavity becomes power limited just under 8.5 MV/m (4.2 K test) or quenches just under 10 MV/m (2 K test). This is very different from well-performing cavities, where the Q_0 drops more slowly and remains at or above 1×10^{10} up to the (nearly doubled) quench field [Por21].

Figure 6.17 includes two plots of the cavity surface resistance vs peak surface magnetic field measured in both RF tests. Since the surface resistance is inversely proportional to Q_0, the basic resistance calculation tells a similar story: the low-field resistance in both tests is within a typical range, though on the higher side. There is a much stronger field dependence than usual, indicating a dominant

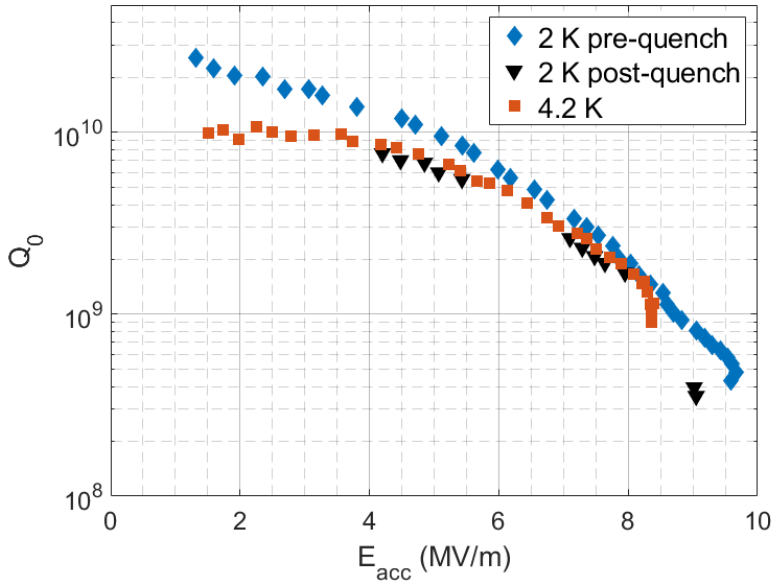

Figure 6.16: Plot of the cavity quality factor vs accelerating gradient for the 2 K and 4.2 K Nb_3Sn tests. The 2 K QvE data includes both pre- and post-quench. An error of 10% is assumed for both Q_0 and E_{acc} (see Chapter 2).

residual resistance component. This is confirmed by subtracting the surface resistance at 2 K from that at 4.2 K. This provides a "shortcut" estimation of R_{BCS} at 4.2 K since the surface resistance at 2 K can be treated as entirely residual: $R_{BCS}(2\,K) \approx 0.2\,p\Omega$ for stoichiometric Nb_3Sn. The result of this calculation is shown in the left plot of Figure 6.17; indeed the estimated R_{BCS} component is field-independent within the calculation error, such that the significant increase in the surface resistance at higher fields is primarily residual. This also indicates that at low fields, the surface resistance at 4.2 K is approximately evenly split between BCS and residual, with each contributing about 10-15 nΩ. State-of-the-art cavities at Cornell have a 4.2 K R_{BCS} of 8-9 nΩ [Por21], indicating that the BCS contribution in the current coating is quite good, though still has room for improvement.

One of the most prevalent contributors to the residual resistance in Nb_3Sn

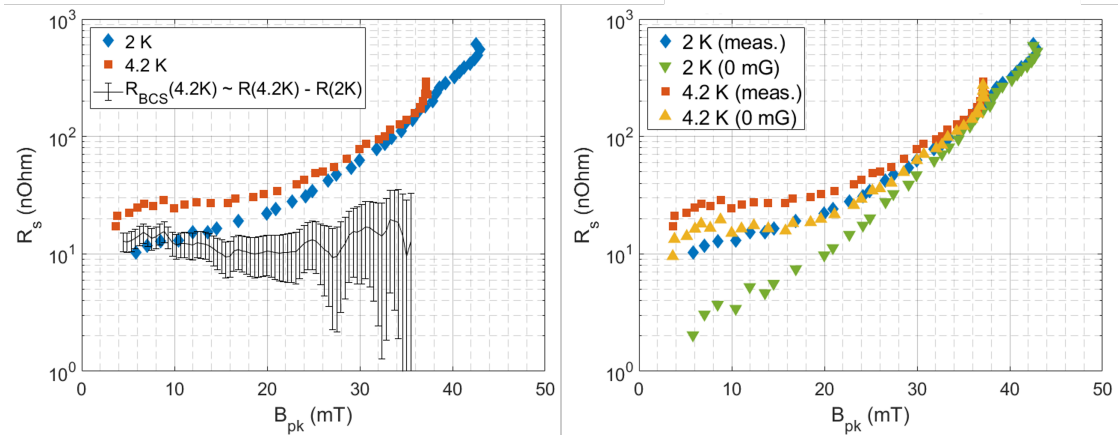

Figure 6.17: Plot of the cavity surface resistance vs peak surface magnetic field for the 2 K and 4.2 K Nb_3Sn tests. The left plot also includes an approximate calculation of $R_{\mathrm{BCS}}(4.2\,\mathrm{K})$ using the fact that $R_s(2\,\mathrm{K})$ is nearly entirely residual. The right plot includes predictions of the what the surface resistance would be if there were no ambient fields present during cooldown, based on an empirical model derived in [Hal17].

cavities is trapped magnetic flux. A previous study at Cornell investigated the sensitivity to trapped flux and empirically derived a formula to calculate this contribution:

$$\frac{\mathrm{d}R}{\mathrm{d}B_{\mathrm{trapped}}} = R^0_{\mathrm{flux}} + R^1_{\mathrm{flux}} B_{\mathrm{RF}} \tag{6.2}$$

where B_{RF} is the peak surface magnetic field in the cavity and $R^0_{\mathrm{flux}} = (0.47 \pm 0.02)$ nΩ/mG and $R^1_{\mathrm{flux}} = (0.021 \pm 0.001)$ nΩ/mG/mT for a 1.3 GHz cavity [Hal17][5]. Note that the field-dependent component of the contribution, while present, is quite small. The right plot of Figure 6.17 shows the result of subtracting off this estimated trapped flux contribution from the surface resistances measured in the RF tests, indicated by the "0 mG" curves. Recall that the ambient magnetic field at the cavity equator during the superconducting transition was about 14 mG.

While these results do show improvement in the projected low-field resistance, the effect diminishes at higher fields. For example, state-of-the-art Nb_3Sn cavities

[5]In these calculations, mG refers to trapped flux during cooldown, while mT refers to the magnetic field inside the cavity during RF operation.

at Cornell have a residual resistance of 7-8 nΩ at 10 MV/m ≈ 44 mT [Por21]; by comparison, the LCC1-1 tests show a 2 K resistance of several *hundred* nΩ at the same field (in this case, the quench field). This indicates a much larger factor contributing to excessive resistance at even moderate fields, with one possibility being poorly coated regions in the cavity. There are several ways in which a sub-optimal coating can contribute to degraded cavity performance, such as thin regions which don't fully mask the niobium substrate from the RF fields, tin-depleted regions with suppressed T_c, and higher surface roughness which can cause local field enhancement [Pos14, Hal17, Por21]. In addition, the visible surface defects near the cavity iris could be a source of increased heating and losses.

6.4 Summary

Successful commissioning of LCC1-1 was completed over the span of about two years; Figure 6.18 gives an overview of the commissioning progress during that time. The new design of the cavity posed extra challenges to the machining and welding process, leading to the cavity fabrication requiring about one year to finish. The niobium and Nb_3Sn vertical tests were completed over the following year, with various preparations leading up to each test described in this chapter. Overall, the cavity reached sufficient performance in both vertical tests to be used for initial testing in the full cryomodule. However, indications of high residual resistance in the Nb_3Sn test suggest that long-term operation of the system may require re-coating the cavity to obtain better RF performance.

While the surface defects present near the cavity iris on the small beam tube side (previously shown in Figures 6.7 and 6.14) have not been directly investigated

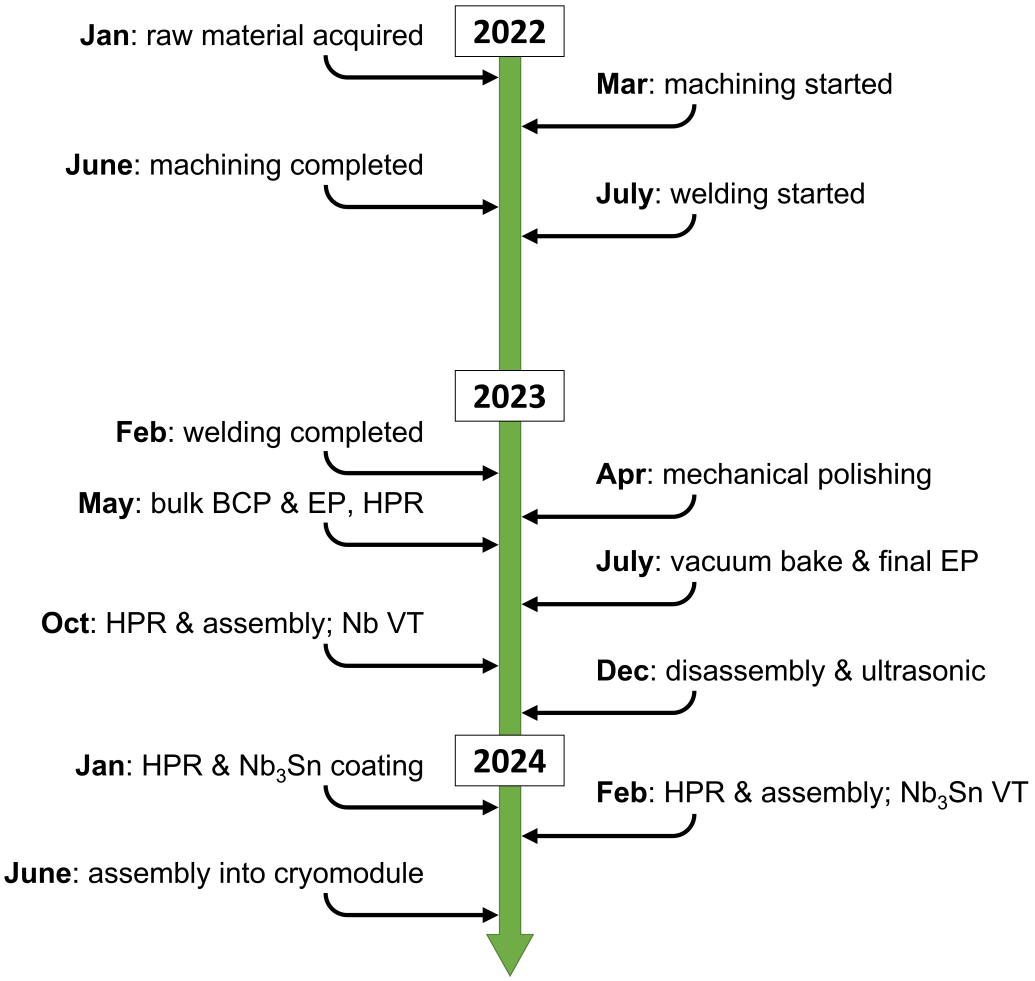

Figure 6.18: Summary of the commissioning timeline for LCC1-1.

or linked to worsened RF performance in LCC1-1, it is not unlikely that a future study could find this to be the case. If so, it may be worth determining the structure of these defects in more detail, for example using an optical inspection setup to examine the area up-close without needing to remove portions of the cavity. This could help assess whether these defects can be eliminated (relatively) simply by removing more surface material, either by physical methods such as tumbling or additional chemical etching.

In addition, more significant measures may need to be taken to address the issue of multipacting in the large beam tube transition region. After multipacting

was unexpectedly seen in the original ERL 2-cell injector cavities, the multipacting behavior in this region was re-investigated using MultiPac [YOP01]. The study found that increasing the bending radius at the transition to the larger beam tube could mitigate the presence of multipacting entirely [BS08]. Part of the issue is that a smaller bending radius creates a local minimum in the electric field, which is more conducive to multipacting. Increasing the radius makes the minimum much more shallow or eliminates it altogether. Thus, a more extensive change to LCC1-1 could be the removal of the current large beam tube transition piece, replacing it with a new piece with a larger bending radius, then re-welding the cavity together[6].

[6]It could be argued that this is a large enough change that the resulting cavity represents a new design and thus would require a new title: LCC1-2. Though this may be approaching Ship of Theseus territory, which is beyond the scope of this work.

CHAPTER 7

SUMMARY AND OUTLOOK

This dissertation has covered the beginning stages of compact SRF research conducted at Cornell. This work began with a proof-of-principle demonstration which was the first to realize the promise of a new branch of SRF science. This achievement – the world's first successful demonstration of an SRF cavity operating at 10 MV/m while cooled solely by a commercial cryocooler – marked the cornerstone of this study. This accelerating gradient is in the relevant range for small-scale applications of interest, making this result a key step in developing compact SRF systems.

Another critical component of this study was the comparison of the effectiveness of different methods for controlling cryocooler-based assembly cooldowns and temperature cycles. This research explicitly showed that the use of independently controlled heaters can reduce thermal gradients across the cavity during cooldown to merely a few mK. In particular, this was the only method to reduce the thermal gradients to less than 200 mK/m, as is recommended to achieve optimal RF performance for a Nb_3Sn cavity [Hal17]. The trade-off is that this method is slightly more involved than a basic "cooler on, cooler off" technique for equilibrating assembly temperatures, which may not achieve as small of thermal gradients. Overall, this study paved the way for extending the conduction cooling concept to a full standalone SRF accelerating cryomodule.

The majority of the work discussed in this dissertation was committed to designing and commissioning such a cryomodule. Removing all liquid cryogenics and relying solely on conduction cooling methods proved quite challenging, particularly when designing the new SRF cavity and the high average power couplers. However,

a mix of ingenuity and creativity made accomplishing both of these tasks possible. The cavity, LCC1-1, was designed to handle high beam currents and deliver power to the beam efficiently. Thermal modeling of the final 4.2 K thermal link shows that it successfully keeps the cavity temperature near 4.2 K at the targeted operating gradient of 10 MV/m, confirming the effectiveness of its design.

Designing the new forward power coupler for the conduction cooled system was one of the most demanding parts of this project. Significantly reducing the 4.2 K heat load compared to the Cornell ERL injector couplers, which are themselves considered state-of-the-art, while increasing the forward power even further posed many difficulties. The addition of specialized components such as the RF shield and quarter-wave transformer made this lofty goal possible. Thermal modeling of the final design indeed showed a 4.2 K heat load of 1.1 W for 100 kW of forward power; this represents another major achievement of this dissertation work.

The final primary challenge of the conduction-cooled cryomodule design was ensuring that all other possible heat load sources in the system were minimized at 4.2 K. Between the cavity and couplers, most of the cooling capacity at 4.2 K was already accounted for, such that only ≈ 0.5 W remained for all other components combined. Yet with appropriate solutions, this final design goal was accomplished. A cooled thermal shield protects the cavity from room-temperature thermal radiation, while appropriately placed thin-walled structures and special materials such as G10 minimize conductive heat leak. All of these design choices and more resulted in the successful design of a high current, high power SRF cryomodule cooled entirely by just two cryocoolers.

The commissioning of the new SRF cavity, LCC1-1, was successfully completed over the course of about two years. Many challenges were faced along the way,

starting with the fabrication and welding of the unique design. During basic cavity treatments, visible surface defects near one of the irises first appeared after the bulk electropolish. The exact nature of these defects is still unclear, but it's possible that they contribute to the cavity's RF performance being worse than expected. Another possible cause is the Nb_3Sn coating; due to unfortunate circumstances, the cavity underwent a non-standard coating process. This may have resulted in a sub-optimal Nb_3Sn layer which could degrade RF performance. Even so, the cavity performance was sufficient for the next stages of the project, and the initial commissioning of LCC1-1 was considered successful.

7.1 What's Next?

Due to time constraints, full commissioning of the conduction-cooled cryomodule had not been completed at the time of writing, and was left in the hands of other capable graduate students. However, the pilot cleanroom assembly of the cavity vacuum components was successfully completed, which provided valuable information regarding several ways to improve the practicality and efficiency of the process. Several images taken during this process are shown in Figure 7.1.

The future outlook for this research is very promising. A proposed extension of this project was successfully funded, such that after commissioning and initial testing is completed, the cryomodule will be installed in a test beamline capable of delivering $\sim 600\,\mathrm{keV}$ electrons to a target. With a proposed beam current of $20\,\mathrm{mA}$, this system could provide the first demonstration of efficient, high current operation in a conduction-cooled SRF cavity. The promising future of this project, combined with those mentioned in Chapter 3, provides a strong case for the ability to bring SRF technology to widespread use in small operations in the near future.

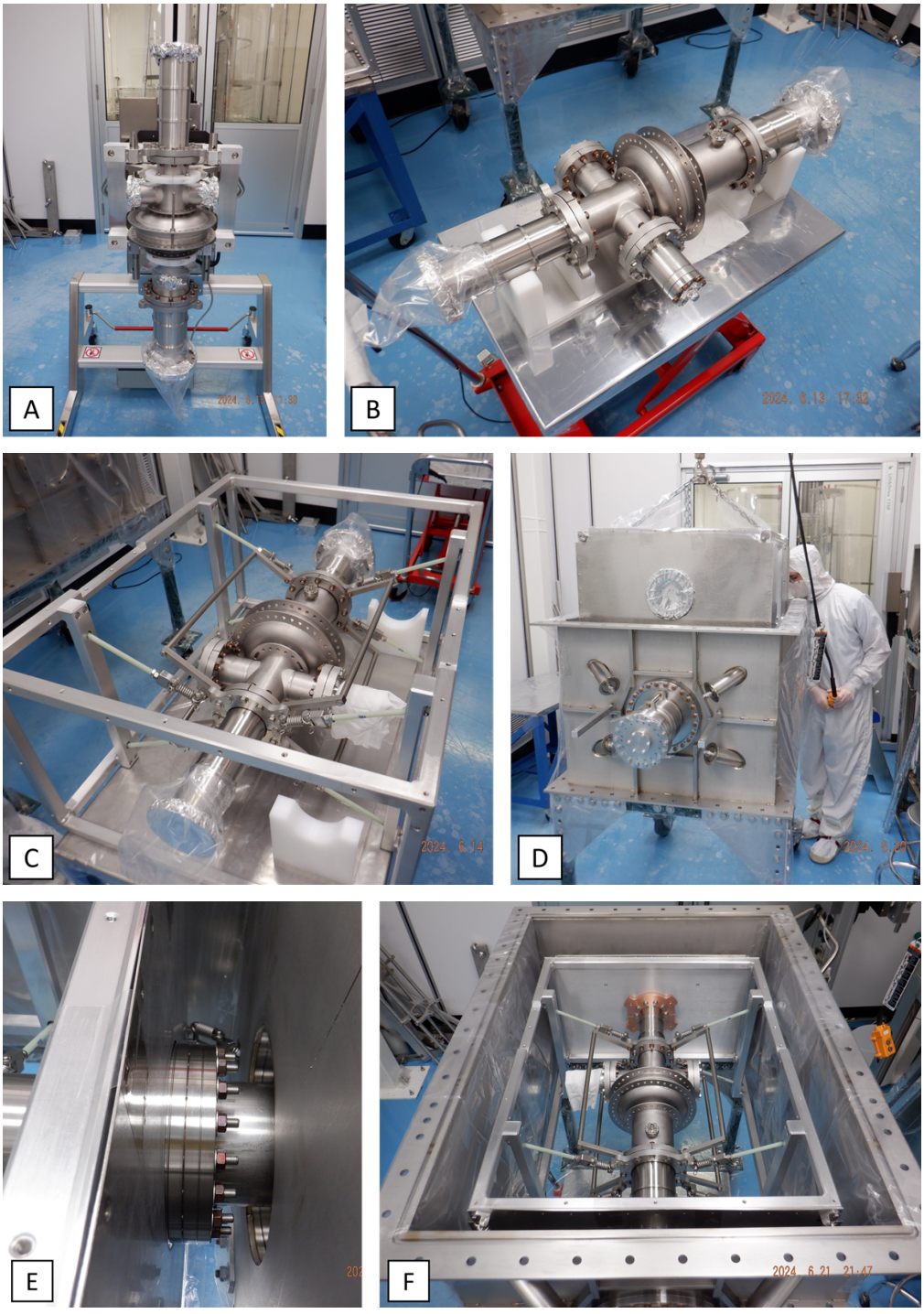

Figure 7.1: Various stages of the cleanroom portion of the new cryomodule assembly: (A) Beam tubes attached to LCC1-1, (B) All cavity indium seals completed, (C) LCC1-1 suspended from aluminum frame via G10 rods, (D) Assembly from (C) being lowered into outer vacuum vessel, (E) Final beam tube conflat seals completed, (F) Full cleanroom assembly completed.

APPENDIX A

DETAILED E-BEAM WELD SEQUENCE

This appendix contains more detailed images of each individual step in the e-beam welding process of LCC1-1, adapted from the technical drawings.

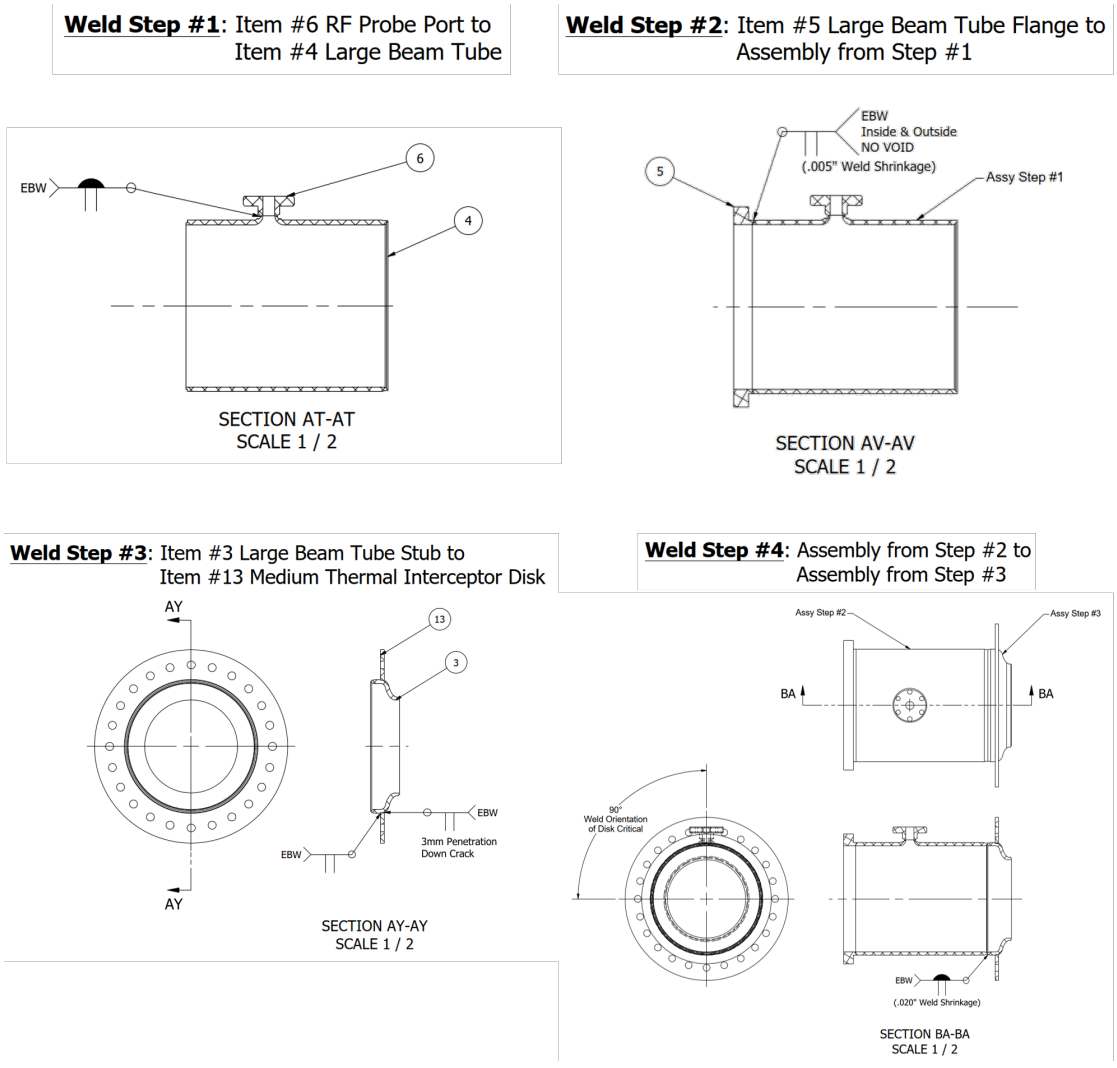

Figure A.1: E-beam welding steps 1 through 4.

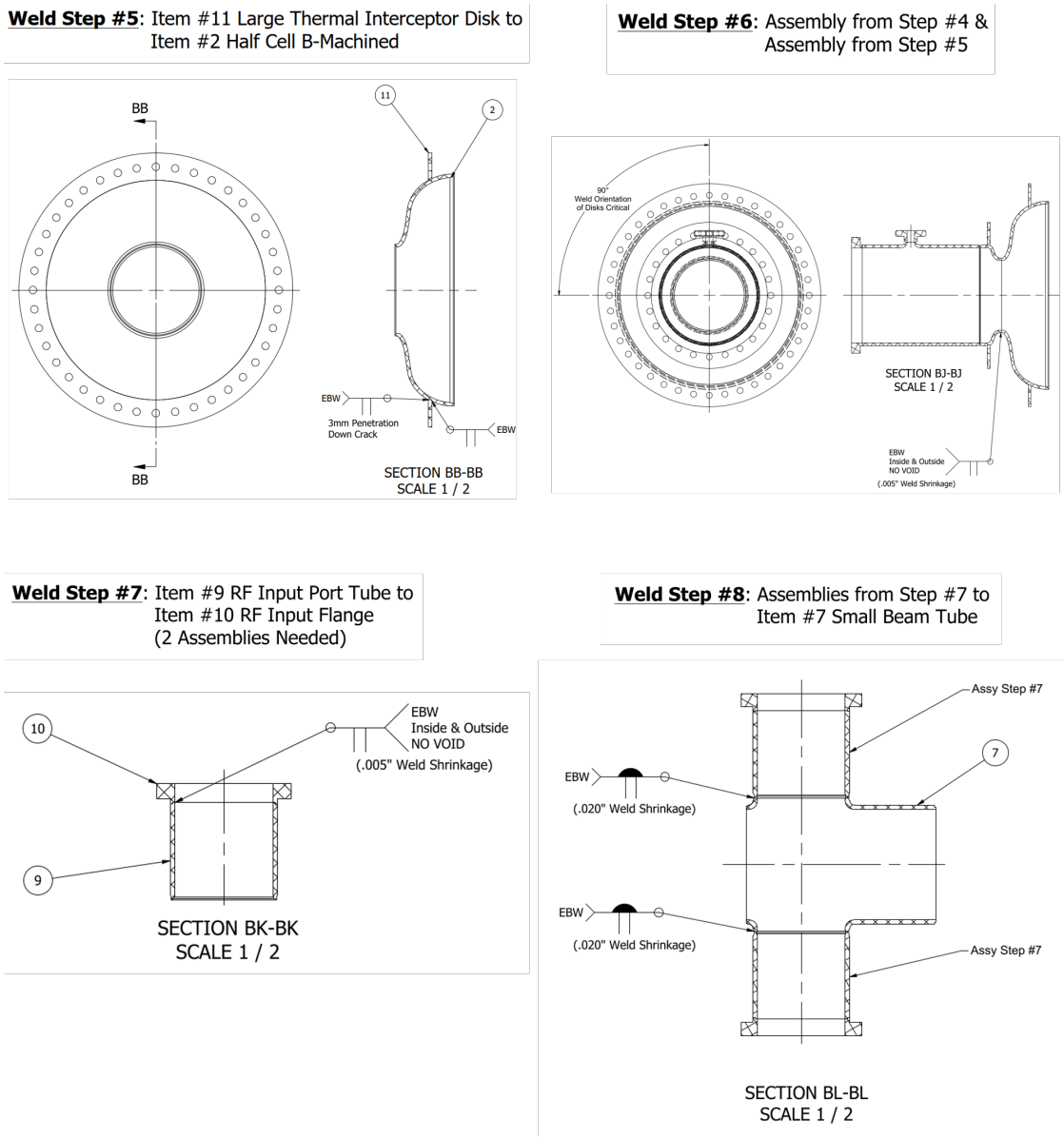

Figure A.2: E-beam welding steps 5 through 8.

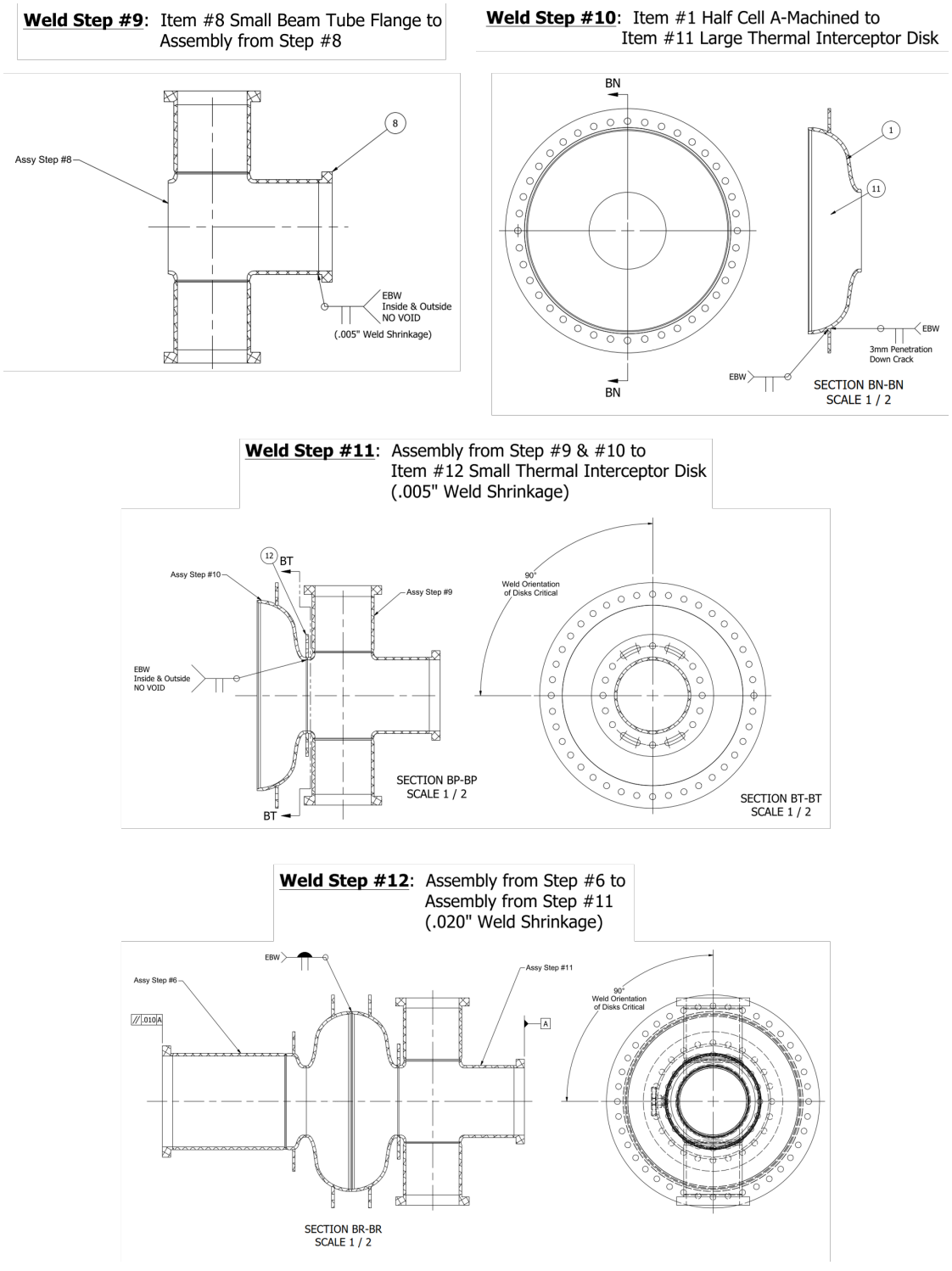

Figure A.3: E-beam welding steps 9 through 12.

BIBLIOGRAPHY

[A+00] B. Aune et al. Superconducting TESLA cavities. *Phys. Rev. ST Accel. Beams*, 3:092001, Sep. 2000.

[A+12] G. Aad et al. Observation of a new particle in the search for the Standard Model Higgs boson with the ATLAS detector at the LHC. *Physics Letters B*, 716(1):1–29, 2012.

[AJNK15] S. Aull, T. Junginger, H. Neupert, and J. Knobloch. Secondary Electron Yield of SRF Materials. In *Proc. 17th Int. Conf. on RF Superconductivity (SRF'15)*, pages 686–690, Geneva, Switzerland, Dec. 2015. JACoW, JACoW.

[Ans23] Ansys, Inc. Ansys Mechanical, Release 23.1, 2023.

[Api24] Apiezon. Apiezon N Grease, 2024.

[Ass98] National Electrical Manufacturers Association. NEMA Standards Publication No. LI 1-1998, 1998.

[Aut23] Autodesk, Inc. Autodesk Inventor, Version 23.2, 2023.

[B+02] I. Bazarov et al. Phase I Energy Recovery Linac at Cornell University. In *Proc. 8th European Particle Accelerator Conf. (EPAC'02)*. JACoW Publishing, Geneva, Switzerland, Aug. 2002.

[Baz21] N. Bazin. Basics for Cryomodule Design, Fabrication, and Assembly, June 2021. Part of the SRF'21 Tutorials Program.

[BCS57] J. Bardeen, L. N. Cooper, and J. R. Schrieffer. Theory of Superconductivity. *Phys. Rev.*, 108:1175–1204, Dec. 1957.

[BEW05] D. H. Bilderback, P. Elleaume, and E. Weckert. Review of third and next generation synchrotron light sources. *Journal of Physics B: Atomic, Molecular and Optical Physics*, 38(9):S773, Apr. 2005.

[Bli12] J. Bliss. U.S. Backs Off All-Cargo Scanning Goal with Inspections at 4%, Aug. 2012.

[Blu24] Bluefors. Pulse Tube Cryocoolers, 2024.

[BR13] P. Bradley and R. Radebaugh. *Properties of Selected Materials at Cryogenic Temperatures*. CRC Press, Boca Raton, FL, 2013.

[BS08] S. Belomestnykh and V. Shemelin. Multipacting-free transitions between cavities and beam-pipes. *Nuclear Instruments and Methods in Physics Research Section A: Accelerators, Spectrometers, Detectors and Associated Equipment*, 595(2):293–298, 2008.

[C+23] G. Ciovati et al. Development of a Prototype Superconducting Radio-Frequency Cavity for Conduction-Cooled Accelerators. Presented at SRF'23 in Grand Rapids, MI, USA, unpublished, Sep. 2023.

[CC64] G. D. Cody and R. W. Cohen. Thermal Conductivity of Nb3Sn. *Rev. Mod. Phys.*, 36:121–123, Jan. 1964.

[CCPR20] G. Ciovati, G. Cheng, U. Pudasaini, and R. A. Rimmer. Multi-metallic conduction cooled superconducting radio-frequency cavity with high thermal stability. *Superconductor Science and Technology*, 33(7):07LT01, May 2020.

[Cry23] Lakeshore Cryogenics. Cernox Sensor Packages and Mounting Adapters, 2023.

[CS08] G. Catelani and J. P. Sethna. Temperature dependence of the superheating field for superconductors in the high-κ London limit. *Phys. Rev. B*, 78:224509, Dec. 2008.

[D+22] R. C. Dhuley et al. Design of a 10 MeV, 1000 kW average power electron-beam accelerator for wastewater treatment applications. *Physical Review Accelerators and Beams*, 25(4), Apr. 2022.

[Das22] Dassault Systèmes SE. CST Studio Suite 2022, 2022.

[DPG+20] R. C. Dhuley, S. Posen, M. I. Geelhoed, O. Prokofiev, and J. C. T. Thangaraj. First Demonstration of a Cryocooler Conduction Cooled Superconducting Radiofrequency Cavity Operating at Practical CW Accelerating Gradients. *Superconductor Science and Technology*, 33(6):06LT01, Apr. 2020.

[DPGT22] R. C. Dhuley, S. Posen, M. I. Geelhoed, and J. C. T. Thangaraj. Development of a cryocooler conduction-cooled 650 MHz SRF cavity oper-

ating at ∼10 MV/m cw accelerating gradient. *IOP Conference Series: Materials Science and Engineering*, 1240(1):012147, May 2022.

[EKR+15] G. V. Eremeev, M. J. Kelley, C. E. Reece, U. Pudasaini, and J. Tuggle. Progress with Multi-Cell Nb3Sn Cavity Development Linked with S.ple Materials Charaterization. In *Proc. 17th Int. Conf. on RF Superconductivity (SRF'15)*, Whistler, Sep. 2015.

[G+07] R. L. Geng et al. Manufacture and Performance of Superconducting RF Cavities for Cornell ERL Injector. In *Proc. 22nd Particle Accelerator Conf. (PAC'07)*. JACoW Publishing, Geneva, Switzerland, Aug. 2007.

[G+17] A. Grassellino et al. Unprecedented quality factors at accelerating gradients up to 45 MV/m in niobium superconducting resonators via low temperature nitrogen infusion. *Superconductor Science and Technology*, 30(9):094004, Aug. 2017.

[GL50] V. L. Ginzburg and L. D. Landau. On the Theory of superconductivity. *Zh. Eksp. Teor. Fiz.*, 20:1064–1082, 1950.

[GL64] W. E. Gifford and R. C. Longsworth. Pulse-Tube Refrigeration. *Journal of Engineering for Industry*, 86(3):264–268, Aug. 1964.

[God06] A. Godeke. A review of the properties of Nb3Sn and their variation with A15 composition, morphology and strain state. *Superconductor Science and Technology*, 19(8):R68, June 2006.

[Gur14] A. Gurevich. Reduction of Dissipative Nonlinear Conductivity of Superconductors by Static and Microwave Magnetic Fields. *Phys. Rev. Lett.*, 113:087001, Aug. 2014.

[Hal17] D. Hall. *New Insights into the Limitations on the Efficiency and Achievable Gradients in Nb3Sn SRF Cavities*. PhD thesis, Cornell University, 2017.

[HGM+84] H. Heinrichs, T. Grundey, N. Minatti, G. Muller, M. Peiniger, H. Piel, G. Unterborsch, and H. P. Vogel. Activities on RF-Superconductivity at Wuppertal. In *Proc. 2nd Int. Workshop on RF Superconductivity (SRF'84)*, Geneva, July 1984.

[HMP+75] B. Hillenbrand, H. Martens, H. Pfister, K. Schnitzke, and G. Ziegler.

Superconducting Nb3Sn Cavities. *IEEE Transactions on Magnetics*, 11(2):420–422, Mar. 1975.

[HS09] W. Henning and C. Shank. Accelerators for America's Future, 2009.

[HW54] A. J. Hatch and H. B. Williams. The Secondary Electron Resonance Mechanism of Low-Pressure High-Frequency Gas Breakdown. *Journal of Applied Physics*, 25(4):417–423, Apr. 1954.

[HW15] S. Henderson and T. Waite. Workshop on Energy and Environmental Applications of Accelerators, June 2015.

[K+24] R. Kostin et al. First conduction cooled photoinjector status. In *Proc. 15th Int. Particle Accelerator Conf.*, pages 2747–2750. JACoW Publishing, Geneva, Switzerland, May 2024.

[KAM+23] S. V. Kutsaev, R. B. Agustsson, A. C. Araujo Martinez, R. D. Berry, P. R. Carriere, P. Frigola, and A. Y. Murokh. Industrial SRF Activities at RadiaBeam Technologies. Presented at SRF'23 in Grand Rapids, MI, USA, unpublished, Sep. 2023.

[KB96] F. Koechlin and B. Bonin. Parametrization of the niobium thermal conductivity in the superconducting state. *Superconductor Science and Technology*, 9(6):453, June 1996.

[Man20] J. Maniscalco. *Studies of the Field-Dependent Surface Resistance of Nitrogen-Doped Niobium for Superconducting Accelerators*. PhD thesis, Cornell University, 2020.

[Mat24] MatWeb, LLC. MatWeb Material Property Data, 2024.

[MD19] A. Miyazaki and W. V. Delsolaro. Two different origins of the Q-slope problem in superconducting niobium film cavities for a heavy ion accelerator at CERN. *Phys. Rev. Accel. Beams*, 22:073101, July 2019.

[PCE+19] U. Pudasaini, G. Ciovati, G. V. Eremeev, M. J. Kelley, I. P. Parajuli, C. E. Reece, and Md. N. Sayeed. Recent Results From Nb3Sn Single Cell Cavities Coated at Jefferson Lab. In *Proc. 19th Int. Conf. on RF Superconductivity (SRF'19)*, pages 65–70. JACoW Publishing, Geneva, Switzerland, Aug. 2019.

[PF79] R. L. Powell and F. R. Fickett. Cryogenic Properties of Copper, Dec. 1979.

[PH17] S. Posen and D. L. Hall. Nb3Sn superconducting radiofrequency cavities: fabrication, results, properties, and prospects. *Superconductor Science and Technology*, 30(3):033004, Jan. 2017.

[PKH08] H. Padamsee, J. Knobloch, and T. Hays. *RF Superconductivity for Accelerators*. Wiley-VCH, 2 edition, 2008.

[PL11] S. Posen and M. Liepe. Stoichiometric Nb3Sn in First Samples coated at Cornell. In *Proc. 15th Int. Conf. on RF Superconductivity (SRF'11)*, Chicago, Illinois, July 2011.

[PL14] S. Posen and M. Liepe. Advances in development of Nb3Sn superconducting radio-frequency cavities. *Phys. Rev. ST Accel. Beams*, 17:112001, Nov. 2014.

[PLM19] R. D. Porter, M. Liepe, and J.T. Maniscalco. High Frequency Nb3Sn Cavities. In *Proc. 19th Int. Conf. on RF Superconductivity (SRF'19)*, pages 44–47. JACoW Publishing, Geneva, Switzerland, Aug. 2019.

[PLS+21] S. Posen, J. Lee, D. N. Seidman, A. Romanenko, B. Tennis, O. S. Melnychuk, and D. A. Sergatskov. Advances in Nb3Sn superconducting radiofrequency cavities towards first practical accelerator applications. *Superconductor Science and Technology*, 34(2):025007, Jan. 2021.

[PLX11] S. Posen, M. Liepe, and Y. Xie. Cornell SRF New Materials Program. In *Proc. 2nd Int. Particle Accelerator Conf. (IPAC'11)*, San Sebastian, Sep. 2011.

[PMRT15] S. Posen, M. Merio, A. Romanenko, and Y. Trenikhina. Fermilab Nb3Sn R&D Program. In *Proc. 17th Int. Conf. on RF Superconductivity (SRF'15)*, Whistler, Dec. 2015.

[Por21] R. D. Porter. *Advancing the maximum accelerating gradient of Niobium-3 Tin superconducting radiofrequency accelerator cavities: RF measurements, dynamic temperature mapping, and material growth.* PhD thesis, Cornell University, 2021.

[Pos14] S. Posen. *Understanding and Overcoming Limitation Mechanisms in*

Nb3Sn Superconducting RF Cavities. PhD thesis, Cornell University, 2014.

[Pud24] U. Pudasaini. Nb3Sn SRF cavities: from R&D to real accelerator – overview of recent developments. Presented at IPAC'24, Nashville, TN, 2024, paper FRXD1, unpublished, May 2024.

[S+24] H. Sakai et al. Conceptual design of the high-power electron beam irradiator using niobium-tin superconducting cavity. *Journal of Physics: Conference Series*, 2687(9):092013, Jan. 2024.

[SB20] V. Shemelin and S. Belomestnykh. *Existence Zones for Multipactor Discharge*, pages 13–24. Springer International Publishing, Cham, 2020.

[SBG+03] V. Shemelin, S. Belomestnykh, R. L. Geng, M. Liepe, and H. Padamsee. Dipole-Mode-Free and Kick-Free 2-Cell Cavity for the SC ERL Injector. In *Proc. 20th Particle Accelerator Conf. (PAC'03)*. JACoW Publishing, Geneva, Switzerland, May 2003.

[She22] V. Shemelin. RF Coupler for 1300 MHz, 50 kW CW. Internal report, 2022.

[SHL+23a] N. A. Stilin, A. T. Holic, M. Liepe, T. I. O'Connell, P. Quigley, J. Sears, V. D. Shemelin, and J. Turco. Design of a 1.3 GHz High-Power RF Coupler for Conduction-Cooled Systems. In *Proc. 21st Int. Conf. on RF Superconductivity (SRF'23)*, pages 342–346. JACoW Publishing, Geneva, Switzerland, Sep. 2023.

[SHL+23b] N. A. Stilin, A.T. Holic, M. Liepe, R. D. Porter, J. Sears, and Z. Sun. RF and thermal studies on conduction cooled Nb3Sn SRF cavity. *Engineering Research Express*, 5(2):025078, June 2023.

[T+23] J.C.T. Thangaraj et al. Compact, High-Power Superconducting Electron Linear Accelerators for Environmental and Industrial Applications: Projects and Status. Presented at SRF'23 in Grand Rapids, MI, USA, unpublished, June 2023.

[TAI23] TAI. Thermal Straps, 2023.

[Tin96] M. Tinkham. *Introduction to Superconductivity*. McGraw-Hill, 2 edition, 1996.

[V+23] J. Vennekate et al. On the Way to a 10 MeV, Conduction-Cooled, Compact SRF Accelerator. In *Proc. 21st Int. Conf. on RF Superconductivity (SRF'23)*, pages 471–476. JACoW Publishing, Geneva, Switzerland, Sep. 2023.

[VBL+05] V. Veshcherevich, S. Belomestnykh, M. Liepe, V. Medjidzade, H. Padamsee, V. Shemelin, N. Sobenin, and A. Zavadtsev. Design of High Power Input Coupler for Cornell ERL Injector Cavities. In *Proc. 12th Int. Workshop on RF Superconductivity (SRF'05)*. JACoW Publishing, Geneva, Switzerland, July 2005.

[vDK10] D. van Delft and P. Kes. The discovery of superconductivity. *Physics Today*, 63(9):38–43, Sep. 2010.

[VL11] N. Valles and M. Liepe. The Superheating Field of Niobium: Theory and Experiment. In *Proc. 15th Int. Conf. on RF Superconducivity (SRF'11)*, pages 293 – 301, Chicago, Illinois, July 2011.

[VR08] G. Ventura and L. Risegari. *The Art of Cryogenics*. Elsevier, 2008.

[Wal83a] G. Walker. *Gifford-McMahon, Solvay, and Postle Cryocoolers*, pages 237–263. Springer US, Boston, MA, 1983.

[Wal83b] G. Walker. *Joule-Thomson Cooling Systems*, pages 265–295. Springer US, Boston, MA, 1983.

[XRK13] B. P. Xiao, C. E. Reece, and M. J. Kelley. Superconducting surface impedance under radiofrequency field. *Physica C: Superconductivity*, 490:26–31, 2013.

[Y+24] Z. Yang et al. Stable Acceleration of a LHe-Free Nb3Sn demo SRF e-linac Based on Conduction Cooling. 2024.

[YOP01] P. Ylä-Oijala and D. Proch. MultiPac - Maltipacting Simulation Package with 2D FEM Field Solver. In *Proc. 10th Int. Workshop on RF Superconductivity (SRF'01)*. JACoW Publishing, Geneva, Switzerland, Sep. 2001.